UNIVERSITA' DEGLI STUDI
DI MODENA E REGGIO EMILIA

Dottorato di ricerca in "Physics and Nanosciences"

Ciclo XXXVIII

Electron beam induced plasma effects on functional materials

Candidata: Caterina Chiari

Relatore (Tutor): Prof. Marco Beleggia

Coordinatore del Corso di Dottorato: Prof. Marco Affronte

Abstract

The interaction between high-energy electron beams and matter lies at the core of Transmission and Scanning Transmission Electron Microscopy (TEM/STEM), where the incident probe not only images materials with atomic resolution but can also actively modify their electronic and structural properties. Despite extensive experimental and theoretical efforts, a unified description that connects microscopic electron–atom scattering events to the macroscopic evolution of charge, electrostatic potential, and electrical conductivity in irradiated materials is still lacking.

In this thesis, a multiscale theoretical framework is developed to bridge quantum scattering theory with continuum transport and electrostatics under electron-beam irradiation. Starting from first principles, elastic and inelastic electron–atom scattering processes are described using a relativistically corrected Schrödinger formalism, which retains analytical tractability while incorporating the essential kinematic effects relevant to typical TEM/STEM energies (100–300 keV). Scattering amplitudes and cross sections are derived within the first Born approximation for hydrogenic systems and extended to multi-electron targets, with particular emphasis on excitation processes and on ionization, the latter being responsible for the generation of free charge carriers.

Beyond the single-collision picture, the microscopic cross sections are employed to construct kinetic models describing the temporal evolution of carrier densities under continuous irradiation and after beam switch-off. Analytical solutions are obtained for both the build-up and relaxation phases, allowing the identification of characteristic time scales and their dependence on material parameters. The framework is subsequently extended to real materials, including insulators, semiconductors, and metals, highlighting the distinct roles of recombination mechanisms and excess carrier generation.

Finally, charge transport and electrostatic feedback are investigated through drift–diffusion equations self-consistently coupled to Poisson's equation. The resulting

steady-state solutions elucidate how local ionization, carrier migration, and electrostatic potential build-up shape non-uniform charge distributions in irradiated samples, and clarify the limits of commonly adopted approximations such as quasi-neutrality.

Overall, this work demonstrates that stationary quantum scattering theory can be consistently connected to macroscopic transport and electrical response, providing a unified and physically transparent description of beam–matter interaction across multiple length and time scales. The proposed approach offers a general strategy for linking microscopic collision physics to emergent collective behavior in irradiated materials, with implications not only for quantitative electron microscopy, but also for radiation physics, semiconductor science, and plasma–material interaction.

Contents

Introduction

The Transmission Electron Microscope (TEM) exploits the various signals generated during the interaction of high-energy electrons with matter to produce images of unprecedented spatial resolution, far beyond the diffraction limit of optical microscopy.

Since its invention in the early twentieth century by Ernst Ruska and Max Knoll [1], who first demonstrated the principle of electron imaging in 1931, TEM technology has undergone continuous and extraordinary evolution. Initially limited by lens aberrations and detector sensitivity, the instrument has progressively benefited from innovations in electron optics, cryogenic stabilization, and digital signal processing.

Over the decades, the combination of aberration correction, coherent electron sources, and advanced detection schemes has transformed the microscope from a purely imaging instrument into a quantitative analytical probe, capable of retrieving both amplitude and phase information from the transmitted electron wave [2, 3, 4].

As a result, electron microscopy has become a cornerstone of modern experimental science, with applications that extend well beyond materials physics to include chemistry, nanotechnology, and structural biology [5, 6, 7, 8]. The capability to visualize atomic-scale structures has also opened new frontiers for the direct observation of dynamic phenomena, such as charge transfer, diffusion, and structural phase transitions, thus linking microscopy to fundamental processes in condensed-matter and plasma physics. In this sense, TEM has evolved from a passive imaging device into a powerful active probe, where the beam itself becomes an agent capable of inducing, controlling, and recording transformations at the atomic level [9, 10].

Understanding how energetic electrons interact with solids is therefore essential for the correct interpretation of Transmission and Scanning Transmission Electron Microscopy (TEM/STEM) experiments. In these instruments, the incident beam not only probes the structure of materials but can also actively modify them, initiating a complex interplay between elastic and inelastic scattering, ionization, charge migration, and local potential build-up [11, 12].

Despite decades of experimental and theoretical work, the physical connection between single-electron scattering events and the collective evolution of charge, potential and conductivity in irradiated specimens, remains only partially understood. Bridging this gap requires a framework that can coherently connect quantum-level interactions to continuum-scale observables. This is a goal that remains one of the most ambitious challenges in electron microscopy theory.

The present work aims to address this issue by developing a multiscale theoretical framework that bridges the quantum-mechanical description of scattering with the macroscopic transport and charging dynamics induced by electron-beam irradiation.

Starting from first principles, the analysis seeks to connect individual collision amplitudes with measurable quantities such as local potential, charge density, and conductivity, thus establishing a unified description of beam–sample interaction from the atomic to the macroscopic scale. Such a unified treatment is particularly relevant in the modern context of *in-situ* and time-resolved microscopy, where the distinction between "observation" and "perturbation" becomes increasingly blurred, and quantitative modeling is essential to disentangle intrinsic material properties from beam-induced effects.

The study begins with a rigorous treatment of electron–atom scattering for an idealized hydrogenic system at incident energies between 100 and 300 keV, representative of typical TEM/STEM operating conditions. Although scattering is intrinsically a time-dependent phenomenon, it can be consistently formulated using the stationary form of the Schrödinger equation, which describes the asymptotic behavior of incoming and outgoing wavefunctions [13, 14, 15, 16]. In this regime, the analysis employs a relativistically corrected Schrödinger equation and neglects spin effects. The electron beam is unpolarized, and no spin-dependent observables are considered; therefore, the full Dirac formalism is unnecessary. This approach retains the essential physics of high-energy scattering while keeping the formalism analytically tractable.

The first Born approximation provides the scattering amplitudes and the corresponding differential and total cross sections for elastic and inelastic processes, including excitation and ionization [17, 18, 19].

The calculated cross sections indicate that elastic scattering plays a primary role in governing the angular redistribution of the incident probe and its coherent interaction with the specimen lattice, particularly at high beam energies. However, experimental evidence shows that the relative importance of elastic and inelastic scattering strongly depends on the atomic number, with the total inelastic cross section exceeding the elastic one for low-Z systems [20]. In such cases, inelastic channels contribute significantly over a broad range of energy transfers and momentum exchanges, rather than being restricted to highly specific conditions.

This analysis also clarifies how the transition from discrete bound states to continuum states leads to the onset of ionization, thereby linking the microscopic scattering formalism to the macroscopic generation of free carriers and to the onset of measurable current within the illuminated volume.

Chapter 1 establishes the theoretical foundations of quantum scattering relevant to electron microscopy. After introducing a relativistically corrected Schrödinger equation appropriate for TEM/STEM energies, the chapter systematically develops the formalism of elastic and inelastic scattering, emphasizing the equivalence between time-dependent and stationary approaches through the Lippmann–Schwinger equation. The role of the $\mathcal{T}$ and $\mathcal{S}$ operators is discussed in detail, with particular attention to unitarity, multichannel scattering, and probability conservation. Scattering amplitudes and differential cross sections are derived within the first Born approximation, and the formalism is extended from single-electron targets to multi-electron atoms, with explicit applications to elastic scattering, excitation, and ionization of carbon. This chapter provides the microscopic quantum-mechanical basis upon which the subsequent multiscale analysis is built.

Chapter 2 focuses on elastic scattering in the presence of a convergent electron probe, representative of modern STEM conditions. Moving beyond the plane-wave approximation, the incident electron is described as a spherical wave emitted from a localized source. Both on-axis and off-axis source configurations are analyzed, revealing how beam convergence and source displacement break translational symmetry and introduce additional angular structure in the scattering amplitude. Numerical evaluations are presented to compare spherical-wave and plane-wave scattering, highlighting the implications for TEM and STEM imaging, including expected effects on HAADF-STEM intensity and contrast formation. This chapter clarifies the physical consequences of probe geometry on elastic scattering processes in focused-beam microscopy.

Chapter 3 addresses inelastic scattering and the generation of free charge carriers under electron-beam irradiation. Starting from ionization and recombination rates derived from microscopic cross sections, the temporal evolution of carrier densities is analyzed using kinetic equations. Both the irradiation phase and the beam switch-off regime are treated analytically, allowing the identification of characteristic and relaxation times under TEM conditions. The framework is then extended to realistic materials, including insulators, semiconductors, and metals, highlighting the distinct roles of recombination mechanisms and material parameters. The chapter culminates in a macroscopic description of beam-induced electrical conductivity, distinguishing between intrinsic and excess contributions and discussing their build-up and relaxation. These results establish a direct link between inelastic scattering events and the emergence of measurable electrical response in irradiated specimens.

Chapter 4 investigates charge transport and electrostatic coupling within the irradiated sample. The spatial redistribution of electrons between illuminated and non-illuminated regions is described using drift–diffusion equations self-consistently coupled to Poisson's equation. Steady-state solutions are analyzed, together with their boundary and matching conditions, and the limits of commonly used approximations such as quasi-neutrality are discussed. This approach provides a physically transparent picture of how local ionization, transport, and electrostatic feedback cooperate to shape non-uniform potential landscapes, which in turn influence both carrier dynamics and beam–sample interaction.

The Conclusions summarize the main results and outline the broader implications of the present framework. A central outcome of this work is the demonstration that stationary quantum scattering theory can be consistently connected to continuum transport and electrostatics, enabling a unified description of beam–matter interaction across vastly different length and time scales. The proposed approach offers a general multiscale strategy for linking microscopic collision physics to emergent macroscopic behavior in irradiated matter, with relevance not only for electron microscopy, but also for radiation physics, semiconductor science, and plasma–material interaction.

Beyond its immediate application to electron microscopy, the theoretical framework developed in this work offers a general multiscale strategy for connecting microscopic collision physics to emergent macroscopic behavior in systems driven far from equilibrium by charged-particle irradiation.

By explicitly linking quantum-mechanical scattering amplitudes to continuum transport and electrostatic equations, the present approach provides a predictive and physically transparent description of beam–sample interaction. This framework is naturally suited for future extensions involving complex materials, multi-element targets, and secondary-electron cascades, paving the way toward a fully quantitative theory of irradiation-induced phenomena in modern high-resolution electron microscopy. More broadly, the methodology outlined here contributes to the ongoing effort to bridge quantum kinetics and continuum electrodynamics, offering new insights into how microscopic processes give rise to collective behavior in irradiated matter, an issue of central relevance not only to microscopy, but also to radiation physics, semiconductor science, and plasma–material interaction.

Chapter 1

Quantum Scattering Formalism

1.1 Relativistically Corrected Schrödinger Equation in TEM/STEM

In Transmission and Scanning Transmission Electron Microscopy (TEM/STEM), the incident electrons are accelerated by an electrostatic potential difference typically ranging from 100 kV to 300 kV. At these energies[1] , the electron velocity reaches a significant fraction of the speed of light ($v \simeq 0.55\,c$ at 100 keV and $v \simeq 0.78\,c$ at 300 keV), so that relativistic effects in the electron kinematics cannot be neglected. In particular, relativistic corrections are essential for an accurate description of the electron wavelength, momentum, phase accumulation, and probability current, all of which directly affect diffraction patterns and image contrast [6, 7, 8].

Despite the relativistic nature of the electron beam, a fully covariant Dirac treatment is generally unnecessary for TEM and STEM applications. Spin-dependent effects such as fine-structure splitting, spin–orbit coupling, and the Darwin term [14, 15] have a negligible impact on elastic scattering and phase contrast for unpolarized, high-energy electron beams. As a consequence, the standard theoretical description adopted in electron microscopy consists of a *scalar*, Schrödinger-like wave equation, in which relativistic effects are incorporated exclusively through the kinematics of the electron, while the interaction with the specimen is described by a classical electrostatic potential. This hybrid approach represents a controlled approximation to

---

[1] An electron accelerated through a potential difference V gains a kinetic energy $E = eV$, where e is the elementary charge. Therefore, an acceleration voltage of 1 kV corresponds to an electron energy of 1 keV. At typical TEM/STEM voltages (100–300 kV), the electron kinetic energy (100–300 keV) becomes a significant fraction of the electron rest energy ($m_e c^2 = 511\,\text{keV}$), and relativistic corrections must be taken into account.

the Dirac equation and forms the basis of essentially all analytical and numerical treatments in TEM and STEM.

Throughout this work, the electron mass m denotes the invariant (rest) mass. Relativistic effects enter through the Lorentz factor

$$\gamma = \frac{1}{\sqrt{1-(v/c)^2}}, \tag{1.1}$$

which characterizes the relation between energy, momentum, and velocity for the incident electron.

To clarify the origin of the scalar relativistic description, it is useful to briefly recall its connection to the Dirac equation. In the presence of an external electrostatic potential $V(\mathbf{r})$, the stationary Dirac equation reads

$$\left[c\,\boldsymbol{\alpha}\cdot\mathbf{p} + \beta mc^2 - eV(\mathbf{r})\right]\Psi(\mathbf{r}) = E\,\Psi(\mathbf{r}), \tag{1.2}$$

where $\mathbf{p} = -\mathrm{i}\hbar\nabla$ and the electron charge is $-e$, so that $-eV(\mathbf{r})$ represents the interaction energy. Here $\boldsymbol{\alpha}$ and β denote the standard Dirac matrices.

The Dirac spinor $\Psi = (\varphi, \chi)^T$ naturally separates into a *large* component φ and a *small* component χ. The large component represents the dominant, Schrödinger-like part of the wavefunction and survives in the non-relativistic limit, whereas the small component encodes relativistic corrections associated with the coupling between positive and negative energy states, including spin-dependent effects such as spin–orbit coupling and the Darwin term. Formally, the small component scales as $|\mathbf{p}|/(mc)$ relative to the large one.

For high-energy electrons in TEM and STEM, the quantity $|\mathbf{p}|/(mc)$ is not asymptotically small (it typically lies in the range 0.5–0.8 for accelerating voltages between 100 and 300 keV). However, the scalar approximation remains justified because the spin-dependent terms encoded in χ give rise to corrections that are small compared to the dominant electrostatic interaction with the specimen potential. In particular, spin polarization and spin–orbit effects are usually negligible in standard electron microscopy experiments, which motivates the elimination of the small component and the adoption of a scalar wave description.

Eliminating χ yields a second-order equation for the large component,

$$\left[(E+eV)^2 - m^2c^4\right]\varphi = c^2\mathbf{p}^2\,\varphi, \tag{1.3}$$

where spin–orbit coupling, the Darwin term, and other spin-dependent contributions have been neglected. Within the scalar approximation adopted in this work, the electron wavefunction used in the following is identified with the large component,

$$\psi(\mathbf{r}) \equiv \varphi(\mathbf{r}), \tag{1.4}$$

thereby providing a direct and physically transparent link between the Dirac formalism and the relativistically corrected Schrödinger-like description.

The relativistic kinetic energy of the electron is defined as

$$T = E - mc^2 = (\gamma - 1)mc^2. \tag{1.5}$$

For an electron accelerated through an electrostatic potential difference U, energy conservation yields

$$T = eU, \tag{1.6}$$

so that the total energy becomes

$$E = mc^2 + eU = \gamma mc^2, \qquad \gamma = 1 + \frac{eU}{mc^2}. \tag{1.7}$$

The relativistic energy–momentum relation,

$$E^2 = (pc)^2 + (mc^2)^2, \tag{1.8}$$

then gives the electron momentum

$$p = \sqrt{2meU\left(1 + \frac{eU}{2mc^2}\right)}. \tag{1.9}$$

In electron optics, it is convenient to introduce the *relativistically corrected accelerating voltage*

$$U^* \equiv U\left(1 + \frac{eU}{2mc^2}\right) = \frac{1+\gamma}{2}U. \tag{1.10}$$

The relativistic momentum is then

$$p^2 = 2meU^*, \tag{1.11}$$

which greatly simplifies the mathematical structure of the wave equation while retaining the correct relativistic kinematics.

Equation (1.3) has a Klein–Gordon-like structure. For high-energy electrons in TEM/STEM and for interaction energies satisfying $|eV| \ll E$, one may expand the left-hand side of Eq. (1.3) to first order in the electrostatic potential. This procedure yields a Helmholtz-type equation for the scalar wavefunction,

$$\left(\nabla^2 + k^2\right) \psi(\mathbf{r}) = -\frac{2me\gamma}{\hbar^2} V(\mathbf{r})\, \psi(\mathbf{r}), \qquad k = \frac{p}{\hbar}. \tag{1.12}$$

This equation constitutes the starting point of the multislice and Bloch-wave formalisms widely used in TEM and STEM [6, 7, 8, 21, 22, 23].

Multiplying Eq. (1.12) by $-\hbar^2/(2m)$ and using $p^2 = 2meU^*$ finally leads to the relativistically corrected Schrödinger equation in the form commonly employed in electron optics,

$$\frac{1}{2m} \left(-\mathrm{i}\hbar\nabla\right)^2 \psi(\mathbf{r}) = e\left[U^* + \gamma V(\mathbf{r})\right] \psi(\mathbf{r}). \tag{1.13}$$

In this representation, relativistic effects enter exclusively through the parameters γ and U^*, while the differential operator retains the familiar non-relativistic Schrödinger form.

The electron wavelength is defined as

$$\lambda = \frac{h}{p}. \tag{1.14}$$

Using Eq. (1.9), one obtains

$$\lambda = \frac{h}{\sqrt{2meU}\sqrt{1 + \dfrac{eU}{2mc^2}}}. \tag{1.15}$$

Equivalently, since $p = \gamma m v$, the wavelength may also be written as

$$\lambda = \frac{h}{\gamma m v}. \tag{1.16}$$

In the scattering theory developed in the following sections, the standard non-relativistic formalism is retained for analytical clarity. Relativistic corrections are incorporated through the kinematics of the incident and scattered electrons and through explicit factors of the Lorentz parameter γ appearing in the normalization of probability currents and scattering cross sections. This approach preserves the formal structure of the Lippmann–Schwinger equation and the Born expansion, while ensuring the correct description of relativistic electron beams.

In summary, high-energy electron propagation in TEM and STEM is described by a scalar Schrödinger-like equation with relativistically corrected kinematics. Although the underlying dynamics is fundamentally relativistic, the dominance of electrostatic interactions and the negligible role of spin degrees of freedom in most imaging conditions justify the use of this controlled scalar approximation. This hybrid formulation provides an accurate and computationally efficient framework for electron scattering and imaging, and it constitutes the standard theoretical foundation of quantitative TEM and STEM simulations [6, 7, 8, 24].

Finally, it is important to emphasize that Eq. (1.13) provides the rigorous starting point for the paraxial description of high-energy electron propagation in TEM and STEM.

By factoring out the rapidly varying longitudinal phase,

$$\psi(\mathbf{r}) = \tilde{\psi}(x, y, z)\, e^{ikz}, \qquad k = \frac{p}{\hbar}, \tag{1.17}$$

and assuming that the envelope $\tilde{\psi}(x, y, z)$ varies slowly along the optical axis z (forward-scattering or paraxial approximation), one obtains the standard paraxial wave equation

$$i\hbar\, \frac{\partial \tilde{\psi}}{\partial z} = -\frac{\hbar^2}{2p}\, \nabla_\perp^2 \tilde{\psi} + \hbar\, C_E\, V(x, y, z)\, \tilde{\psi}, \tag{1.18}$$

where $\nabla_\perp^2$ denotes the transverse Laplacian and $p = \gamma m v$ is the relativistic electron momentum.

The coefficient C_E is the relativistically corrected electron–matter interaction constant. It quantifies the phase modulation induced by the electrostatic potential and therefore determines the strength of elastic scattering in the paraxial regime. It is given by

$$C_E = \frac{me}{\hbar^2 k} \left(1 + \frac{E}{2mc^2} \right), \qquad k = \frac{p}{\hbar}, \tag{1.19}$$

where E denotes the kinetic energy of the incident electron.

Equation (1.18) governs high-energy electron propagation in electron microscopy and constitutes the theoretical basis of the multislice formalism [21], the contrast transfer function (CTF) framework, and the description of focused STEM probes. The paraxial approximation thus emerges naturally as the high-energy, small-angle limit of the relativistically corrected Schrödinger equation, establishing a direct connection between the underlying Dirac formalism and practical imaging models in TEM and STEM.

1.2 Elastic and Inelastic Scattering Processes

In electron microscopy (EM), electron–matter interactions can be broadly classified as elastic or inelastic. Elastic scattering refers to processes in which the total kinetic energy of the combined system, consisting of the incident electron and the target, is conserved, although energy may be redistributed between the two. Elastic interactions are responsible for diffraction contrast, coherent imaging mechanisms, and the phase evolution of the transmitted electron wave, thereby determining the structural information encoded in the image. Experimental evidence shows, however, that particularly for low-Z materials, the total inelastic cross section can exceed the elastic one [20]. Therefore, although elastic scattering is fundamental for image formation, inelastic scattering represents an essential component of electron–matter interactions in many practical EM conditions. Inelastic processes generate a wide variety of secondary signals, including characteristic X-rays, Auger and secondary electrons, and visible photons through cathodoluminescence [5, 9, 10]. These signals provide complementary information on the chemical composition, electronic structure, and bonding configuration of the specimen, which cannot be accessed through elastic interactions alone.

Inelastic electron–matter interactions constitute the physical basis of analytical techniques such as Electron Energy–Loss Spectroscopy (EELS) and Energy–Filtered Transmission Electron Microscopy (EFTEM), which exploit the energy distribution of scattered electrons to probe the local chemical and electronic environment [7, 10, 20]. By analyzing the energy–loss spectrum, one can identify elemental composition, map spatial distributions, and infer bonding states with atomic-scale spatial resolution. Each inelastic scattering event corresponds to a transition of the target from its ground state to an excited or ionized state and therefore contributes to the progressive modification of the specimen under electron-beam irradiation. At sufficiently high beam currents or prolonged exposure times, the accumulation of ionization events may drive the system toward a quasi–plasma regime, as encountered for example in beam-induced charging of insulating materials under TEM conditions.

Radiation damage, manifested as the progressive alteration of the atomic or molecular structure of the specimen, arises predominantly from inelastic collisions [9, 12]. Processes such as bond breaking, radiolysis, electron–hole pair generation and recombination, and local heating are all consequences of inelastic energy transfer. Because the relevant cross sections and material properties evolve dynamically as the sample composition and charge state change, quantitative modeling must account for the coupled temporal and spatial evolution of molecular fragments, secondary electrons, and charge carriers generated by these processes. Recent developments in structured and vortex electron beams [25] have introduced an additional degree of control, enabling the selective modulation of scattering channels through the orbital angular momentum of the incident beam.

In the present work, we begin with an analytical treatment of electron–hydrogen scattering, decomposing the total wavefunction into elastic and inelastic contributions. This approach allows closed-form expressions for both interaction channels, enabling a direct visualization of elastic diffraction, excitation, ionization, and secondary electron formation. Despite its apparent simplicity, the hydrogenic model already exhibits rich and nontrivial behavior, illustrating how even the most elementary atomic system undergoes significant modifications under sustained electron-beam irradiation.

To theoretically describe scattering processes, it is convenient to employ the *integral form* of the Schrödinger equation [13, 15, 26], obtained from the Lippmann–Schwinger equation and typically formulated within a time-independent framework. Although the Hamiltonian may be time independent, the physical states relevant to scattering are generally non-stationary: the incident wave represents a particle propagating toward a localized scattering center, which upon interaction generates outgoing spherical waves. Scattering theory therefore intrinsically connects the time-dependent and stationary formulations of quantum mechanics.

While the time-dependent approach is conceptually fundamental, it is often analytically cumbersome. It can be shown rigorously that the stationary formulation leads to the same Lippmann–Schwinger equation as obtained from the full time-dependent analysis [13, 15, 19]. This equivalence allows one to compute experimentally observable quantities, such as scattering amplitudes and differential cross sections, using stationary wavefunctions, thereby simplifying the theoretical development without loss of physical content.

A comprehensive framework encompassing all scattering processes is provided by $\mathcal{S}$–matrix theory [18, 19], which relates asymptotic incoming and outgoing states through a unitary transformation. In many situations relevant to electron microscopy, such as collisions of fast electrons with atomic or light molecular targets, it is sufficient to truncate the perturbative expansion at first order, leading to the Born approximation.

The Born approximation is formally valid when the scattering potential induces only a small perturbation of the incident wave over the spatial extent of the interaction region. From scattering theory, a more precise high-energy criterion can be expressed in terms of the dimensionless parameter

$$ka \gg 1, \tag{1.20}$$

where k is the electron wave number and a is a characteristic range of the potential. In this regime, the Born approximation requires that the potential energy satisfies

$$|V| \ll \frac{\hbar^2 k}{ma}, \tag{1.21}$$

which ensures that the phase shift accumulated by the electron across the interaction region remains small.

For a localized atomic potential of spatial extent a, this condition is more restrictive than the simple energetic requirement $|V| \ll U$, where U denotes the kinetic energy of the incident electron. Indeed, Eq. (1.21) expresses the fact that the Born approximation is fundamentally a condition on the phase modulation induced by the potential, rather than on the absolute magnitude of the interaction energy.

In extended systems such as crystals, however, the notion of a single interaction range a becomes ambiguous. In this case, the relevant small parameter is provided by the weakness of the crystal potential relative to the kinetic energy of the fast electron, and the practical validity of the Born approximation is often assessed through the condition

$$|eV(\mathbf{r})| \ll U, \tag{1.22}$$

which ensures that multiple scattering and strong channel coupling remain limited. For typical accelerating voltages in TEM and STEM, the electron kinetic energy is several orders of magnitude larger than the characteristic Fourier components of the crystal potential, so that the perturbative regime is generally well satisfied.

The Born approximation therefore provides the natural theoretical starting point for the analysis of electron–atom and electron–crystal scattering developed in the following sections. Although multiple scattering effects may become important in thick samples or for heavy elements, the Born framework captures the essential physics of high-energy electron interactions and remains the conceptual basis of most analytical and numerical scattering formalisms used in electron microscopy.

Many phenomena in atomic, molecular, and solid-state physics fall within or close to the regime defined by Eqs. (1.21) and (1.22), and the qualitative physical picture provided by the Born approximation often remains useful even in situations where higher-order corrections become non-negligible. In particular, perturbative scattering theory constitutes the standard theoretical framework for high-energy electron interactions and forms the basis of most analytical treatments of electron diffraction and spectroscopy [13, 17, 19, 20]. For this reason, despite its formal limitations, the Born formalism remains a central conceptual and computational tool in the theoretical description of electron scattering processes.

1.3 Time-Dependent and Time-Independent Approaches

The Schrödinger equation admits exact analytical solutions only for a limited class of simple potentials. For most physically relevant systems, one must therefore rely on approximate methods, among which perturbation theory occupies a central role [14, 15, 16, 26]. Within this framework, the Hamiltonian is written as

$$H = H_0 + \delta H_1, \tag{1.23}$$

where H_0 has known eigenvalues and eigenstates, H_1 represents a perturbing interaction, and δ is a dimensionless coupling constant interpolating between the unperturbed ($\delta = 0$) and full ($\delta = 1$) regimes. When H_1 is time independent, one speaks of *stationary perturbation theory*, whose purpose is to determine energy shifts and wavefunction corrections. If H_1 depends explicitly on time, one instead deals with *time-dependent perturbation theory*, which is used to compute transition probabilities between unperturbed states.

The distinction between these two approaches is more subtle than it may appear. Even for a time-independent Hamiltonian, the physical states of interest may be intrinsically non-stationary, as in scattering processes.[2] In scattering, the incident wave evolves dynamically as it interacts with a localized potential, producing an outgoing wave with modified amplitude and phase. Nevertheless, all experimentally measurable quantities, such as scattering amplitudes and differential cross sections, can be obtained within the stationary formalism. This equivalence between time-dependent and time-independent descriptions lies at the foundation of modern scattering theory [13, 18, 19].

1.3.1 Lippmann–Schwinger Equation and Stationary Scattering

Having established a scalar Schrödinger-like description with relativistically corrected kinematics, we now develop the scattering formalism within the standard stationary framework. Relativistic effects are consistently incorporated through the values of the incident momentum, wavelength, and probability current, while the formal structure of the Lippmann–Schwinger equation is retained.

Consider a collision process governed by the Hamiltonian

$$H = H_0 + V, \qquad H_0 = \frac{\mathbf{p}^2}{2m} = \frac{\hbar^2 \mathbf{k}^2}{2m}. \tag{1.24}$$

In the absence of an interaction potential ($V = 0$), the stationary eigenstates of H_0 are free-particle plane waves $|\mathbf{k}\rangle$. When $V \neq 0$, the eigenstates are modified according to

$$H_0 |\phi\rangle = E|\phi\rangle, \tag{1.25}$$

$$(H_0 + V)|\psi\rangle = E|\psi\rangle. \tag{1.26}$$

---

[2] Other examples include resonance decay and metastable states.

For elastic scattering, the energy is conserved, and the stationary Schrödinger equation can be recast in the form of the **Lippmann–Schwinger equation** [13, 15, 19],

$$|\psi^{\pm}\rangle = |\phi\rangle + \frac{1}{E - H_0 \pm \mathrm{i}\epsilon}\, V|\psi^{\pm}\rangle, \tag{1.27}$$

where ϵ is a positive infinitesimal quantity. The limit $\epsilon \to 0^+$ specifies how the resolvent operator is defined in the presence of the continuous spectrum of H_0 and enforces the appropriate asymptotic boundary conditions. The $+i\epsilon$ prescription corresponds to outgoing (retarded) scattering states, while the $-i\epsilon$ prescription selects incoming (advanced) solutions.

To obtain the coordinate–space representation, the identity operator $\mathbb{1} = \int d^3\mathbf{r}'\, |\mathbf{r}'\rangle\langle\mathbf{r}'|$ in the position basis has been inserted between the resolvent operator and the interaction potential.

In the following, the interaction is assumed to be described by a *local* potential operator, such that

$$\langle\mathbf{r}|V|\mathbf{r}'\rangle = V(\mathbf{r})\, \delta^{(3)}(\mathbf{r} - \mathbf{r}'). \tag{1.28}$$

This assumption is appropriate for most electron–atom and electron–crystal scattering problems treated within single-particle theory. For genuinely non-local interactions, the integral equation retains a similar structure but involves a non-local kernel $\langle\mathbf{r}|V|\mathbf{r}'\rangle$.

In coordinate representation, Eq. (1.27) then becomes

$$\langle\mathbf{r}|\psi^{\pm}\rangle = \langle\mathbf{r}|\phi\rangle + \int \mathrm{d}^3\mathbf{r}' \left\langle\mathbf{r}\middle|\frac{1}{E - H_0 \pm \mathrm{i}\epsilon}\middle|\mathbf{r}'\right\rangle V(\mathbf{r}')\, \langle\mathbf{r}'|\psi^{\pm}\rangle. \tag{1.29}$$

The kernel of this integral equation is the Green's function of the free Hamiltonian, defined as the coordinate-space representation of the resolvent operator. Its explicit form can be obtained by noting that

$$(E - H_0 \pm i0) \left\langle\mathbf{r}\middle|\frac{1}{E - H_0 \pm i0}\middle|\mathbf{r}'\right\rangle = \delta^{(3)}(\mathbf{r} - \mathbf{r}'). \tag{1.30}$$

Introducing

$$G_{\pm}(\mathbf{r}, \mathbf{r}') = \frac{\hbar^2}{2m}\left\langle\mathbf{r}\middle|\frac{1}{E - H_0 \pm i0}\middle|\mathbf{r}'\right\rangle, \qquad E = \frac{\hbar^2 k^2}{2m}, \tag{1.31}$$

one finds that $G_{\pm}$ satisfies the inhomogeneous Helmholtz equation

$$\left(\nabla^2 + k^2\right) G_{\pm}(\mathbf{r}, \mathbf{r}') = -\, \delta^{(3)}(\mathbf{r} - \mathbf{r}'). \tag{1.32}$$

A convenient way to solve Eq. (1.32) is to Fourier transform in the relative coordinate $\mathbf{R} = \mathbf{r} - \mathbf{r}'$:

$$G_\pm(\mathbf{R}) = \int \frac{d^3\mathbf{q}}{(2\pi)^3}\, \tilde{G}_\pm(\mathbf{q})\, e^{i\mathbf{q}\cdot\mathbf{R}}, \tag{1.33}$$

$$\tilde{G}_\pm(\mathbf{q}) = \frac{1}{q^2 - k^2 \mp i0}. \tag{1.34}$$

Therefore,

$$G_\pm(\mathbf{r}, \mathbf{r}') = \int \frac{d^3\mathbf{q}}{(2\pi)^3} \frac{e^{i\mathbf{q}\cdot(\mathbf{r}-\mathbf{r}')}}{q^2 - k^2 \mp i0}. \tag{1.35}$$

Evaluating the integral in Eq. (1.35) (e.g. by performing the angular integration and then computing the remaining radial integral by contour methods) yields

$$G_\pm(\mathbf{r}, \mathbf{r}') = -\frac{1}{4\pi} \frac{e^{\pm ik|\mathbf{r}-\mathbf{r}'|}}{|\mathbf{r}-\mathbf{r}'|}. \tag{1.36}$$

The infinitesimal prescription $\mp i0$ specifies how the poles at $q = \pm k$ are bypassed and selects the boundary condition: G_+ corresponds to an outgoing (retarded) spherical wave, whereas G_- corresponds to an incoming (advanced) spherical wave.

$$G_\pm(\mathbf{r}, \mathbf{r}') = \lim_{\epsilon\to 0^+} \frac{\hbar^2}{2m} \left\langle \mathbf{r} \middle| \frac{1}{E - H_0 \pm \mathrm{i}\epsilon} \middle| \mathbf{r}' \right\rangle = -\frac{1}{4\pi} \frac{e^{\pm \mathrm{i}k|\mathbf{r}-\mathbf{r}'|}}{|\mathbf{r}-\mathbf{r}'|}, \tag{1.37}$$

where the sign of $\pm i\epsilon$ determines the outgoing or incoming spherical-wave boundary conditions.

Substituting Eq. (1.37) into Eq. (1.29), one obtains the integral form of the stationary Schrödinger equation,

$$\langle \mathbf{r}|\psi^\pm\rangle = \langle \mathbf{r}|\phi\rangle - \frac{2m}{\hbar^2} \int \mathrm{d}^3\mathbf{r}' \, \frac{e^{\pm \mathrm{i}k|\mathbf{r}-\mathbf{r}'|}}{4\pi|\mathbf{r}-\mathbf{r}'|} V(\mathbf{r}')\, \langle \mathbf{r}'|\psi^\pm\rangle. \tag{1.38}$$

For scattering, one is primarily interested in the asymptotic region $|\mathbf{r}| \gg |\mathbf{r}'|$, where

$$|\mathbf{r}-\mathbf{r}'| \simeq r - \hat{\mathbf{r}}\cdot\mathbf{r}', \qquad \frac{1}{|\mathbf{r}-\mathbf{r}'|} \simeq \frac{1}{r}, \qquad e^{\pm \mathrm{i}k|\mathbf{r}-\mathbf{r}'|} \simeq e^{\pm \mathrm{i}kr} e^{\mp \mathrm{i}\mathbf{k}'\cdot\mathbf{r}'}, \tag{1.39}$$

with $\mathbf{k}' = k\hat{\mathbf{r}}$. Assuming a localized interaction potential and an incident plane wave $\langle \mathbf{r}|\phi\rangle = e^{\mathrm{i}\mathbf{k}\cdot\mathbf{r}}/L^{3/2}$, the asymptotic form of the scattered wavefunction [3]

---

[3] In scattering theory one selects the + solution of the Lippmann–Schwinger equation because it enforces outgoing-wave boundary conditions. This corresponds to a physically prepared incident state in the remote past that generates a scattered wave propagating towards spatial infinity, consistently with the causal (retarded) Green's function.

$$\langle \mathbf{r}|\psi^+\rangle \simeq \frac{e^{\mathrm{i}\mathbf{k}\cdot\mathbf{r}}}{L^{3/2}} - \frac{2m}{4\pi\hbar^2}\frac{e^{\mathrm{i}kr}}{r}\int \mathrm{d}^3\mathbf{r}'\, e^{-\mathrm{i}\mathbf{k}'\cdot\mathbf{r}'} V(\mathbf{r}')\langle \mathbf{r}'|\psi^+\rangle, \tag{1.40}$$

where L^3 denotes a finite normalization volume introduced to normalize plane–wave states (box normalization); physical observables such as scattering amplitudes and cross sections are independent of L and remain well defined in the limit $L \to \infty$.

The total wavefunction therefore asymptotically takes the form

$$\psi(\mathbf{r}) \underset{r\to\infty}{=} \frac{1}{L^{3/2}}\left[e^{\mathrm{i}\mathbf{k}\cdot\mathbf{r}} + \frac{e^{\mathrm{i}kr}}{r} f(\mathbf{k}',\mathbf{k})\right], \tag{1.41}$$

where $f(\mathbf{k}',\mathbf{k})$ is the *scattering amplitude.* The physical interpretation follows from the probability current associated with the asymptotic wavefunction. The outgoing spherical wave generates a radial probability current proportional to $|f(\mathbf{k}',\mathbf{k})|^2/r^2$, while the incident plane wave carries a uniform incoming flux. The ratio of the scattered flux through a solid angle element $\mathrm{d}\Omega$ to the incident flux defines the differential cross section,

$$\frac{\mathrm{d}\sigma}{\mathrm{d}\Omega} = |f(\mathbf{k}',\mathbf{k})|^2. \tag{1.42}$$

For weak interaction potentials, the wavefunction ψ^+ can be approximated by the incident plane wave inside the integral in Eq. (1.40), leading to the **first Born approximation**,

$$f^{(1)}(\mathbf{k}',\mathbf{k}) = -\frac{1}{4\pi}\frac{2m}{\hbar^2}\int \mathrm{d}^3\mathbf{r}'\, e^{\mathrm{i}(\mathbf{k}-\mathbf{k}')\cdot\mathbf{r}'} V(\mathbf{r}'), \tag{1.43}$$

which corresponds to the Fourier transform of the interaction potential with respect to the momentum transfer $\mathbf{K} = \mathbf{k}' - \mathbf{k}$. This result establishes the direct connection between the microscopic potential landscape and the experimentally observed scattering pattern.

Higher-order corrections are obtained by iterating the Lippmann–Schwinger equation, giving rise to the perturbative expansion of the *transition operator* $\mathcal{T}$,

$$\mathcal{T} = V + V\frac{1}{E - H_0 + \mathrm{i}\epsilon}V + V\frac{1}{E - H_0 + \mathrm{i}\epsilon}V\frac{1}{E - H_0 + \mathrm{i}\epsilon}V + \dots, \tag{1.44}$$

so that the scattering amplitude can be written compactly as

$$f(\mathbf{k}',\mathbf{k}) = -\frac{1}{4\pi}\frac{2m}{\hbar^2}\langle \mathbf{k}'|\mathcal{T}|\mathbf{k}\rangle. \tag{1.45}$$

The successive terms in this expansion correspond to multiple scattering processes in which the electron interacts repeatedly with the potential before emerging into the asymptotic region.

The Lippmann–Schwinger equation thus provides a rigorous bridge between the stationary formalism of scattering theory and its physical time-dependent interpretation. It encapsulates both the asymptotic structure of the scattered wave and the perturbative expansion of the transition operator, establishing the mathematical framework from which all elastic and inelastic scattering observables can be consistently derived.

1.3.2 Connection with the Time-Dependent Picture

Although scattering is naturally a time-dependent process, all experimentally measurable quantities, such as scattering amplitudes and differential cross sections, are determined by stationary solutions. In this subsection, we show explicitly how the time-dependent description reduces to the stationary result in the asymptotic regime.

Consider a short-range potential $V(\mathbf{r})$ and a wave-packet solution of the time-dependent Schrödinger equation,

$$i\hbar\frac{\partial}{\partial t}\Psi(\mathbf{r},t) = (H_0 + V)\,\Psi(\mathbf{r},t), \qquad H_0 = -\frac{\hbar^2}{2m}\nabla^2. \tag{1.46}$$

At $t \to -\infty$, before the interaction takes place, the particle is free and is described by an incident wave packet,

$$\Psi_{\text{in}}(\mathbf{r},t) = \int \mathrm{d}^3\mathbf{k}\, a(\mathbf{k})\, e^{\mathrm{i}(\mathbf{k}\cdot\mathbf{r}-\omega_k t)}, \qquad \omega_k = \frac{E_k}{\hbar} = \frac{\hbar k^2}{2m}, \tag{1.47}$$

where the amplitude $a(\mathbf{k})$ has sharply peaked around a central momentum $\mathbf{k}_0$. This choice ensures a narrow energy spread and allows the incident state to closely approximate a plane wave with the wavevector $\mathbf{k}_0$, while retaining a finite spatial localization and a well-defined incident flux.

The exact time evolution can be expressed as a coherent superposition of stationary scattering states [13, 18, 19]:

$$\Psi(\mathbf{r},t) = \int \mathrm{d}^3\mathbf{k}\, a(\mathbf{k})\, e^{-\mathrm{i}E_k t/\hbar}\, \psi^{(+)}_{\mathbf{k}}(\mathbf{r}), \tag{1.48}$$

where each $\psi^{(+)}_{\mathbf{k}}$ satisfies the stationary Lippmann–Schwinger equation and has the asymptotic form given in Eq. (1.41).

In the far-field region $r \to \infty$, the total wave function decomposes into an incident and a scattered contribution, within the non-relativistic scattering formalism adopted here, is

$$\Psi(\mathbf{r},t) \simeq \underbrace{\int \mathrm{d}^3\mathbf{k}\, a(\mathbf{k})\, e^{\mathrm{i}(\mathbf{k}\cdot\mathbf{r}-\omega_k t)}}_{\Psi_{\mathrm{inc}}} + \frac{1}{r} \underbrace{\int \mathrm{d}^3\mathbf{k}\, a(\mathbf{k})\, f_{\mathbf{k}}(\hat{\mathbf{r}})\, e^{\mathrm{i}(kr-\omega_k t)}}_{\Psi_{\mathrm{sc}}}, \tag{1.49}$$

where, for narrow packets, $f_{\mathbf{k}}(\hat{\mathbf{r}}) \approx f_{\mathbf{k}_0}(\hat{\mathbf{r}}) \equiv f(\hat{\mathbf{r}})$. With the linearization of the phase near k_0, valid for sufficiently narrow wave packets in momentum space, and the introduction of the temporal envelope

$$A\left(t - \frac{r}{v_0}\right) = \int \mathrm{d}^3\mathbf{k}\, a(\mathbf{k})\, e^{\mathrm{i}(k-k_0)(r-v_0 t)}, \qquad v_0 = \frac{\hbar k_0}{m}, \tag{1.50}$$

the scattered packet takes the universal asymptotic form;

$$\Psi_{\mathrm{sc}}(\mathbf{r},t) \simeq \frac{e^{\mathrm{i}(k_0 r-\omega_0 t)}}{r}\, f(\hat{\mathbf{r}})\, A\left(t - \frac{r}{v_0}\right). \tag{1.51}$$

The corresponding radial probability current density is

$$j_{\mathrm{sc}}(r,\hat{\mathbf{r}},t) \simeq \frac{\hbar k_0}{m} \frac{|f(\hat{\mathbf{r}})|^2}{r^2} \big|A(t-r/v_0)\big|^2, \tag{1.52}$$

so that the total number of particles scattered at the solid angle $d\Omega$ is

$$N_{\mathrm{sc}}(\hat{\mathbf{r}}) = \frac{\hbar k_0}{m} |f(\hat{\mathbf{r}})|^2 \int_{-\infty}^{+\infty} \mathrm{d}t\, |A(t-r/v_0)|^2. \tag{1.53}$$

Since the detector is located at a fixed distance r, the time delay r/v_0 is a constant. The time integral of the scattered probability density is therefore invariant under the change of variables $\tau = t - r/v_0$, which corresponds to a rigid time translation of the wave packet.

$$\int_{-\infty}^{+\infty} \mathrm{d}t\, \big|A(t-r/v_0)\big|^2 = \int_{-\infty}^{+\infty} \mathrm{d}\tau\, |A(\tau)|^2. \tag{1.54}$$

For simplicity, the variable τ is relabeled as t in the following.

Similarly, the incident number of incoming particles per unit area is

$$\Phi_{\mathrm{in}} = \frac{\hbar k_0}{m} \int_{-\infty}^{+\infty} \mathrm{d}t\, |A_{\mathrm{in}}(t)|^2. \tag{1.55}$$

In the case of *purely elastic scattering*, in the absence of degeneracies, the scattered packet is obtained from the incident one by unitary time evolution under the full Hamiltonian. Here, the absence of degeneracies refers to the absence of internal or channel degeneracies, i.e. to the case in which the initial and final states are uniquely specified by the asymptotic momentum of the scattered particle. The continuous degeneracy associated with the energy shell in momentum space is implicitly taken into account through the angular dependence of the scattering amplitude.

Unitarity ensures conservation of probability, which in this context means that the temporal envelope has the same total norm before and after the interaction:

$$\int \mathrm{d}t\, |A(t)|^2 = \int \mathrm{d}t\, |A_{\text{in}}(t)|^2. \tag{1.56}$$

Since the group velocity $\hbar k_0/m$ is the same for incident and scattered components in elastic processes, the time integrals appearing in N_{sc} and Φ_{in} cancel exactly, resulting in the following.

$$\boxed{\frac{\mathrm{d}\sigma}{\mathrm{d}\Omega} = \frac{N_{\text{sc}}}{\Phi_{\text{in}}} = |f(\hat{\mathbf{r}})|^2.} \tag{1.57}$$

This shows that all observable information on elastic scattering is encoded in the stationary scattering amplitude $f(\hat{\mathbf{r}})$, independent of the temporal width or detailed profile of the incident packet[4].

When *inelastic channels* are present, the above equality is generalized: unitarity of the scattering operator guarantees conservation of probability only after summing over all final states,

$$\int \mathrm{d}t\, |A_{\text{in}}(t)|^2 = \sum_f \int \mathrm{d}t\, |A_f(t)|^2, \tag{1.58}$$

where the sum runs over elastic and inelastic final channels. Physically, the interaction with $V(\mathbf{r})$ redistributes the probability flux between several outgoing energies rather than preserving it within a single channel. In this multichannel setting, observable predictions involve matrix elements of the transition operator $\mathcal{T}(E)$ or the unitarity relation $\mathcal{S}^\dagger\mathcal{S} = \mathbb{1}$ in the channel space. From a conceptual viewpoint, the stationary Lippmann–Schwinger formalism emerges as the asymptotic limit of the full time–dependent evolution.

The adiabatic prescription in Eq. (1.27) ensures that the interaction potential acts only on outgoing waves, corresponding to the physical condition that the particle is free in the remote past and in the far future [18, 19]. Having established the

---

[4] Possible relativistic corrections can be included, as discussed previously, by multiplying the non-relativistic cross section by the Lorentz factor γ.

equivalence between the time-dependent and time-independent formulations, we now introduce the transition operator $\mathcal{T}(E)$ and the scattering matrix $\mathcal{S}$, which provide a compact and general framework for quantum collision theory [13, 14, 16, 19]. They relate the microscopic interaction potential V to observable quantities such as differential and total cross sections, and rigorously distinguish between elastic and inelastic channels through the unitarity of the $\mathcal{S}$-matrix.

1.4 The $\mathcal{T}$ and $\mathcal{S}$ Operators: Unitarity and Multichannel Scattering

The Lippmann–Schwinger equation provides a natural path to the definition of the *transition operator* $\mathcal{T}(E)$, which compactly encodes all the scattering processes generated by the interaction potential V [13, 15, 26].

Starting from Eq. (1.27), one defines

$$\mathcal{T}(E) = V + V\, G_0^{(+)}(E)\, \mathcal{T}(E), \tag{1.59}$$

where $G_0^{(+)}(E) = (E - H_0 + \mathrm{i}\epsilon)^{-1}$ denotes the free Green's operator enforcing outgoing-wave boundary conditions. The iterative expansion of Eq. (1.59) gives the Born series,

$$\mathcal{T}(E) = V + V\, G_0^{(+)}(E)\, V + V\, G_0^{(+)}(E)\, V\, G_0^{(+)}(E)\, V + \dots, \tag{1.60}$$

each term corresponding to successive interactions of the projectile with the scattering potential, separated by free propagation.

The scattering amplitude between the asymptotic free states $|\varphi_i\rangle = |\mathbf{k}_i\rangle$ and $|\varphi_f\rangle = |\mathbf{k}_f\rangle$ is obtained from the on-shell matrix element of $\mathcal{T}(E)$ as

$$f(\mathbf{k}_f, \mathbf{k}_i) = -\frac{1}{4\pi}\frac{2m}{\hbar^2}\, \langle \mathbf{k}_f | \mathcal{T}(E) | \mathbf{k}_i \rangle, \tag{1.61}$$

from which all differential and total cross sections follow through $\mathrm{d}\sigma/\mathrm{d}\Omega = |f|^2$.

The transition operator $\mathcal{T}(E)$ thus acts as the generator of transitions between scattering channels, encompassing both elastic and inelastic processes in a unified operator framework.

1.4.1 Unitarity of the $\mathcal{S}$–matrix

The asymptotic relation between incoming and outgoing states can be written compactly in terms of the *scattering matrix*:

$$\mathcal{S} = \mathbb{1} + \mathrm{i}\mathcal{T}, \tag{1.62}$$

within the present normalization conventions and where $\mathcal{T}$ is evaluated on the energy shell $E = E_i = E_f$. The unitarity of $\mathcal{S}$,

$$\mathcal{S}^\dagger \mathcal{S} = \mathbb{1}, \tag{1.63}$$

expresses the conservation of the total probability flux across all open channels [13, 19]. For matrix elements between specific initial and final states,

$$\mathcal{S}_{fi} = \delta_{fi} + \mathrm{i}\,\mathcal{T}_{fi}, \tag{1.64}$$

the condition (1.63) implies the general operator identity

$$\mathrm{i}\left(\mathcal{T}_{fi} - \mathcal{T}^\dagger_{fi}\right) = \sum_n \mathcal{T}^\dagger_{fn}\mathcal{T}_{ni}, \tag{1.65}$$

which embodies the redistribution of flux among all possible outgoing channels n. Any reduction of probability in one channel must, therefore, be compensated for by an increase in others. In field–theoretical language, this is the statement that the $\mathcal{S}$–matrix is unitary order by order in perturbation theory.

1.4.2 Elastic and Inelastic Channels

If the final state of the target coincides with its initial configuration ($f = i$), the process is *elastic*: both the total energy and the internal state remain unchanged, and only the direction (and possibly the phase) of the projectile is modified.

When the target is excited or ionized ($f \neq i$), the process is *inelastic*, involving an energy transfer from the projectile to the internal degrees of freedom of the target.

For a given incoming channel i, the unitarity of $\mathcal{S}$ implies

$$\sum_f |\mathcal{S}_{fi}|^2 = 1, \tag{1.66}$$

so that the survival probability in the elastic channel is

$$|\mathcal{S}_{ii}|^2 = 1 - \sum_{f \neq i} |\mathcal{S}_{fi}|^2. \tag{1.67}$$

This explicitly shows that inelastic scattering is not an independent process but rather the *loss of flux* from the elastic channel [17, 18]. The corresponding inelastic cross section (up to kinematic and density-of-states factors absorbed in the definition of $\mathcal{T}$) reads

$$\sigma_{\text{inel}}^{(i)} \propto \sum_{f \neq i} |\mathcal{T}_{fi}|^2 \propto 1 - |\mathcal{S}_{ii}|^2, \tag{1.68}$$

making explicit that the inelastic component quantifies the amount of flux removed from the coherent elastic channel.

1.4.3 Optical Theorem and Forward Scattering

The *optical theorem* provides a direct and remarkably compact connection between the forward elastic scattering amplitude and the total cross section, which includes both elastic and inelastic channels [13, 14, 16, 27].

Consider an incident plane wave of momentum $\mathbf{k}_i$ scattered by a localized potential. In the asymptotic region $r \to \infty$, the wave function can be written as

$$\psi(\mathbf{r}) \simeq e^{\mathrm{i}\mathbf{k}_i \cdot \mathbf{r}} + f(\theta) \frac{e^{\mathrm{i}kr}}{r}, \tag{1.69}$$

where $f(\theta)$ denotes the scattering amplitude and θ is the angle between $\mathbf{k}_i$ and $\mathbf{k}_f$. The corresponding differential cross section is, as introduced above,

$$\frac{\mathrm{d}\sigma}{\mathrm{d}\Omega} = |f(\theta)|^2. \tag{1.70}$$

To obtain the total cross section, one integrates the continuity equation on a spherical surface enclosing the interaction region and makes use of the unitarity condition (1.65). After a straightforward but lengthy derivation, one finds the celebrated result, within the present normalization conventions for the scattering amplitude:

$$\sigma_{\text{tot}} = \frac{4\pi}{k} \operatorname{Im} f(0) = \sigma_{\text{el}} + \sigma_{\text{inel}}, \tag{1.71}$$

where $f(0)$ denotes the forward scattering amplitude ($\theta = 0$) and $k = |\mathbf{k}_i|$.

Thus, the imaginary part of the *forward* amplitude fully determines the *total* removal of flux from the incident beam, regardless of the angular distribution of the scattered particles. This result may at first seem counterintuitive, since forward scattering corresponds to zero scattering angle, yet mathematically it encodes the global depletion of the coherent incident wave.

In the absence of absorption or inelastic channels (i.e. for a real interaction potential and a unitary $\mathcal{S}$–matrix in the elastic subspace), one has $\sigma_{\text{inel}} = 0$ and therefore $\sigma_{\text{tot}} = \sigma_{\text{el}}$. In this purely elastic case, the forward amplitude $f(0)$ is generally complex, and its imaginary part is not a signature of inelasticity by itself: rather, $\operatorname{Im} f(0)$ encodes, through interference between the incident and scattered waves, the total flux removed from the *unscattered* plane-wave component and redistributed into finite scattering angles.

The presence of absorption or genuinely inelastic channels manifests itself instead through a loss of unitarity of the elastic channel alone, so that $\sigma_{\text{inel}} > 0$ and σ_{tot} exceeds the purely elastic contribution. In partial-wave language this corresponds to complex phase shifts or, equivalently, to inelasticity parameters $\eta_\ell < 1$, which quantify the reduction of elastic flux due to coupling to additional channels.

Within the Quantum Field Theory (QFT) formulation, the optical theorem is the statement that the flux lost from the forward direction equals the rate of production of *all other* asymptotic channels. Therefore, the optical theorem represents the most compact and physically transparent expression of unitarity: the imaginary part of $f(0)$ measures the total flux removed from the incident beam, while the difference $\sigma_{\text{tot}} - \sigma_{\text{el}}$ quantifies the net contribution of inelastic processes.

1.4.4 Partial-Wave Expansion and Angular Momentum Channels

For spherically symmetric potentials, scattering decomposes into independent angular momentum channels, or *partial waves* [13, 14, 17]. The wave function can be written as

$$\psi(\mathbf{r}) = \sum_{\ell=0}^{\infty}(2\ell+1)\mathrm{i}^{\ell}\frac{u_\ell(r)}{r}\,P_\ell(\cos\theta), \tag{1.72}$$

where P_ℓ are Legendre polynomials and $u_\ell(r)$ solves the radial Schrödinger equation. At large distances $r \to \infty$, one has

$$u_\ell(r) \sim \frac{1}{2\mathrm{i}}\left[e^{-\mathrm{i}\left(kr-\frac{\ell\pi}{2}\right)} - \mathcal{S}_\ell\, e^{\mathrm{i}\left(kr-\frac{\ell\pi}{2}\right)}\right], \tag{1.73}$$

where the partial-wave $\mathcal{S}$–matrix eigenvalue is parametrized as $\mathcal{S}_\ell = e^{2\mathrm{i}\delta_\ell}$. Here δ_ℓ is in general a *complex* phase shift parameter: its real part δ'_ℓ describes elastic scattering, while the imaginary part $-\eta_\ell$ encodes attenuation due to inelastic channels.

The corresponding element of $\mathcal{S}$–matrix for each angular momentum ℓ is

$$\mathcal{S}_\ell = e^{2\mathrm{i}\delta_\ell} = e^{2\mathrm{i}\delta'_\ell} e^{-2\eta_\ell}, \tag{1.74}$$

with $\eta_\ell \geq 0$. If $\eta_\ell = 0$, the scattering is purely elastic in that channel; if $\eta_\ell > 0$, part of the incident flux is irreversibly transferred to internal excited states. The partial elastic and inelastic cross sections are [14, 17]

$$\sigma_\ell^{(\mathrm{el})} = \frac{\pi}{k^2}(2\ell+1)\,|\mathcal{S}_\ell - 1|^2, \tag{1.75}$$

$$\sigma_\ell^{(\mathrm{inel})} = \frac{\pi}{k^2}(2\ell+1)\,\big(1 - |\mathcal{S}_\ell|^2\big). \tag{1.76}$$

Summing over all ℓ reproduces Eq. (1.68) for a central potential, where each angular momentum channel acts as an independent scattering mode. Formally,

$$\sigma_{\mathrm{inel}} = \frac{\pi}{k^2}\sum_{\ell=0}^{\infty}(2\ell+1)\big(1 - |\mathcal{S}_\ell|^2\big). \tag{1.77}$$

Elastic scattering therefore represents the coherent redirection of the incident flux by the static potential of the target, preserving both energy and phase.

Inelastic scattering, on the contrary, corresponds to irreversible processes in which a fraction of the incident flux modifies the internal state of the target, leading to excitation, ionization, or energy loss. Mathematically, this manifests itself as a deviation of $\mathcal{S}_\ell$ from a pure phase factor, i.e. as $|\mathcal{S}_\ell| < 1$, which signals loss of probability from the elastic channel due to coupling to additional open channels.

In this case the elastic $\mathcal{S}$–matrix alone is no longer unitary, although the full $\mathcal{S}$–matrix in the enlarged channel space remains globally unitary. The total imaginary part of the forward amplitude $f(0)$ measures the overall flux removed from the unscattered beam, while the difference $\sigma_{\mathrm{tot}} - \sigma_{\mathrm{el}}$ provides the direct quantitative measure of genuinely inelastic processes.

1.5 Scattering Amplitudes and Cross Sections

To investigate electron–matter interactions within a rigorous yet analytically tractable framework, it is convenient to begin with the simplest possible target: the hydrogen atom. This case constitutes an invaluable theoretical benchmark, as it allows one to compute scattering amplitudes and cross sections in a closed analytical form, thereby clarifying the physical mechanisms that later reappear in more complex systems. Once the essential features of electron–hydrogen scattering are understood, the same formalism can be extended to realistic, many–electron targets by appropriate modifications of the interaction potential and inclusion of screening effects [13, 14, 19, 24, 28].

We consider an incident electron impinging on a hydrogen atom initially in its ground state ($1s$). The coordinate $\mathbf{r}_1$ denotes the position of the incident (primary) electron, while $\mathbf{r}_2$ denotes the coordinate of the bound electron.[5]

The Hamiltonian of the composite system reads

$$H = K_e + H_H + V \equiv H_0 + V, \tag{1.78}$$

where K_e is the kinetic operator of the projectile, H_H is the hydrogen–atom Hamiltonian acting on $\mathbf{r}_2$, and V describes the interaction between the projectile and the atomic constituents.

Far from the projectile, the hydrogen eigenstates satisfy

$$H_H\, \chi_n(\mathbf{r}_2) = E_n\, \chi_n(\mathbf{r}_2). \tag{1.79}$$

For bound hydrogen states, the energy spectrum is given by

$$E_n = -\frac{Ry}{n^2}, \qquad n = 1, 2, \ldots, \tag{1.80}$$

where $Ry = 13.6$ eV is the Rydberg energy, while the continuum ($E_n > 0$) describes the ionized states of the atom.

The incident electron is represented by a plane wave $\varphi(\mathbf{r}_1) = e^{\mathrm{i}\mathbf{k}_i\cdot\mathbf{r}_1}/L^{3/2}$, an eigenfunction of K_e with eigenvalue $E_e = \hbar^2 k_i^2/(2m)$.

---

[5] Since the incident electron carries kinetic energy much larger than the hydrogen binding energy, the two electrons may be treated as *distinguishable* to an excellent approximation and exchange effects can be neglected at first order. Physically, this follows from the fact that the fast projectile electron has a de Broglie wavelength and a characteristic spatial extent much smaller than that of the bound atomic electron, so that the overlap between their wavefunctions is negligible. As a consequence, antisymmetrization of the two-electron state produces only exponentially small corrections to the scattering amplitude. This approximation reproduces standard results for TEM energies.

Let $\Psi^{(+)}(\mathbf{r}_1, \mathbf{r}_2)$ denote the total wave function of two particles that describes a collision in which the incident electron with momentum $\mathbf{k}_i$ interacts with a hydrogen atom in its ground state $\chi_0(\mathbf{r}_2)$. This function satisfies the following conditions

$$H\,\Psi^{(+)} = E\,\Psi^{(+)} \tag{1.81}$$

and may be written in the Lippmann–Schwinger form

$$\Psi^{(+)}(\mathbf{r}_1, \mathbf{r}_2) = \varphi(\mathbf{r}_1)\chi_0(\mathbf{r}_2) + \iint \mathrm{d}\mathbf{r}_1'\,\mathrm{d}\mathbf{r}_2' \left\langle \mathbf{r}_1, \mathbf{r}_2 \middle| \frac{1}{E - H_0 + i\epsilon} \middle| \mathbf{r}_1', \mathbf{r}_2' \right\rangle V(\mathbf{r}_1', \mathbf{r}_2')\,\Psi^{(+)}(\mathbf{r}_1', \mathbf{r}_2'). \tag{1.82}$$

The Green's operator couples the projectile and atomic subsystems through V.

The two–particle wavefunction can be expanded in a complete basis of atomic eigenstates:

$$\Psi^{(+)}(\mathbf{r}_1, \mathbf{r}_2) = \sum_n \psi_n^{(+)}(\mathbf{r}_1)\,\chi_n(\mathbf{r}_2), \tag{1.83}$$

where $\psi_n^{(+)}(\mathbf{r}_1)$ is the scattering amplitude of the projectile when the target is found in the internal state χ_n. Inserting (1.83) into (1.82), multiplying by χ_n^* and integrating over $\mathbf{r}_2$ yields a hierarchy of coupled–channel integral equations.

The explicit form of the relevant free Green's function matrix element follows from the separability of the free Hamiltonian $H_0 = K_e + H_H$ and from the fact that the atomic eigenstates satisfy $H_H|\chi_n\rangle = E_n|\chi_n\rangle$. Using the completeness of the atomic basis $\{|\chi_n\rangle\}$, one finds

$$\left\langle \chi_n \middle| \frac{1}{E - H_0 + \mathrm{i}\epsilon} \middle| \chi_m \right\rangle = \delta_{nm}\,\frac{1}{E - E_n - K_e + \mathrm{i}\epsilon},$$

so that

$$\left\langle \mathbf{r}_1, \chi_n \middle| \frac{1}{E - H_0 + \mathrm{i}\epsilon} \middle| \mathbf{r}_1', \chi_m \right\rangle = \delta_{nm} \left\langle \mathbf{r}_1 \middle| \frac{1}{E - E_n - K_e + \mathrm{i}\epsilon} \middle| \mathbf{r}_1' \right\rangle.$$

The remaining kernel is the free Green's function of the projectile at energy $E - E_n = \hbar^2 k_f^2/(2m)$, whose coordinate–space form is

$$\left\langle \mathbf{r}_1 \middle| \frac{1}{E - E_n - K_e + \mathrm{i}\epsilon} \middle| \mathbf{r}_1' \right\rangle = -\frac{m}{2\pi\hbar^2}\,\frac{e^{\mathrm{i}k_f|\mathbf{r}_1 - \mathbf{r}_1'|}}{|\mathbf{r}_1 - \mathbf{r}_1'|}.$$

$$\left\langle \mathbf{r}_1, \chi_n \middle| \frac{1}{E - H_0 + \mathrm{i}\epsilon} \middle| \mathbf{r}_1', \chi_m \right\rangle = -\delta_{nm}\,\frac{m}{2\pi\hbar^2}\,\frac{e^{\mathrm{i}k_f|\mathbf{r}_1 - \mathbf{r}_1'|}}{|\mathbf{r}_1 - \mathbf{r}_1'|}, \tag{1.84}$$

where $E_f - E_i = E_{\text{loss}}$ is the energy transferred to the target.[6] Here k_f denotes the projectile wave number in the final channel n, defined by $\hbar^2 k_f^2/(2m) = E - E_n$. In the elastic channel one has $|\mathbf{k}_i| = |\mathbf{k}_f|$, and therefore $E_{\text{loss}} = 0$.

The resulting equation takes the form

$$\psi_n^{(+)}(\mathbf{r}_1) = \varphi(\mathbf{r}_1)\,\delta_{n0} - \frac{m}{2\pi\hbar^2}\sum_m \int \mathrm{d}\mathbf{r}_1' \int \mathrm{d}\mathbf{r}_2\, \frac{e^{\mathrm{i}k_f|\mathbf{r}_1-\mathbf{r}_1'|}}{|\mathbf{r}_1-\mathbf{r}_1'|}\,\chi_n^*(\mathbf{r}_2)\,V(\mathbf{r}_1',\mathbf{r}_2)\,\chi_m(\mathbf{r}_2)\,\psi_m^{(+)}(\mathbf{r}_1'). \tag{1.85}$$

Here $\chi_m(\mathbf{r}_2)$ denotes the internal eigenstate of the target atom, which depends only on the bound–electron coordinate $\mathbf{r}_2$, while $\mathbf{r}_1$ and $\mathbf{r}_1'$ refer to the projectile coordinates.

In the *first Born approximation*, valid whenever the interaction potential is weak compared to the kinetic energy of the incident electron, one replaces $\psi_m^{(+)} \to \varphi$ inside the integral. Taking the far–field limit yields

$$\psi_n^{(+)}(\mathbf{r}_1) = \varphi(\mathbf{r}_1)\,\delta_{n0} - \frac{m}{2\pi\hbar^2}\frac{e^{\mathrm{i}k_f r_1}}{r_1}\sum_m \iint \mathrm{d}\mathbf{r}_1'\,\mathrm{d}\mathbf{r}_2\; e^{-\mathrm{i}\mathbf{k}_f\cdot\mathbf{r}_1'}\,\chi_n^*(\mathbf{r}_2)\,V(\mathbf{r}_1',\mathbf{r}_2)\,\chi_m(\mathbf{r}_2)\,\varphi(\mathbf{r}_1'). \tag{1.86}$$

Equation (1.86) is the two–particle generalization of the single–particle Born approximation and provides the starting point for computing both elastic and inelastic scattering amplitudes.

To proceed, the interaction potential $V(\mathbf{r}_1, \mathbf{r}_2)$ must be specified. At TEM energies, relativistic corrections primarily influence the Coulomb term through Lorentz contraction of electric fields [29, 30, 31]. A convenient model is therefore

$$V(\mathbf{r}_1,\mathbf{r}_2) = \frac{\gamma e^2}{4\pi\epsilon_0|\mathbf{r}_1-\mathbf{r}_2|} - \frac{\gamma e^2}{4\pi\epsilon_0|\mathbf{r}_1|}, \qquad (Z=1), \tag{1.87}$$

which expresses the difference between electron–electron repulsion and electron–nucleus attraction, both scaled by the Lorentz factor γ associated with the fast projectile.[7]

---

[6] The conservation of the total energy and momentum holds before and after the collision. In the nonrelativistic regime, one has $E = \hbar^2k^2/2m$, whereas for relativistic electrons $E = \sqrt{\hbar^2k^2c^2 + m^2c^4}$.

[7] In multi–electron targets, the bare Coulomb interaction $e^2/(4\pi\epsilon_0 r)$ between the projectile and the atomic electrons is modified in two systematic ways. (i) *Static screening:* the nuclear charge is partially shielded by the surrounding electron cloud, leading to an effective potential that decays faster than $1/r$ at large distances. (ii) *Exchange effects:* since all electrons are indistinguishable

This effective form captures the dominant relativistic enhancement of the longitudinal Coulomb interaction at high projectile velocities, while neglecting fully covariant QED corrections. Within the first Born framework, three fundamental scattering channels may occur:

1. **Elastic scattering:** $e^- + H \to e^- + H$, where the atom remains in its ground state.
2. **Inelastic excitation:** $e^- + H \to e^- + H^*$, where the atom is promoted to an excited bound state.
3. **Inelastic ionization:** $e^- + H \to 2e^- + H^+$, corresponding to the ejection of the bound electron into the continuum.

In the ionization channel, the two outgoing electrons are distinguished by their energies: the scattered projectile retains most of the incident beam energy, while the ejected (secondary) electron carries the excess energy above the ionization threshold I. Energy conservation in the ionization channel can be written in the explicit form

$$E_{\text{beam}} = E'_{\text{beam}} + E_{\text{kin}}^{(\text{sec})} + I, \tag{1.88}$$

where E'_{beam} denotes the kinetic energy of the scattered projectile after the collision, $E_{\text{kin}}^{(\text{sec})}$ is the kinetic energy of the ejected (secondary) electron, and I is the ionization energy of the target. Equivalently, the total energy loss of the incident electron is

$$E_{\text{loss}} = E_{\text{beam}} - E'_{\text{beam}} = I + E_{\text{kin}}^{(\text{sec})}. \tag{1.89}$$

Together with elastic scattering and bound-state excitation, these processes constitute the basic interaction channels of electron–atom scattering. Their respective cross sections determine how the incident beam redistributes flux among elastic and inelastic final states, thereby governing image contrast, energy–loss spectra, and beam-induced damage mechanisms. In the following sections, explicit analytical expressions for the elastic and inelastic scattering amplitudes will be derived, providing the quantitative foundation for the microscopic-to-macroscopic connection developed throughout this thesis.

---

fermions, the scattering wavefunction must be anti–symmetrized, giving rise to additional “exchange” terms in the interaction. These corrections are negligible for hydrogen but become essential for many–electron targets.

1.6 Scattering Amplitudes in the First Born Approximation

We now apply the formalism derived in Eq. (1.86) to explicit calculations of elastic, excitation, and ionization scattering in hydrogen. These three channels represent the fundamental interaction mechanisms between a fast electron and a hydrogenic center. Within the first Born approximation, they can be treated on equal footing, yielding closed analytic expressions for the corresponding scattering amplitudes and cross sections. Unless otherwise stated, incident and scattered momenta k_i and k_f are relativistic, defined through $E = \sqrt{\hbar^2 k^2 c^2 + m^2 c^4}$, and plane waves are normalized in a finite box of volume L^3, as discussed above.

Within the present formulation, relativistic effects associated with the fast incident electron are incorporated through the effective interaction potential V, which includes the Lorentz factor γ. For clarity, we introduce the quantity f_{NR}, defined as the scattering amplitude obtained from the same expressions by formally removing the relativistic enhancement, such that

$$f = \gamma\, f_{\mathrm{NR}}. \tag{1.90}$$

Accordingly, all scattering cross sections explicitly display the global kinematic factor γ^2, while f_{NR} contains the purely quantum–mechanical Coulomb scattering contribution.

In some parts of this thesis, the intermediate expressions are written in their non-relativistic form. In this case, the extension to the relativistic regime is straightforward and amounts to a simple multiplicative rescaling by γ at the level of the scattering amplitude (and by γ^2 for the corresponding cross sections).

Case 1: Elastic Scattering

In elastic scattering, the atom remains in its ground state, $\chi_f = \chi_0$. Inserting χ_0 into Eq. (1.86) gives

$$f(\mathbf{k}_i, \mathbf{k}_f) = -\frac{m}{2\pi\hbar^2} \iint \mathrm{d}\mathbf{r}_1\, \mathrm{d}\mathbf{r}_2\, e^{-\mathrm{i}\mathbf{k}_f\cdot\mathbf{r}_1}\, \chi_0^*(\mathbf{r}_2)\, V(\mathbf{r}_1, \mathbf{r}_2)\, \varphi_{\mathbf{k}_i}(\mathbf{r}_1)\, \chi_0(\mathbf{r}_2), \tag{1.91}$$

with $\varphi_{\mathbf{k}_i}(\mathbf{r}_1) = e^{\mathrm{i}\mathbf{k}_i\cdot\mathbf{r}_1}/L^{3/2}$, and $\chi_0(\mathbf{r}_2) = e^{-r_2/a_0}/\sqrt{\pi a_0^3}$. Here a_0 denotes the Bohr radius, defined as

$$a_0 = \frac{4\pi\varepsilon_0\hbar^2}{me^2}, \tag{1.92}$$

where ε_0 is the vacuum permittivity, $\hbar$ the reduced Planck constant, m the electron mass, and e the elementary charge. Its numerical value is

$$a_0 \simeq 5.291\,772\,109 \times 10^{-11}\,\text{m}. \tag{1.93}$$

Using the potential in Eq. (1.87) and introducing momentum transfer $\mathbf{K} = \mathbf{k}_i - \mathbf{k}_f$, we obtain the following

$$f(\mathbf{k}_i, \mathbf{k}_f) = -\frac{\gamma m}{2\pi\hbar^2}\frac{1}{L^{3/2}\,\pi a_0^3}\iint \mathrm{d}\mathbf{r}_1\,\mathrm{d}\mathbf{r}_2\; e^{i\mathbf{K}\cdot\mathbf{r}_1}\left[\frac{e^2}{4\pi\epsilon_0|\mathbf{r}_1 - \mathbf{r}_2|} - \frac{e^2}{4\pi\epsilon_0|\mathbf{r}_1|}\right] e^{-2r_2/a_0}. \tag{1.94}$$

Integration over $\mathbf{r}_1$ produces the standard Coulomb factor $1/K^2$, showing that small–angle scattering (small K) dominates elastic processes. After integrating over $\mathbf{r}_2$ in spherical coordinates, one obtains

$$f(\mathbf{K}) = \frac{\gamma\, a_0}{2}\left[\frac{1}{1 + (a_0 K/2)^2} + \frac{1}{\left[1 + (a_0 K/2)^2\right]^2}\right]. \tag{1.95}$$

The corresponding differential and total elastic cross sections are

$$\frac{\mathrm{d}\sigma_{\text{el}}}{\mathrm{d}\Omega} = |f(K)|^2, \tag{1.96}$$

$$\sigma_{\text{el}} = 2\pi\int_0^{\pi} |f(K)|^2 \sin\theta\,\mathrm{d}\theta. \tag{1.97}$$

Representative numerical values (typical TEM conditions)

To provide an order-of-magnitude estimate, we consider electron energies representative of conventional TEM and STEM experiments, in the range $V = 100$–300 keV. The relativistic factor is $\gamma = 1 + eV/(m_e c^2)$, while the relativistic de Broglie wavelength is $\lambda = h/\sqrt{2m_e eV\,[1 + eV/(2m_e c^2)]}$. For small scattering angles ($\theta \ll 1$), the momentum transfer reduces to $K \simeq k\theta$, with $k = 2\pi/\lambda$.

A characteristic angular scale is set by $a_0 K/2 \sim 1$, yielding $\theta_c \simeq 1/(k a_0)$. This gives $\theta_c \approx 11$ mrad at 100 keV, $\theta_c \approx 7.5$ mrad at 200 keV, and $\theta_c \approx 5.9$ mrad at 300 keV, which confirms that elastic scattering is strongly dominated by small angles.

As a representative differential value, for $V = 200$ keV and $\theta = 10$ mrad one finds

$$\left.\frac{\mathrm{d}\sigma_{\text{el}}}{\mathrm{d}\Omega}\right|_{\theta=10\ \text{mrad}} \simeq 2\times 10^{-21}\ \text{m}^2/\text{sr} \simeq 2\times 10^{7}\ \text{barn/sr},$$

Table 1.1: Elastic scattering cross sections for hydrogen under typical TEM conditions. The partial cross section $\sigma_{\mathrm{el}}(\theta \leq \theta_{\mathrm{max}})$ is obtained by integrating Eq. (1.95) up to the collection semi-angle θ_{max}.

V (keV)	θ_{max} (mrad)	σ_{el} (m^2)	σ_{el} (barn)
100	10	1.6×10^{-24}	1.6×10^{4}
100	50	3.4×10^{-24}	3.4×10^{4}
200	10	1.0×10^{-24}	1.0×10^{4}
200	50	2.2×10^{-24}	2.2×10^{4}
300	10	7.5×10^{-25}	7.5×10^{3}
300	50	1.6×10^{-24}	1.6×10^{4}

which reflects the strongly forward-peaked angular distribution of Coulomb (Rutherford) scattering, with most of the elastic cross section arising from scattering angles below a few tens of milliradians.

These estimates show that, for realistic TEM collection angles of a few tens of milliradians, elastic scattering cross sections are of the order of 10^3–10^4 barn, with the dominant contribution arising from the small-angle region $\theta \lesssim 10$ mrad.

Case 2: Excitation ($1s \to 2s$)

For excitation, the final atomic state is $\chi_f = \chi_{2s}$. In this case, the electron–nucleus part of the potential gives no contribution because of orthogonality of the bound states, $\int \chi_0^*(\mathbf{r}_2)\chi_{2s}(\mathbf{r}_2)\,\mathrm{d}\mathbf{r}_2 = 0$, so only electron–electron repulsion contributes. Using the explicit hydrogenic form of χ_{2s} and performing the integrations as in the elastic case yields the analytic amplitude

$$f_{\mathrm{NR}}(K) = \frac{512\sqrt{2}\,a_0}{\left(9 + 4a_0^2K^2\right)^3}. \tag{1.98}$$

The factor k_f/k_i reflects flux conservation between non–equal energies of the incoming and outgoing electrons:

$$\frac{\mathrm{d}\sigma_{\mathrm{exc}}}{\mathrm{d}\Omega} = \frac{k_f}{k_i}\,|f(K)|^2, \tag{1.99}$$

$$\sigma_{\mathrm{exc}} = 2\pi\,\frac{k_f}{k_i}\int_0^{\pi} |f(K)|^2 \sin\theta\,\mathrm{d}\theta. \tag{1.100}$$

Table 1.2: Representative total excitation cross sections for the $1s \to 2s$ transition in hydrogen under typical TEM/STEM conditions, computed within the first Born approximation. Relativistic kinematic corrections are included through relativistic momenta and the flux factor k_f/k_i. The excitation energy is $\Delta E = 10.2$ eV. For comparison, the ratio between excitation and elastic cross sections is also reported.

E_{beam} (keV)	γ	$1 - k_f/k_i$	σ_{exc} ($10^{-24}\,\text{m}^2$)	σ_{el} ($10^{-24}\,\text{m}^2$)	$\sigma_{\text{exc}}/\sigma_{\text{el}}$
100	1.195	1.0×10^{-4}	0.862	3.57	0.241
200	1.391	5.0×10^{-5}	0.338	2.82	0.120
300	1.587	3.0×10^{-5}	0.135	2.58	0.052

Table 1.2 reports representative total excitation cross sections for the $1s \to 2s$ transition under typical TEM conditions, highlighting their relative magnitude compared to the elastic channel.

Case 3: Ionization

For ionization, an electron is ejected into the continuum and its wavefunction is described by a Coulomb continuum state [13, 14, 26, 29, 30, 32]:

$$\chi_s(\mathbf{r}_2) = \frac{e^{\mathrm{i}\mathbf{k}_s\cdot\mathbf{r}_2}}{L^{3/2}}\, e^{\pi/(2a_0k_s)}\,\Gamma\!\left(1 + \frac{\mathrm{i}}{a_0k_s}\right)\, {}_1F_1\!\left(-\frac{\mathrm{i}}{a_0k_s}; 1; -\mathrm{i}(k_sr_2 + \mathbf{k}_s\cdot\mathbf{r}_2)\right). \tag{1.101}$$

Here $\Gamma(z)$ denotes the Euler gamma function, which naturally appears in the normalization of Coulomb continuum states, while ${}_1F_1(a; b; z)$ is the confluent hypergeometric function of the first kind (Kummer function). The latter accounts for the distortion of the outgoing electron wavefunction due to the long–range Coulomb interaction with the residual ionic core [13, 14, 29].

Substituting this form into Eq. (1.86) yields a rather cumbersome integral, which can be evaluated most efficiently in parabolic coordinates (ξ, η, φ):

$$x = \sqrt{\xi\eta}\cos\varphi, \qquad y = \sqrt{\xi\eta}\sin\varphi, \qquad z = (\xi - \eta)/2.$$

The detailed derivation, involving Bessel-function expansions and confluent hypergeometric identities, is reported in the Appendix A. The final analytical expression for the ionization amplitude is

$$f(\mathbf{k}_i, \mathbf{k}_f, \mathbf{k}_s) = \frac{2^5 \sqrt{\pi}\, \gamma\, a_0^{3/2}}{L^{3/2} q}\, \Gamma\left(1 - \frac{\mathrm{i}}{a_0 k_s}\right) e^{\pi/(2a_0 k_s)} \big\{ \big[(1 + a_0 k_s)^2 - a_0^2 K^2\big]^{-\frac{\mathrm{i}}{a_0 k_s} - 1}$$

$$\times\ \big[-1 - a_0^2(k_s^2 + K^2) + 2a_0^2 k_s K \cos\theta_{Ks}\big]^{\frac{\mathrm{i}}{a_0 k_s} - 2} \big[a_0 K - (\mathrm{i} + a_0 k_s) \cos\theta_{Ks}\big] \big\}. \quad (1.102)$$

The corresponding *triple differential cross section* (TDCS), which accounts for the number of available final states of the ejected electron, is[8]

$$\frac{\mathrm{d}\sigma_{\mathrm{ion}}}{\mathrm{d}\Omega\, \mathrm{d}^3\mathbf{k}_s} = \frac{k_f}{k_i}\, |f(\mathbf{K}, \mathbf{k}_s)|^2\, \frac{L^3}{(2\pi)^3}. \quad (1.103)$$

Integrating over the solid angle of the secondary electron yields the *double differential cross section* (DDCS):

$$\frac{\mathrm{d}\sigma_{\mathrm{ion}}}{\mathrm{d}\Omega\, \mathrm{d}k_s} = \frac{k_f}{k_i}\, 2^{10}\, k_s \frac{a_0^2}{K^2} \frac{e^{-\frac{2}{a_0 k_s} \arctan\left(\frac{2a_0 k_s}{a_0^2(K^2 - k_s^2) + 1}\right)}}{1 - e^{-2\pi/(a_0 k_s)}} \frac{\big[1 + a_0^2(k_s^2 + 3K^2)\big]}{3\big[1 + a_0^4(k_s^2 - K^2)^2 + 2a_0^2(k_s^2 + K^2)\big]^3}. \quad (1.104)$$

The total ionization cross section follows from integration over both the primary scattering angle and the ejected electron momentum:

$$\sigma_{\mathrm{ion}} = \int_0^{\pi} \int_0^{k_s^{\max}} k_s^2 \frac{\mathrm{d}\sigma_{\mathrm{ion}}}{\mathrm{d}\Omega\, \mathrm{d}k_s} \sin\theta\, \mathrm{d}\theta\, \mathrm{d}k_s. \quad (1.105)$$

The upper integration limit $k_s^{\max}$ is determined by energy conservation:

$$E_i + mc^2 = E_f + E_s + I, \quad (1.106)$$

where E_f denotes the total relativistic energy of the scattered projectile. Its value is not an independent integration variable, but is uniquely fixed by energy conservation for given scattering angle θ and secondary-electron momentum k_s. The minimum allowed value corresponds to $E_f = mc^2$, i.e. a vanishing final kinetic energy of the projectile.

Representative total ionization cross sections under typical TEM conditions are summarized in Table 1.3.

---

[8] The appearance of the factor L^3 in the TDCS is a direct consequence of the box normalization adopted for plane-wave continuum states. Specifically, we take $\langle \mathbf{r}|\mathbf{k}\rangle = L^{-3/2} e^{i\mathbf{k}\cdot\mathbf{r}}$, so that continuum sums are replaced by $\sum_{\mathbf{k}} \to \frac{L^3}{(2\pi)^3} \int d^3\mathbf{k}$. With this convention, the ionization amplitude $f(\mathbf{k}_i, \mathbf{k}_f, \mathbf{k}_s)$ in Eq. (1.102) scales as $L^{-3/2}$, and therefore $|f|^2 \propto L^{-3}$. Multiplication by the density-of-states factor $L^3/(2\pi)^3$ in the TDCS cancels the quantization volume exactly, yielding a physical cross section that is independent of L.

Table 1.3: Total ionization cross section of the hydrogen atom under typical TEM/STEM conditions, computed within the first Born approximation. Relativistic kinematic corrections are included through the Lorentz factor γ and relativistic momenta. Nuclear recoil is neglected. The ratio $\sigma_{\mathrm{ion}}/\sigma_{\mathrm{el}}$ is computed with σ_{el} the *total* elastic cross section integrated over the full solid angle.

E_{beam} (keV)	γ	k_s^{max} (m^{-1})	σ_{ion} ($10^{-23}\,\mathrm{m}^2$)	$\sigma_{\mathrm{ion}}/\sigma_{\mathrm{el}}$
100	1.195	1.18×10^{12}	2.6	0.074
200	1.391	1.67×10^{12}	1.8	0.075
300	1.587	2.04×10^{12}	1.3	0.068

It is worth emphasizing that Table 1.2 reports the cross section for a single discrete bound–bound channel ($1s \to 2s$) and therefore represents only a subset of the total excitation spectrum of hydrogen. Table 1.3, instead, reports the *total* ionization cross section, which provides the dominant contribution to the overall inelastic signal under typical TEM/STEM conditions. Consequently, at $E_{\mathrm{beam}} = 100$ keV the combined inelastic cross section obtained by summing the $1s \to 2s$ excitation and ionization channels exceeds the total elastic cross section by a factor of several, consistent with empirical trends indicating that the inelastic-to-elastic cross section ratio scales approximately as $18/Z$ for low-Z systems [20].

The dependence of the total ionization cross section on the incident electron energy is shown in Fig. 1.1. The curve exhibits the characteristic behavior observed in both theoretical and experimental studies: a rapid rise above threshold, followed by a broad maximum at intermediate energies and a slow decrease at high energies due to the increasing transparency of the target to fast projectiles.

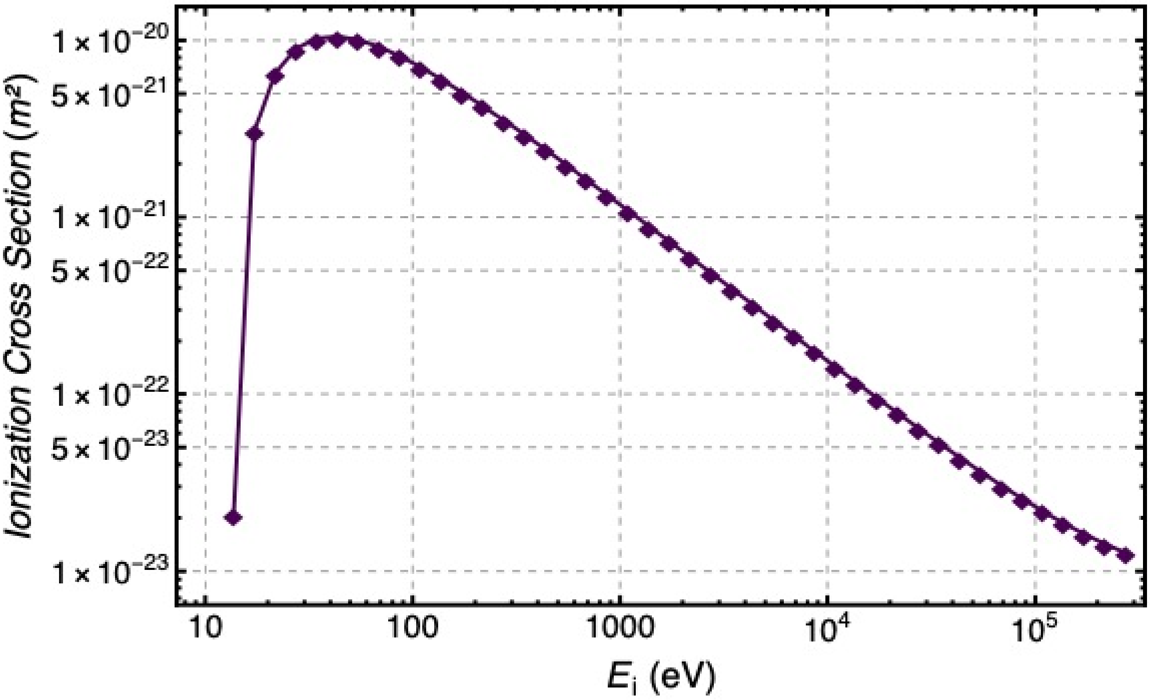

Figure 1.1: Total ionization cross section of atomic hydrogen in the first Born approximation as a function of the incident electron energy E_i. The cross section is obtained by integrating the double differential cross section (1.104) over the full solid angle and over all kinematically allowed secondary electron momenta. Relativistic kinematics are included through the Lorentz factor γ.

1.7 Extension to multi–electron targets: the Carbon atom

After establishing and validating the scattering formalism for the hydrogen atom, the same theoretical framework is applied to the carbon atom. This step represents a natural but non–trivial generalization, since carbon is a multi–electron system whose description inevitably requires additional approximations compared to the single–electron hydrogen case.

In hydrogen, the availability of exact bound and continuum eigenstates ensures a consistent and internally orthogonal description of both elastic and inelastic scattering processes. For multi–electron atoms, instead, the use of effective one–electron potentials and approximate atomic orbitals becomes unavoidable.
While such approaches are widely employed and often successful, they introduce model–dependent assumptions whose range of validity must be carefully assessed.

From a fundamental point of view, the difficulty in extending the hydrogenic formalism to multi–electron atoms originates from the structure of the electronic

Hamiltonian.

For an atom with N electrons, the non–relativistic electronic Hamiltonian reads

$$\hat{H} = \sum_{i=1}^{N} \left(-\frac{\hbar^2}{2m_e} \nabla_i^2 - \frac{Ze^2}{4\pi\varepsilon_0 r_i} \right) + \sum_{i<j}^{N} \frac{e^2}{4\pi\varepsilon_0 |\mathbf{r}_i - \mathbf{r}_j|}, \tag{1.107}$$

where the last term explicitly accounts for electron–electron Coulomb repulsion. The presence of this interaction term couples different electronic coordinates and prevents the exact separation of the many–electron Schrödinger equation into independent single–particle equations. As a consequence, the total electronic wavefunction cannot be written as a simple product of hydrogen–like orbitals, and correlation effects play a fundamental role in determining both bound and continuum states.

In addition, since electrons are indistinguishable fermions, the total electronic wavefunction must satisfy the Pauli exclusion principle and be antisymmetric under the exchange of any two particles. This requirement further constrains the structure of the many–electron state and reinforces the impossibility of a naive factorization into independent single–electron wavefunctions. In independent–particle approaches such as Hartree–Fock theory, antisymmetry is enforced by expressing the total wavefunction as a Slater determinant of single–electron spin–orbitals. Here $\varphi_i(\mathbf{r})$ denotes a *spin–orbital*, i.e. a single–electron wavefunction defined on the combined space and spin coordinates,

$$\varphi_i(\mathbf{r}, \sigma) = \psi_i(\mathbf{r})\, \chi_i(\sigma), \tag{1.108}$$

where $\psi_i(\mathbf{r})$ is a spatial orbital and $\chi_i(\sigma)$ is a two–component spin function (α or β). Each spin–orbital therefore specifies both the spatial distribution and the spin state of a single electron.

$$\Psi(\mathbf{r}_1, \ldots, \mathbf{r}_N) = \frac{1}{\sqrt{N!}} \begin{vmatrix} \varphi_1(\mathbf{r}_1) & \varphi_2(\mathbf{r}_1) & \cdots & \varphi_N(\mathbf{r}_1) \\ \varphi_1(\mathbf{r}_2) & \varphi_2(\mathbf{r}_2) & \cdots & \varphi_N(\mathbf{r}_2) \\ \vdots & \vdots & \ddots & \vdots \\ \varphi_1(\mathbf{r}_N) & \varphi_2(\mathbf{r}_N) & \cdots & \varphi_N(\mathbf{r}_N) \end{vmatrix}. \tag{1.109}$$

While this construction guarantees the correct fermionic symmetry, it also highlights that the orbitals entering the determinant are not exact hydrogenic eigenstates, but effective quantities determined self–consistently by the mean field generated by all electrons. Exchange and correlation effects are therefore intrinsically entangled with the choice of the orbital basis, further complicating the extension of hydrogen–based scattering models to multi–electron atoms.

In practical calculations, these difficulties are commonly addressed by introducing effective one–electron descriptions, such as Hartree–Fock or density functional theory (DFT) [33], which replace the explicit electron–electron interaction with an effective potential. Within DFT in particular, quantitatively reliable predictions for excitation and ionization processes in carbon can be achieved, including orbital hybridization and correlation effects. However, the formalism underlying such approaches is fundamentally different from the analytical scattering framework developed in this thesis and would require a fully numerical treatment beyond its intended scope.

In this chapter, three different electron–carbon scattering processes are considered: elastic scattering, excitation, and ionization. Each process is treated using a level of approximation chosen to retain analytical tractability while capturing the dominant physical mechanisms.

For elastic scattering, the interaction between the incident electron and the target atom is described by an effective screened Coulomb potential, accounting for the average screening of the nuclear charge by bound electrons. In particular, a Yukawa–type potential is adopted, following the formulation proposed by Egerton [20].

Hydrogen–like orbitals corrected by Clementi–Raimondi parameters [34, 35] are employed to model the core electronic states involved in excitation and ionization processes.

Although more refined self–consistent Hartree–Fock or Dirac–Fock potentials exist, the present choice provides a convenient compromise between physical realism and analytical simplicity within the first Born approximation.

The purpose of the present analysis is therefore not to compete with state–of–the–art *ab initio* methods. Rather, it aims to test the extent to which the hydrogen–based scattering formalism can be meaningfully extended to a multi–electron target and to identify the physical limitations arising from simplified one–electron models.

As will be shown in the following sections, while the elastic scattering channel can be described in a reasonably consistent way, the inelastic excitation and ionization processes exhibit significant discrepancies with respect to experimental expectations, such as those observed in EELS measurements. These discrepancies do not indicate a failure of the theoretical approach itself, but rather highlight the intrinsic limitations of simplified one–electron descriptions when applied to deep–core processes in multi–electron atoms.

For this reason, the results presented in this chapter should be regarded not only as quantitative calculations, but also as a systematic exploration of the domain of validity of the adopted theoretical framework, providing insight into the physical ingredients that must be included in more refined models.

1.7.1 Elastic scattering: $e^- + C \rightarrow e^- + C$

The expression for the scattering amplitude in the first Born approximation for a carbon atom is obtained by a direct generalization of Eq. (1.91), with the interaction potential derived from the multi–electron Hamiltonian in Eq. (1.107), namely

$$f(\mathbf{k}_i, \mathbf{k}_f) = -\frac{m\gamma}{2\pi\hbar^2} \int \mathrm{d}\mathbf{r}_1 \int \mathrm{d}\mathbf{r}_2 ... \int \mathrm{d}\mathbf{r}_7 \; e^{\mathrm{i}\mathbf{K}\cdot\mathbf{r}_1} \; \Psi_C^{f\,*}(\mathbf{r}_2...\mathbf{r}_7) V(\mathbf{r}_1...\mathbf{r}_7) \Psi_C^i(\mathbf{r}_2...\mathbf{r}_7) \tag{1.110}$$

where again $\mathbf{K} = \mathbf{k}_i - \mathbf{k}_f$ is the momentum transfer, $\mathbf{r}_1$ is the coordinate of the primary beam electron, $\mathbf{r}_2...\mathbf{r}_7$ are the coordinates of the bound electrons and where $V(\mathbf{r}_1, \ldots, \mathbf{r}_7)$ denotes the full Coulomb interaction between the incident electron, the nucleus, and the bound electrons [20, 24].

In the elastic process $\Psi_C^f(\mathbf{r}_2...\mathbf{r}_7) = \Psi_C^i(\mathbf{r}_2...\mathbf{r}_7)$ and we can suppose that the primary electron will see a positive nuclear charge screened by six bound electrons. Therefore, we may formally define

$$V_{\text{eff}}(\mathbf{r}_1) = \int \mathrm{d}\mathbf{r}_1 \int \mathrm{d}\mathbf{r}_2 \cdots \int \mathrm{d}\mathbf{r}_7 \; \Psi_C^*(\mathbf{r}_2...\mathbf{r}_7) \; V(\mathbf{r}_1...\mathbf{r}_7) \; \Psi_C(\mathbf{r}_2...\mathbf{r}_7). \tag{1.111}$$

In order to express V_{eff} in a form that can be used within the Born approximation, we may adopt the following expression (see [20])

$$V_{\text{eff}}(r_1) = \frac{Ze^2}{4\pi\epsilon_0 r_1} e^{-r_1/a_0 Z^{-1/3}}. \tag{1.112}$$

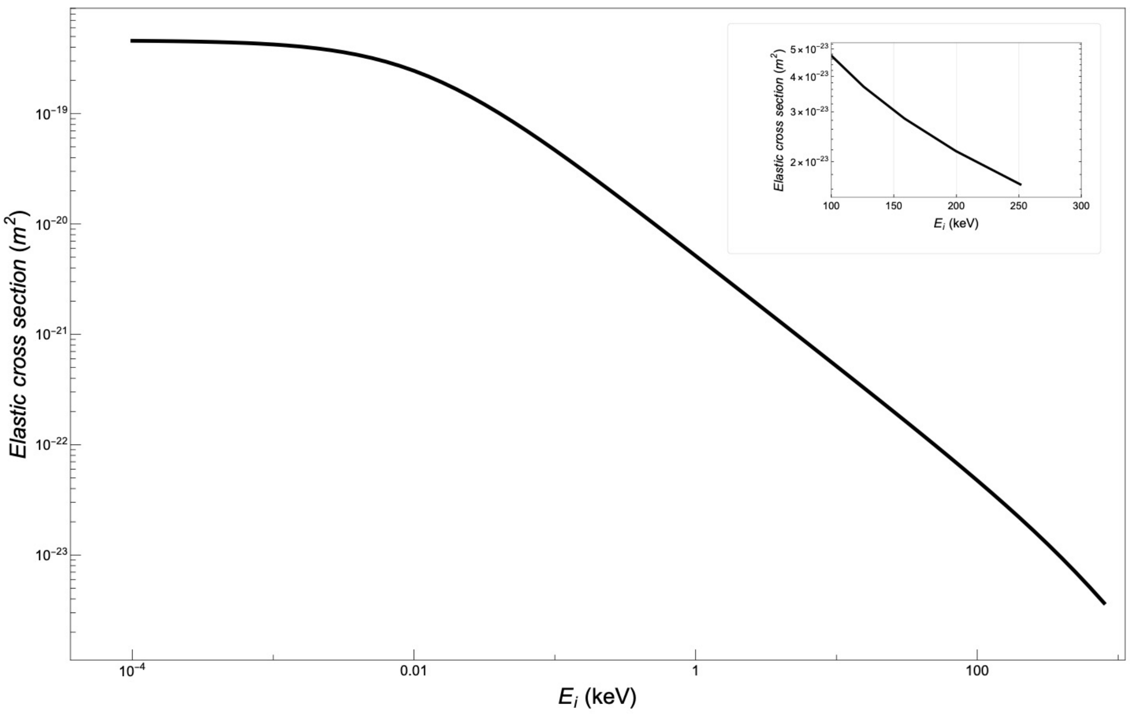

Figure 1.2: Total elastic cross section of a carbon atom as a function of the primary electron energy E_i, calculated within the first Born approximation. The shaded region and the inset highlight the energy range between 100 and 300 keV, corresponding to electron wavevectors $k \sim 10^{11}$–10^{12} m^{-1}.

Eq. (1.91) then becomes

$$f^{\mathrm{EL}}(K) = -\frac{m\gamma}{2\pi\hbar^2}\int \mathrm{d}\mathbf{r}_1\, e^{i\mathbf{K}\cdot\mathbf{r}_1}\, V_{\mathrm{eff}}(r). \tag{1.113}$$

with $Z = 6$. Since the effective potential is spherically symmetric, we may repeat the calculation made for the hydrogen atom. This gives us

$$f^{\mathrm{EL}}(K) = \frac{Ze^2 m\gamma}{2\pi\hbar^2 4\pi\epsilon_0}\frac{1}{K^2+\kappa^2}, \qquad \kappa = \frac{1}{a_0 Z^{-1/3}}, \qquad K^2 = 2k_i^2(1-\cos\theta_{\mathrm{sc}}). \tag{1.114}$$

Then

$$\frac{\mathrm{d}\sigma_{EL}}{\mathrm{d}\Omega} = \gamma^2|f(K)^{\mathrm{EL}}|^2 \Longrightarrow \sigma^{\mathrm{EL}}_{\mathrm{TOT}} = 2\pi\gamma^2\int \mathrm{d}\Omega|f(K)^{\mathrm{EL}}|^2. \tag{1.115}$$

By substituting the numerical values, we obtain the (analytical) elastic cross section shown in Fig. 1.2.

Experimental measurements and semi–empirical parameterizations reported by Egerton [20] and Cowley [24] indicate total elastic cross sections for carbon of order 10^{-23} m^2 for incident electron energies in the range 100–300 keV, with a weak decrease as the beam energy increases. In the same interval, the present Born–approximation calculation yields $\sigma_{\mathrm{el}}(100\ \mathrm{keV}) \simeq 1.8 \times 10^{-23}\,\mathrm{m}^2$ and $\sigma_{\mathrm{el}}(300\ \mathrm{keV}) \simeq 9.1 \times 10^{-24}\,\mathrm{m}^2$, i.e. values in the range $(0.9\text{–}1.8) \times 10^{-23}\,\mathrm{m}^2$. Both the magnitude and the mild energy dependence are consistent with the experimental trends, indicating that the screened–Coulomb potential employed within the first Born approximation captures the dominant physics of elastic electron–carbon scattering under typical TEM conditions. In particular, the calculated cross sections lie in the range $(0.9\text{–}1.8) \times 10^{-23}\,\mathrm{m}^2$ for beam energies between 100 and 300 keV, fully consistent with the experimental estimates. Notably, both the absolute magnitude and the weak energy dependence observed in this interval are in agreement with available experimental measurements and semi–empirical parameterizations, which report only a modest decrease of the elastic cross section with increasing beam energy. This agreement indicates that, despite its simplicity, the screened–Coulomb potential employed within the first Born approximation captures the dominant physics governing elastic electron–carbon scattering under typical TEM conditions.

At sufficiently large incident wave vectors, $k_i \gtrsim 10\ \mathrm{nm}^{-1}$, the calculated elastic cross section exhibits an approximately $\sigma_{\mathrm{el}} \propto k_i^{-2}$ dependence. This behavior is expected and reflects the high–energy asymptotic limit of elastic electron–atom scattering within the first Born approximation for a screened Coulomb potential. Indeed, for relativistic electrons scattered by an atom with effective nuclear charge Z, the total elastic cross section is known to scale as

$$\sigma_{\mathrm{el}} \simeq 4\pi\,\gamma^2\,\frac{Z^{4/3}}{k_i^2},$$

as discussed by Egerton [20]. The present results are therefore fully consistent with the expected high–energy scaling behavior and confirm that the observed decrease of σ_{el} at large k_i is a physical effect rather than a numerical artifact.

Deviations at low scattering angles and at lower beam energies are expected, as the first Born approximation neglects multiple scattering, exchange effects, and short–range corrections to the screened Coulomb potential. More accurate treatments based on partial–wave expansions or relativistic Dirac–Hartree–Fock calculations are known to improve the agreement in these regimes, but do not alter the overall magnitude relevant for TEM applications.

1.7.2 Inelastic scattering (excitation): $e^- + C \to e^- + C^*$ $(1s \to 2p)$

It is important to emphasize that the present treatment refers to an isolated carbon atom and to a discrete atomic $1s \to 2p$ excitation; it should therefore not be directly associated with the experimental carbon K–edge observed in EELS of carbon–based materials.

We consider the calculation of the scattering amplitude for a core excitation process in carbon,

$$1s \to 2p.$$

Within the first Born approximation, and neglecting both spin and exchange effects as discussed earlier, the excitation scattering amplitude can be written as

$$f^{\text{exc}}(\mathbf{K}, m_\ell) = -\frac{m\gamma}{2\pi\hbar^2} \int \mathrm{d}^3\mathbf{r}_1 \int \mathrm{d}^3\mathbf{r}_2\, e^{\mathrm{i}\mathbf{K}\cdot\mathbf{r}_1}\, \Psi^*_{2p\,m_\ell}(\mathbf{r}_2)\, V(\mathbf{r}_1, \mathbf{r}_2)\, \Psi_{1s}(\mathbf{r}_2), \tag{1.116}$$

where $\mathbf{r}_1$ and $\mathbf{r}_2$ denote the coordinates of the incident electron and of the bound electron undergoing the excitation, respectively, and m_ℓ is the magnetic quantum number of the excited state.

The interaction potential $V(\mathbf{r}_1, \mathbf{r}_2)$ describes the repulsive electron–electron interaction and is modeled by a screened Coulomb (Yukawa–type) potential,

$$V(\mathbf{r}_1, \mathbf{r}_2) = \frac{e^2}{4\pi\epsilon_0|\mathbf{r}_1 - \mathbf{r}_2|}\, e^{-\lambda_{\text{sc}}|\mathbf{r}_1 - \mathbf{r}_2|}, \tag{1.117}$$

where λ_{sc} is the inverse screening length accounting for the average screening produced by the electrons that do not directly participate in the excitation process [20].

The carbon wave functions involved in the transition are taken in hydrogen–like form,

$$\begin{aligned} \Psi_{1s}(\mathbf{r}_2) &= \mathcal{N}_{1s}\, e^{-\xi_1 r_2/a_0}, \\ \Psi_{2p\,m_\ell}(\mathbf{r}_2) &= \mathcal{N}_{2p\,m_\ell}\, r_2\, e^{-\xi_2 r_2/a_0} Y_1^{m_\ell}(\theta_2, \varphi_2). \end{aligned} \tag{1.118}$$

where ξ_1 and ξ_2 are effective charge parameters. Following Clementi and Raimondi [34, 35], we use $\xi_1 = 5.6727$ for the $1s$ orbital and $\xi_2 = 1.5679$ for the $2p$ orbital.

The normalization constants are obtained from the condition $\int |\Psi|^2\, \mathrm{d}^3\mathbf{r}_2 = 1$, yielding

$$\begin{aligned} \mathcal{N}_{1s} &= \sqrt{\frac{\xi_1^3}{\pi a_0^3}}, \\ \mathcal{N}_{2p\,m_\ell} &= 2\sqrt{\frac{\xi_2^5}{3a_0^5}}. \end{aligned} \tag{1.119}$$

By inserting the wave functions (1.118) into Eq. (1.116), the excitation amplitude becomes explicit.

The screening parameter $\lambda_{\rm sc}$ provides an effective description of the reduction of the long–range electron–electron interaction due to the remaining bound electrons and regularizes the infrared divergence of the first–Born excitation cross section as $K \to 0$. Since this divergence is controlled by large $|\mathbf{r}_1 - \mathbf{r}_2|$, we set $\lambda_{\rm sc} = \xi_2/a_0$, i.e. we tie the screening length to the spatial extent of the final $2p$ orbital[9] .

At long range, the static Coulomb field generated by a single occupied orbital is indeed dominated by the monopole term, which is identical for the $1s$ and $2p$ states since both contain one electron. However, the infrared behavior of the first–Born *inelastic* amplitude is not determined by the static multipole expansion of either orbital, but by the spatial support of the *transition matrix element* $\langle 2p|V|1s\rangle$.

In particular, the divergence as $K \to 0$ arises from large values of $|\mathbf{r}_1 - \mathbf{r}_2|$, weighted by the overlap $\psi^*_{2p}(\mathbf{r})\psi_{1s}(\mathbf{r})$. Since the $2p$ orbital is significantly more extended than the $1s$ orbital, the long–range contribution to the excitation amplitude is effectively controlled by the spatial extent of the final state.

For this reason, the screening length entering the regularization of the infrared behavior is chosen to be of the order of the characteristic size of the $2p$ orbital,

$$\lambda_{\rm sc} = \frac{\xi_2}{a_0},$$

which provides a physically motivated cutoff for the infrared divergence of the excitation cross section within the first Born approximation. This interpretation is consistent with standard treatments of inelastic electron scattering, where the infrared behavior is governed by the spatial extent of the transition charge density

---

[9] A natural question is whether the screening length should instead be tied to the more localized $1s$ orbital, since the overlap $\Psi^*_{2p}(\mathbf{r})\Psi_{1s}(\mathbf{r})$ is confined by the core state. Here, however, $\lambda_{\rm sc}$ does not represent the spatial extent of the transition density, but rather an effective cutoff for the long–range projectile–electron interaction in Eq. (1.117). The infrared divergence as $K \to 0$ is driven by contributions from large separations $|\mathbf{r}_1 - \mathbf{r}_2|$, where the Coulomb kernel varies slowly. In this regime, the relevant screening is produced by the spectator electrons and is therefore controlled by the outer electronic cloud rather than by the tightly bound $1s$ core. For this reason, a screening length of the order of the spatial extent of the final $2p$ orbital, $\lambda_{\rm sc} = \xi_2/a_0$, provides a simple and physically motivated regularization within the present one–electron model.

rather than by the static charge distribution of the individual orbitals. In this framework, the effective screening length represents a phenomenological cutoff associated with the finite size of the electronic cloud participating in the excitation process [20, 29, 32]. We have verified that varying $\lambda_{\rm sc}$ by a factor of order unity only affects the detailed shape of the cross section in the extreme low–K regime, while leaving the overall magnitude and energy dependence of $\sigma_{\rm exc}$ essentially unchanged.

With this choice, the amplitude reads

$$f^{\rm exc}(\mathbf{K}, m_\ell) = -\frac{me^2\gamma}{4\pi^2\epsilon_0\hbar^2}\int \mathrm{d}^3\mathbf{r}_1 \int \mathrm{d}^3\mathbf{r}_2\, e^{\mathrm{i}\mathbf{K}\cdot\mathbf{r}_1}\sqrt{\frac{\xi_2^5}{3a_0^5}}\sqrt{\frac{\xi_1^3}{\pi a_0^3}}\, r_2\, e^{-(\xi_1+\xi_2)r_2/a_0} \\ \times Y_1^{*m_\ell}(\theta_2,\varphi_2)\frac{e^{-\xi_2|\mathbf{r}_1-\mathbf{r}_2|/a_0}}{|\mathbf{r}_1-\mathbf{r}_2|}. \qquad (1.120)$$

The integration over $\mathbf{r}_1$ yields

$$\frac{e^2}{4\pi\epsilon_0}\int \mathrm{d}^3\mathbf{r}_1 \frac{e^{-\xi_2|\mathbf{r}_1-\mathbf{r}_2|/a_0}}{|\mathbf{r}_1-\mathbf{r}_2|}e^{\mathrm{i}\mathbf{K}\cdot\mathbf{r}_1} = \frac{e^2}{\epsilon_0}\frac{e^{\mathrm{i}\mathbf{K}\cdot\mathbf{r}_2}}{K^2+(\xi_2/a_0)^2}, \qquad (1.121)$$

and the plane wave can be expanded as

$$e^{\mathrm{i}\mathbf{K}\cdot\mathbf{r}_2} = 4\pi\sum_{\ell',m'_\ell}\mathrm{i}^{\ell'}j_{\ell'}(Kr_2)Y_{\ell'}^{*m'_\ell}(\hat{\mathbf{K}})Y_{\ell'}^{m'_\ell}(\theta_2,\varphi_2). \qquad (1.122)$$

Here, $Y_{\ell'}^{m'_\ell}(\hat{\mathbf{K}})$ arises from the spherical–wave expansion of the plane wave $e^{\mathrm{i}\mathbf{K}\cdot\mathbf{r}_2}$ and encodes the angular dependence of the excitation with respect to the direction of the momentum transfer. The unit vector $\hat{\mathbf{K}} = \mathbf{K}/|\mathbf{K}|$ defines the preferred scattering direction, while the corresponding spherical harmonic determines how the excitation probability depends on the orientation of $\mathbf{K}$ relative to the atomic orbitals.

After angular integration, only the $\ell' = 1$ term survives, and one obtains

$$f^{\rm exc}(\mathbf{K}, m_\ell) = -\frac{32\pi\mathrm{i}\gamma}{a_0}\sqrt{\frac{\xi_2^5}{3a_0^5}}\sqrt{\frac{\xi_1^3}{\pi a_0^3}}\frac{Y_1^{*m_\ell}(\hat{\mathbf{K}})}{K^2+(\xi_2/a_0)^2}\int_0^\infty r_2^3 j_1(Kr_2)e^{-(\xi_1+\xi_2)r_2/a_0}\,\mathrm{d}r_2. \qquad (1.123)$$

Using

$$j_1(Kr_2) = \frac{\sin(Kr_2)}{K^2r_2^2} - \frac{\cos(Kr_2)}{Kr_2}, \qquad (1.124)$$

the radial integral can be evaluated analytically, leading to

$$f^{\rm exc}(\mathbf{K}, m_\ell) = -\frac{128\gamma\sqrt{\pi}\,\mathrm{i}\,\xi_2^{5/2}\xi_1^{3/2}(\xi_1+\xi_2)\,K\,Y_1^{*m_\ell}(\hat{\mathbf{K}})}{\sqrt{3}\,[K^2+(\xi_2/a_0)^2]\,[(\xi_1^2+\xi_2^2)^2+a_0^2K^2]^3}. \qquad (1.125)$$

The differential excitation cross section is then given by

$$\frac{\mathrm{d}\sigma_{\mathrm{exc}}}{\mathrm{d}\Omega} = \frac{k_f}{k_i}\,\gamma^2\,\left|f^{\mathrm{exc}}(K, m_\ell)\right|^2 . \tag{1.126}$$

Since the specific magnetic sublevel $m_\ell = 0, \pm 1$ of the excited electron is not resolved, we sum over all magnetic quantum numbers. Using the completeness relation for spherical harmonics with $\ell = 1$,

$$\sum_{m_\ell=-1}^{1} \left|Y_1^{m_\ell}(\hat{\mathbf{K}})\right|^2 = \frac{3}{4\pi}, \tag{1.127}$$

we finally obtain

$$\frac{\mathrm{d}\sigma_{\mathrm{exc}}}{\mathrm{d}\Omega} = \frac{k_f}{k_i}\,\gamma^2\,\frac{4096\,\xi_2^5\xi_1^3(\xi_1+\xi_2)^2K^2}{\left[K^2+(\xi_2/a_0)^2\right]^2\left[(\xi_1^2+\xi_2^2)^2+a_0^2K^2\right]^6}. \tag{1.128}$$

The total excitation cross section is analytically obtained by angular integration,

$$\sigma_{\mathrm{exc}} = \int \mathrm{d}\Omega\,\frac{\mathrm{d}\sigma_{\mathrm{exc}}}{\mathrm{d}\Omega}, \tag{1.129}$$

and is shown in Fig. 1.3.

Experimental EELS spectra of carbon do not exhibit any discrete $1s \to 2p$ excitation at higher energies. Instead, the carbon K–edge corresponds to the ionization threshold of the $1s$ core level, followed by transitions into continuum states with predominantly p–like character. It is important to clarify the origin of this discrepancy. Within the hydrogen–like approximation, the energy levels are expressed in terms of the effective charge parameter ξ_1 associated with the $1s$ core orbital,

$$E_n = -\xi_1^2\,\frac{13.6\ \mathrm{eV}}{n^2}. \tag{1.130}$$

The corresponding excitation energy reads

$$\Delta E_{1s\to 2p} = 13.6\ \mathrm{eV}\,\xi_1^2\left(1-\frac{1}{4}\right). \tag{1.131}$$

Using $\xi_1 \simeq 5.67$, one obtains

$$\Delta E_{1s\to 2p} \simeq \frac{3}{4}\times 13.6\times(5.67)^2 \simeq 4.29\times 10^2\ \mathrm{eV}, \tag{1.132}$$

in agreement with the threshold energy obtained in the present calculation.

This value, however, should not be interpreted as the physical position of the carbon K–edge. In real carbon, the $2s$ and $2p$ states form the valence manifold

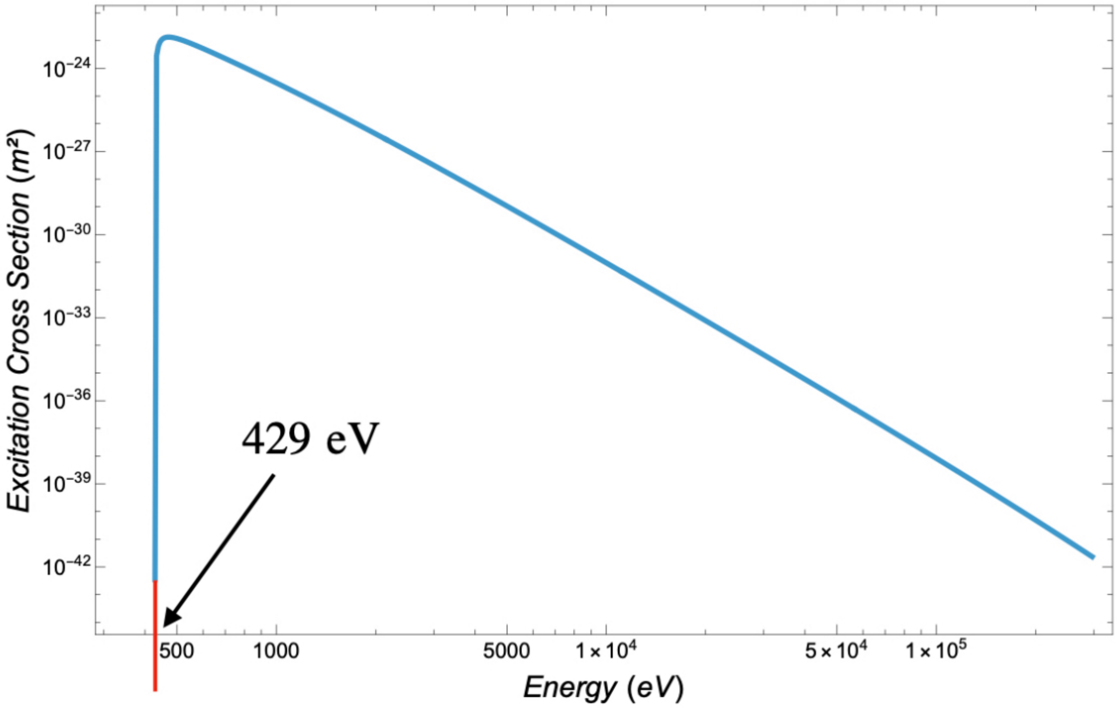

Figure 1.3: Total excitation cross section of the carbon atom as a function of the primary electron energy, calculated within the first Born approximation. The onset energy of the $1s \to 2p$ excitation is significantly higher than the experimentally observed carbon K–edge energy ($E_{\mathrm{K}} \simeq 284$ eV), reflecting the limitations of the simplified hydrogen–like model employed here.

and are already partially occupied, while core–loss excitations involve transitions from the $1s$ level to unoccupied continuum states. The experimentally observed K–edge at ~ 284 eV therefore corresponds to the ionization threshold of the $1s$ core state followed by excitation into continuum states with predominantly p–like angular character, as dictated by dipole selection rules (see fig. 1.4).

The hydrogen–like $1s \to 2p$ transition considered here thus represents a strongly simplified and non–realistic description of the final electronic states. Its role is to provide an analytically tractable framework for studying the angular dependence and momentum–transfer behavior of the excitation cross section within the first Born approximation, rather than to reproduce the absolute position of the carbon K–edge.

1.7.3 Inelastic scattering (ionization): $e^- + C \to +2e^- + C^+$

We consider the ionization process $1s \to$ continuum for the carbon atom. The calculation closely follows the one previously performed for hydrogen, with the bound

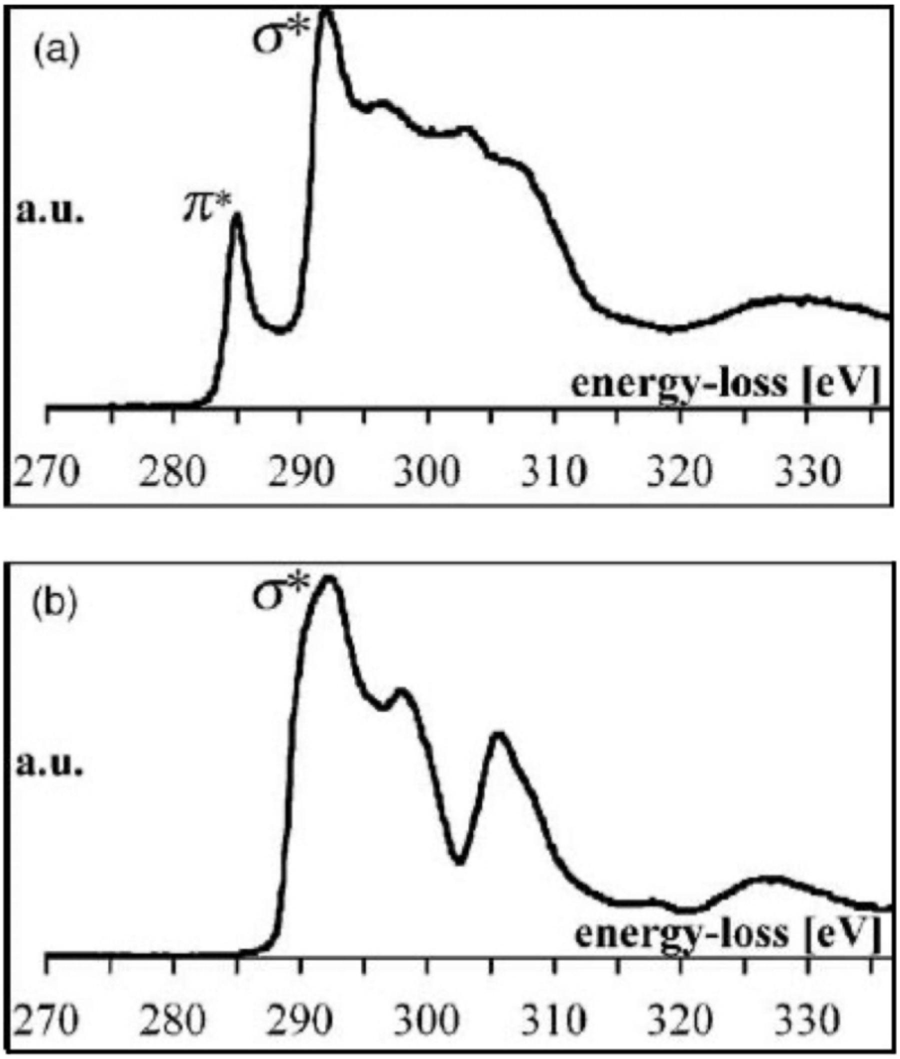

Figure 1.4: Representative carbon K-edge ELNES (Electron Energy-Loss Near-Edge Structure) spectra illustrating the sensitivity of EELS to the local bonding configuration. The pronounced π^* resonance at $\sim$284 eV is characteristic of sp^2-hybridized carbon, while the dominance of the σ^* manifold at higher energy losses reflects sp^3 bonding. Adapted from Hamon *et al.* [36].

initial state described by an effective hydrogen–like orbital.

The initial bound state of the carbon atom is taken as

$$\Psi_C^{in}(r_2) = \sqrt{\frac{\xi_1^3}{\pi a_0^3}}\, e^{-\xi_1 r_2/a_0}, \tag{1.133}$$

where ξ_1 is the effective nuclear charge parameter introduced in Section 1.7.2.

Within the first Born approximation, the ionization amplitude reads

$$f_{ion}(\mathbf{K}, \mathbf{k}_s) = -\frac{m\gamma}{2\pi\hbar^2} \int \mathrm{d}^3\mathbf{r}_1 \int \mathrm{d}^3\mathbf{r}_2\, e^{-\mathrm{i}\mathbf{K}\cdot\mathbf{r}_1} \Psi_C^{*fin}(\mathbf{r}_2) \frac{e^2}{4\pi\epsilon_0 |\mathbf{r}_1 - \mathbf{r}_2|} \Psi_C^{in}(\mathbf{r}_2). \tag{1.134}$$

and

$$\Psi_C^{fin}(r_2) = \frac{e^{\mathrm{i}\mathbf{k}_s\cdot\mathbf{r}_2}}{L^{3/2}}\, e^{\pi/(2a_0k_s)}\, \Gamma\left(1+\frac{\mathrm{i}}{a_0k_s}\right)\, {}_1F_1\left(-\frac{\mathrm{i}}{a_0k_s}; 1; -\mathrm{i}(k_sr_2+\mathbf{k}_s\cdot\mathbf{r}_2)\right) , \tag{1.135}$$

namely, the same given in eq. (1.101).

This is due to the fact that in the calculation of the total ionization cross section of carbon, the wave function of the ejected electron was modeled using a Coulomb wave function formally equivalent to that employed in the hydrogen case. This approximation is justified by the fact that, once the electron is ionized and sufficiently far from the parent atom, it effectively experiences a Coulomb potential corresponding to a unit positive charge, similarly to an electron escaping from a hydrogen atom. Consequently, the asymptotic form of the continuum wave function can be reasonably described by the hydrogenic Coulomb solution.

The calculation made by hydrogen remains valid and is the just given in the appendix A, with the only difference made by $\Psi_C^{fin}(r_2)$ which contains ξ_1.[10].

Figure 1.5 shows the total ionization cross section as a function of the ejected electron momentum for the excitation process considered here.

---

[10] This implies that in eq. (A.13) we have to replace $\lambda = \xi_1/a_0$, instead of $\lambda = 1/a_0$, while all other aspects remain unchanged.

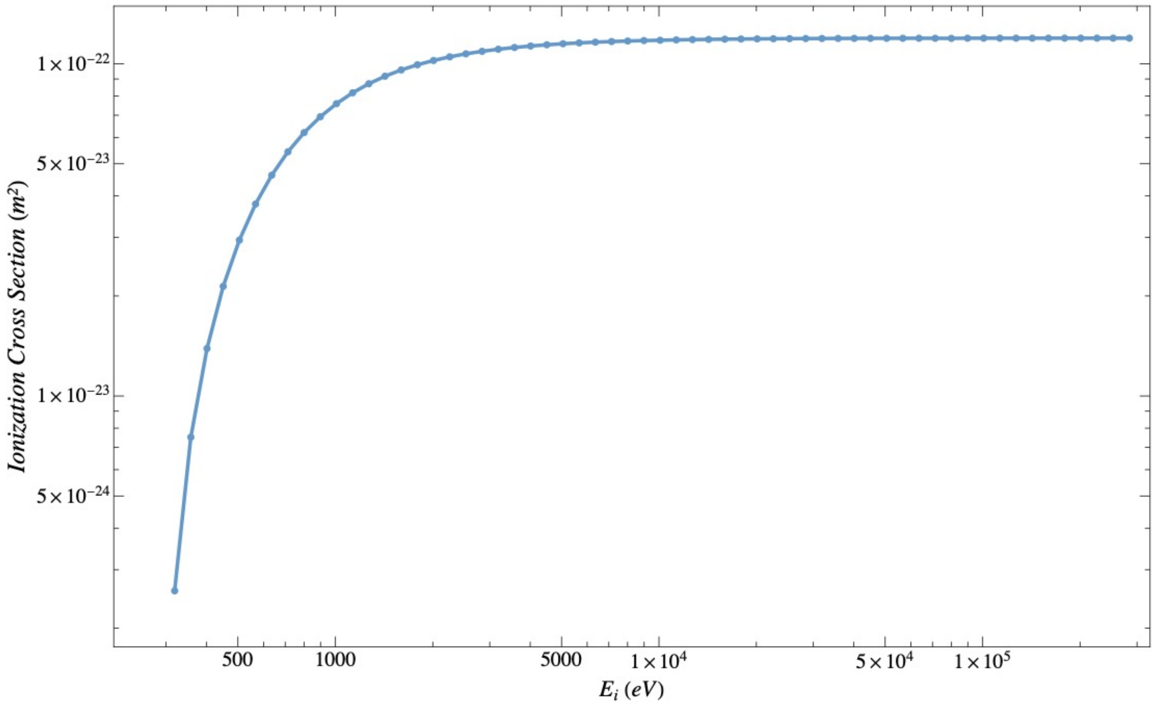

Figure 1.5: Total ionization cross section of the carbon atom as a function of the primary electron energy, E_i, calculated within the first Born approximation. The plateau at high energies is an artifact of the simplified one–electron model and is discussed in the main text. Discrete symbols represent the calculated values of the ionization cross section; the solid line is obtained by joining the points and is shown as a guide to the eye.

As can be seen in Fig. 1.5, the calculated total ionization cross section exhibits a plateau at large values of the primary electron energy E_i. This behavior is in qualitative contrast with experimental data and more refined theoretical calculations reported in the literature, such as the DWBA results and measurements shown in Fig. 1.6 [37], where the ionization cross section decreases monotonically with increasing incident electron energy.

Although the two figures are plotted as a function of different kinematic variables, both describe the high–energy behavior of the ionization cross section and are therefore directly comparable at a qualitative level.

This unphysical behavior originates from the lack of orthogonality between the initial bound state and the final continuum state adopted in the present model. While in hydrogen bound and continuum eigenstates of the same Hamiltonian form a complete and orthogonal set, here the initial state is described by a hydrogen–like orbital with an effective nuclear charge, whereas the final state is a Coulomb

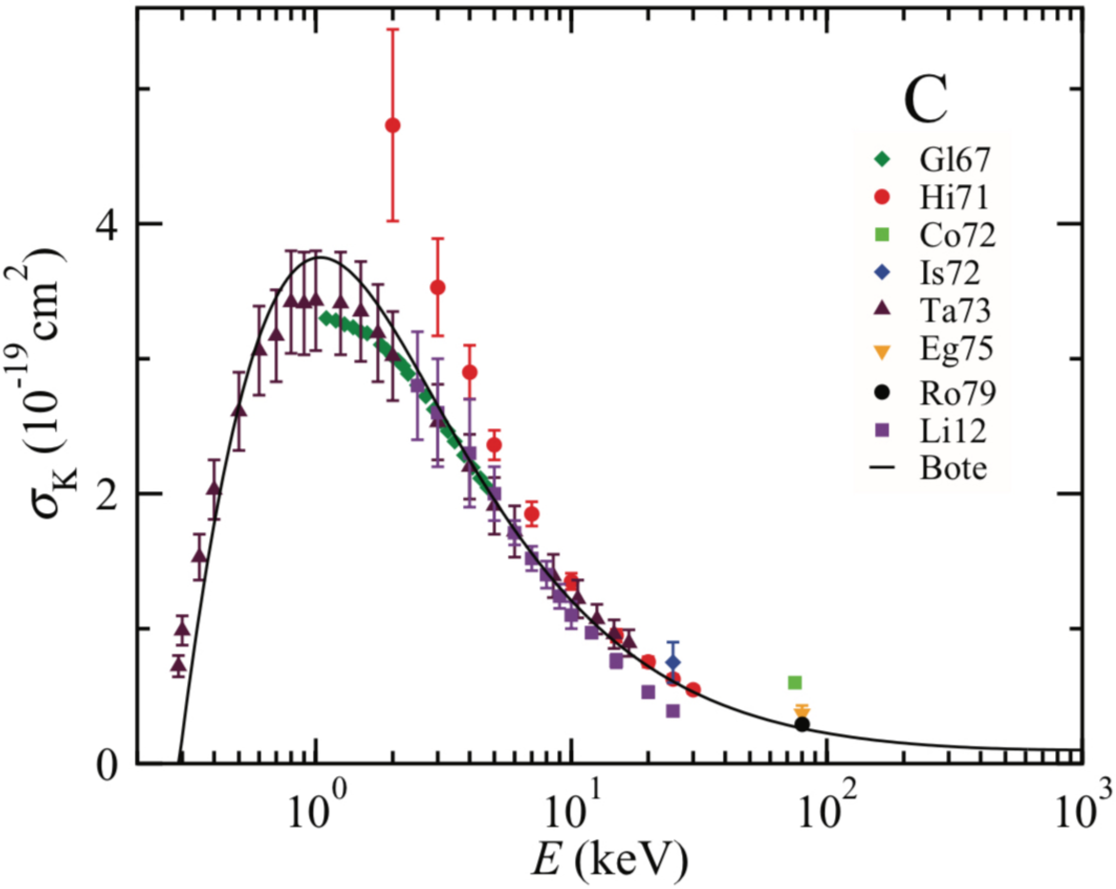

Figure 1.6: Absolute K-shell ionization cross sections vs. incident electron energy for Carbon, C. Solid curves are the results of the DWBA calculations. The symbols show measured cross sections, with the legend indicating the key references identified in Table 2 of the article [37].

continuum eigenfunction of a different Hamiltonian.[11]

The resulting residual overlap generates a spurious background contribution to the ionization amplitude, which persists even at high incident energies and manifests itself as a plateau in the total ionization cross section. This feature should therefore be regarded as a modeling artifact rather than a physical saturation of the ionization process.

It is fundamental to underline that while the present work adopts an analytical

---

[11] A possible remedy within effective one–electron models is to enforce orthogonality by explicitly projecting out the bound component from the continuum wavefunction. One may define an orthogonalized continuum state as $\widetilde{\Psi}_C^{fin}(\mathbf{r}) = \Psi_C^{fin}(\mathbf{r}) - \langle \Psi_C^{in} | \Psi_C^{fin} \rangle \, \Psi_C^{in}(\mathbf{r})$. In principle, this procedure removes the residual overlap responsible for the spurious high–energy background and restores a monotonically decreasing behavior of the ionization cross section.

approach based on the first Born approximation, alternative formulations relying on first-principles electronic-structure calculations have been developed to describe inelastic electron scattering and energy-loss processes [38].

In particular, momentum-resolved descriptions of EELS provide a complementary framework that directly links scattering probabilities to the electronic structure of the target [39, 40, 41].

More generally, the theoretical foundations of electron energy-loss processes are rooted in the dielectric response of condensed matter and in the interaction of fast electrons with collective and single-particle excitations [29, 31, 42, 43, 44].

1.7.4 Normalization Constants and Probability Conservation

In the previous sections, we derived the asymptotic form of the Lippmann–Schwinger equation in the first Born approximation, Eq. (1.41). When both elastic and inelastic channels are open, the total wavefunction in the far field can be formally written, at the level of scattering amplitudes, as

$$\psi(\mathbf{r}) \underset{r\to\infty}{=} \underbrace{\varphi_i(\mathbf{r})}_{\substack{\text{incident}\\ \text{wave}}} + \underbrace{\psi_{\text{el}}(\mathbf{r})}_{\substack{\text{elastic}\\ \text{scattered}\\ \text{wave}}} + \underbrace{\psi_{\text{in}}(\mathbf{r})}_{\substack{\text{inelastic}\\ \text{scattered}\\ \text{wave}}} \simeq \frac{1}{L^{3/2}}\left[e^{\mathrm{i}\mathbf{k}_i\cdot\mathbf{r}} + \frac{e^{\mathrm{i}k_i r}}{r} f^{(\mathrm{EL})}(K) + \frac{e^{\mathrm{i}k_f r}}{r} f^{(\mathrm{IN})}(K, k_s)\right]. \tag{1.136}$$

Equation (1.136) is written under the assumption that only a single inelastic channel is open, corresponding to a specific final state of the target. This situation applies to the case considered in the present work but, in the general case, several inelastic channels may be energetically allowed, in which case the asymptotic wavefunction takes the form

$$\psi(\mathbf{r}) \underset{r\to\infty}{=} \frac{1}{L^{3/2}}\left[e^{\mathrm{i}\mathbf{k}_i\cdot\mathbf{r}} + \frac{e^{\mathrm{i}k_i r}}{r} f^{(\mathrm{EL})}(K) + \sum_n \frac{e^{\mathrm{i}k_{f,n} r}}{r} f_n^{(\mathrm{IN})}(K, k_{s,n})\right], \tag{1.137}$$

where the sum runs over all energetically accessible inelastic final states of the target.

This representation clearly separates the incident, elastic, and inelastic contributions in the asymptotic region, far from the scattering center.

However, Eq. (1.136) should be regarded as a formal asymptotic expansion at the level of coherent scattering amplitudes. In this representation, the incident and elastically scattered components share the same energy and, in principle, interfere, particularly in the forward direction, while the inelastic component corresponds to an outgoing state with different energy and does not interfere with them.

In the present work, however, we are not interested in coherent phase-sensitive interference effects between different outgoing components, but rather in the redistribution of probability flux among experimentally distinguishable outcomes. We therefore adopt an effective description at the level of intensities, appropriate for a collimated electron beam undergoing single scattering in a thin specimen, as commonly assumed in TEM and STEM experiments. Within this framework, transmission without scattering, elastic scattering, and inelastic scattering are treated as mutually exclusive detection channels, and cross-channel coherence effects are neglected in the far field.

To illustrate this point, consider a collimated electron beam propagating in free space, $V = 0$, described by a normalized plane wave.

When a scattering potential $V \neq 0$ is present, the incoming flux is divided between three mutually exclusive outcomes: transmission without scattering, elastic scattering (with energy conservation) and inelastic scattering (with energy loss due to excitation or ionization of the target).

In the asymptotic region, elastic and inelastic scattering channels are associated with outgoing waves characterized by different energies and momenta and therefore do not interfere. Although the incident and elastically scattered waves are, in principle, coherent, in typical TEM/STEM measurements the detector is not phase-sensitive and records only intensities. Within this effective incoherent-channel description, probability conservation can be expressed at the level of channel-resolved fluxes as

$$|\psi(\mathbf{r})|^2 \simeq |\varphi_i(\mathbf{r})|^2 + |\psi_{\mathrm{el}}(\mathbf{r})|^2 + |\psi_{\mathrm{in}}(\mathbf{r})|^2. \tag{1.138}$$

At this point, it is important to stress that the following normalization should not be interpreted as a modification of the exact asymptotic solution of the Lippmann–Schwinger equation at the level of coherent amplitudes. Rather, it provides an effective and physically transparent description of probability redistribution appropriate for a collimated electron beam undergoing single scattering in a thin target, as commonly encountered in TEM and STEM. Within this interpretation, elastic and inelastic channels are treated as mutually exclusive outcomes, and interference effects between channels of different energy are neglected in the far field.

A correct asymptotic description of the scattering process must therefore include normalization coefficients accounting for the redistribution of probability among the different channels:

$$\psi(\mathbf{r}) \underset{r\to\infty}{=} \frac{1}{L^{3/2}} \left[C\, e^{\mathrm{i}\mathbf{k}_i\cdot\mathbf{r}} + D\, \frac{e^{\mathrm{i}k_i r}}{r}\, f^{(\mathrm{EL})}(K) + E\, \frac{e^{\mathrm{i}k_f r}}{r}\, f^{(\mathrm{IN})}(K, k_s) \right]. \tag{1.139}$$

Here $C \neq 1$, reflecting the depletion of the forward-transmitted amplitude due to scattering. Global probability conservation imposes the constraint

$$|C|^2 + |D|^2 + |E|^2 = 1, \tag{1.140}$$

which holds within the effective incoherent-channel description adopted here.

A physically transparent determination of the coefficients C, D, and E can be obtained by matching microscopic scattering probabilities to the macroscopic flux of the beam.

In the present derivation we consider a *single* scattering center (an isolated atom), so that the illuminated region contains $N = 1$ target. In this case the probability of a scattering event is $\sigma_{\mathrm{tot}}/(\pi R^2)$ and vanishes as $R \to \infty$, as expected for a single atom embedded in an increasingly large beam area. For an extended specimen containing N independent scattering centers within the illuminated region, the factors below generalize by replacing $\sigma_{\mathrm{tot}} \to N\sigma_{\mathrm{tot}}$ (and similarly for σ_{el} and σ_{in}) in the dilute single-scattering regime $N\sigma_{\mathrm{tot}} \ll \pi R^2$.

Let a collimated electron beam of radius R impinge on a target characterized by a total microscopic scattering cross section σ_{tot},

$$\sigma_{\mathrm{tot}} = \sigma_{\mathrm{el}} + \sigma_{\mathrm{in}} = \sigma_{\mathrm{el}} + \sigma_{\mathrm{exc}} + \sigma_{\mathrm{ion}}. \tag{1.141}$$

The incident flux is uniformly distributed over the geometrical area πR^2, so the probability for a given electron to undergo no scattering event is

$$P_{\text{no scatt.}} = 1 - \frac{\sigma_{\mathrm{tot}}}{\pi R^2}. \tag{1.142}$$

Similarly, the probabilities for elastic and inelastic scattering events are given by $\sigma_{\mathrm{el}}/(\pi R^2)$ and $\sigma_{\mathrm{in}}/(\pi R^2)$, respectively. The normalization coefficients in Eq. (1.139) can therefore be chosen as

$$C = \sqrt{1 - \frac{\sigma_{\text{tot}}}{\pi R^2}}, \tag{1.143}$$

$$D = \sqrt{\frac{\sigma_{\text{el}}}{\pi R^2}}, \tag{1.144}$$

$$E = \sqrt{\frac{\sigma_{\text{in}}}{\pi R^2}}. \tag{1.145}$$

By construction, these coefficients satisfy the flux-conservation condition (1.140).

Equation (1.139) thus provides a self-consistent normalization scheme linking microscopic scattering amplitudes $f^{(\text{EL})}$ and $f^{(\text{IN})}$ to macroscopic beam attenuation and the redistribution of probability flux. This connection is particularly relevant in electron microscopy, where experimentally accessible observables such as transmitted, elastically scattered, and inelastically scattered intensities must be consistently related to scattering cross sections computed from first principles.

From a conceptual standpoint, this normalization embodies the physical content of the optical theorem and the unitarity of the $\mathcal{S}$-matrix: any reduction of the forward-transmitted amplitude is exactly compensated by the total scattered flux, and the sum over all mutually exclusive channels exhausts the incoming probability [13, 19]. In the following, this framework will be used to derive quantitative expressions for contrast, attenuation, and energy-loss signals in realistic TEM and STEM geometries.

1.7.5 Scattering Between the Primary Beam and the Sample

Let σ_{atom} denote the total (elastic or inelastic) cross section for a single isolated atom at the beam energy under consideration. For a homogeneous material of mass density ρ [$\text{kg}\,\text{m}^{-3}$] and molar mass M [$\text{kg}\,\text{mol}^{-1}$], the atomic number density is

$$n_{\text{at}} = \frac{\rho\, N_{\text{A}}}{M} \qquad [\text{m}^{-3}],$$

where N_{A} is the Avogadro constant. The corresponding macroscopic cross section, or attenuation coefficient, is

$$\Sigma = n_{\text{at}}\, \sigma_{\text{atom}} \qquad [\text{m}^{-1}].$$

In the single-scattering regime (thin-sample), $\Sigma t \ll 1$, the probability of undergoing at least one scattering event in a thickness t is approximately

$$P_{\geq 1}(t) \simeq \Sigma\, t,$$

while in general

$$P_{\geq 1}(t) = 1 - e^{-\Sigma t}.$$

The mean free path of the electron beam is thus given by

$$\lambda_{\mathrm{MFP}} = \frac{1}{\Sigma}.$$

To illustrate, consider a simple specimen composed of hydrogen atoms in their ground state.

The first incident electron e_{p} may undergo elastic scattering, $e_{\mathrm{p}} + \mathrm{H} \to e_{\mathrm{p}} + \mathrm{H}$, or inelastic scattering such as excitation or ionization. In the ionization event, a secondary electron e_{s} is emitted, and a proton p^+ remains. Secondary electrons contribute to a growing density of free-electrons $n_e(\mathbf{r})$ within the sample.

A subsequent primary electron will then interact with a slightly modified potential landscape: one of the neutral atoms has become an ion p^+ embedded in, and weakly screened by, the nascent electron gas $n_e(\mathbf{r})$.

Once ionization has occurred, the scattering potential experienced by a subsequent primary electron is dominated by the screened Coulomb attraction of the residual positive ion.

A convenient model for this effective interaction is a Yukawa (screened Coulomb) potential,

$$V(r) = -\frac{e^2}{4\pi\varepsilon_0} \frac{e^{-r/\lambda_{\mathrm{TF}}}}{r},$$

where λ_{TF} is the screening length determined by the surrounding electronic environment. In a classical plasma, λ corresponds to the Debye length,

$$\lambda_{\mathrm{D}} = \sqrt{\frac{\varepsilon_0 k_{\mathrm{B}} T_e}{n_e e^2}},$$

where T_e is the electron temperature and n_e is the electron number density. For a degenerate electron gas, the appropriate scale is the Thomas–Fermi screening length, $\lambda_{\mathrm{TF}} = 1/k_{\mathrm{TF}}$, where

$$k_{\mathrm{TF}}^2 = \frac{3 n_e e^2}{2\varepsilon_0 E_{\mathrm{F}}}, \qquad E_{\mathrm{F}} = \frac{\hbar^2}{2m}(3\pi^2 n_e)^{2/3}.$$

Here, n_e denotes the number density of free electrons.

In the following, the screening length is identified with the Thomas–Fermi screening length, $\lambda = \lambda_{\mathrm{TF}}$, so that, within the first Born approximation, the elastic scattering amplitude for the Yukawa potential is

$$f(\mathbf{K}) = -\frac{m\gamma}{2\pi\hbar^2}\int \mathrm{d}^3\mathbf{r}\, e^{i\mathbf{K}\cdot\mathbf{r}} V(r) = \frac{me^2}{2\pi\varepsilon_0\hbar^2}\frac{1}{K^2 + 1/\lambda_{TF}^2} = \frac{2}{a_0}\frac{1}{K^2 + 1/\lambda_{TF}^2},$$

where $\mathbf{K} = \mathbf{k}_i - \mathbf{k}_f$ is the momentum transfer and $a_0 = 4\pi\varepsilon_0\hbar^2/(me^2)$ is the Bohr radius. For dilute electron densities, one typically finds $\lambda_{TF} \gtrsim a_0$, corresponding to a weak (long-range) screening of the Coulomb potential, but the exact value of λ_{TF} follows self-consistently from n_e through the relations above [20, 42, 43].

As the irradiation proceeds, the number density of free electrons n_e increases cumulatively with the dose, and the screening length λ_{TF} decreases correspondingly. For typical TEM conditions, even modest ionization fractions can locally lead to screening lengths comparable to atomic scales.

To see when λ_{TF} can reach atomic length scales, it is sufficient to perform an order-of-magnitude estimate. Let n_{at} be the atomic number density of the solid and let $f_{\mathrm{ion}} \ll 1$ be the local fraction of electrons that are promoted to quasi-free (or weakly bound) states by irradiation. Then the free-electron density can be written as

$$n_e \simeq f_{\mathrm{ion}}\, n_{\mathrm{at}}. \tag{1.146}$$

For a condensed-matter target, n_{at} is typically of the order $10^{29}\,\mathrm{m}^{-3}$, so that even a very small ionization fraction, $f_{\mathrm{ion}} \sim 10^{-4}$–$10^{-3}$, corresponds to

$$n_e \sim 10^{25}\text{–}10^{26}\,\mathrm{m}^{-3}. \tag{1.147}$$

Using the Thomas–Fermi relations above, these densities yield screening lengths of a few Bohr radii, e.g.

$$n_e = 10^{25}\,\mathrm{m}^{-3} \;\Rightarrow\; \lambda_{\mathrm{TF}} \approx 4.7\,a_0, \qquad n_e = 10^{26}\,\mathrm{m}^{-3} \;\Rightarrow\; \lambda_{\mathrm{TF}} \approx 3.2\,a_0, \tag{1.148}$$

demonstrating that atomic-scale screening can arise locally once a small population of quasi-free electrons builds up. This argument is intended as an effective, local estimate: the actual charge density experienced by subsequent electrons depends on transport, trapping and recombination, which are treated at the continuum level in

Chapter 4. It should also be noted that electronically excited and ionized states are not permanent, but relax via a cascade of de-excitation processes (Auger decay, radiative recombination, and charge transport), which tend to partially refill core holes and reduce the local free-electron density. The competition between excitation/ionization and relaxation processes, and their respective time scales, will be explicitly addressed in the following sections within the continuous transport framework.

At this point, the effective interaction potential experienced by subsequent primary electrons differs substantially from the bare Coulomb potential of a neutral atom.

This progressive modification implies that the elastic and inelastic scattering cross sections are no longer fixed quantities, but become functions of the local electronic environment and, ultimately, of the accumulated electron dose.

After sufficiently many irradiation steps, the sample can no longer be described as an ensemble of independent scattering centers, but rather as a dynamically evolving medium in which ionization, screening, and charge transport are intrinsically coupled.

The present discussion thus provides the microscopic motivation for the effective-medium approach introduced in chapter 4, where the cumulative effect of successive beam electrons is described through coupled transport equations for the electron and ion densities. In that framework, the screening length λ, the effective potential, and the resulting scattering probabilities emerge self-consistently from the evolving charge distribution, allowing the transition from a single-event description to a dose-dependent model of beam–matter interaction.

It is important to stress that the purpose of the above analysis is not to provide a step-by-step scattering theory for each successive primary electron, but rather to clarify the physical mechanism by which the target is progressively modified by irradiation. While the first beam electrons may be reasonably described in terms of single-atom scattering processes, this picture rapidly loses validity as ionization accumulates and the local electronic environment evolves. At that stage, an explicit event-by-event treatment based on isolated-atom cross sections and Born-type calculations becomes neither practical nor physically meaningful. Instead, the focus must shift to the description of how the sample itself evolves under sustained electron irradiation, which is the approach adopted in the following section.

The probabilistic interpretation of elastic, excitation, and ionization cross sections discussed in the previous subsection provides a convenient framework for connecting single-event scattering physics to the cumulative modification of the sample under irradiation. In the following, this perspective is naturally extended to a local, position-dependent formulation appropriate for continuous beam profiles.

1.7.6 Local formulation and connection to continuous models

In realistic TEM and STEM configurations, the electron flux is generally non-uniform and confined to a limited region of the sample. While the relative fractions f_i remain determined solely by the microscopic cross sections, the absolute number of events becomes position-dependent through the local electron flux $\Phi(\mathbf{r})$.

This observation provides a natural bridge between the discrete, microscopic description of electron–atom scattering and the continuous, macroscopic models employed in the following chapters. In particular, the ionization cross section σ_{ion} enters directly into the definition of a local generation rate of free electrons,

$$G(\mathbf{r}) = \sigma_{\text{ion}}\, \Phi(\mathbf{r})\, n_{\text{H}}(\mathbf{r}), \tag{1.149}$$

which forms the basis for the drift–diffusion–recombination framework used to describe beam-induced plasma formation inside the sample.

Here $G(\mathbf{r})$ represents the local volumetric generation rate of free electrons, i.e. the number of electrons created per unit time and per unit volume by ionization events at position $\mathbf{r}$. It is directly proportional to the local electron flux $\Phi(\mathbf{r})$ and to the density of target atoms $n_{\text{H}}(\mathbf{r})$, and therefore provides the microscopic source term entering the macroscopic transport equations. In the continuous description, $G(\mathbf{r})$ acts as the link between the single-event scattering cross section σ_{ion} and the time-dependent evolution of the electron density.

In this sense, the probabilistic interpretation of scattering cross sections presented here establishes the conceptual link between microscopic interaction physics and the macroscopic transport equations developed in the remainder of this work.

Chapter 2

Elastic Scattering: Plane-Wave vs. Spherical-Wave Illumination

In electron scattering theory, the standard formulation assumes an incident plane wave interacting with a spherically symmetric potential centered at the origin, as schematically illustrated in Fig. 2.1. Within this framework, the incident beam is translationally invariant and the scattering problem admits a high degree of symmetry.

This approximation is mathematically convenient and historically motivated by early developments in transmission electron microscopy (TEM), where the incident beam is highly collimated and the wavefront can be accurately regarded as planar over the spatial extent of the scattering region.

In modern electron microscopy, however, the incident illumination is often *not* well described by a plane wave. In particular, in scanning transmission electron microscopy (STEM), the beam is intentionally focused to form a spatially localized probe, and the incident wavefield at the specimen is characterized by a finite angular spread and a nontrivial phase profile. As a result, translational invariance is lost and the scattering process becomes explicitly sensitive to the spatial structure and curvature of the incoming wavefront.

In practical STEM simulations, the scattering of displaced or focused probes is routinely treated within the multislice formalism [21], which provides a numerically accurate solution of the paraxial wave equation for arbitrary illumination functions and complex specimens. Within this framework, the effects of probe displacement, finite convergence angle, aberrations, and multiple scattering are naturally included through the propagation of the electron wavefunction across successive slices of the

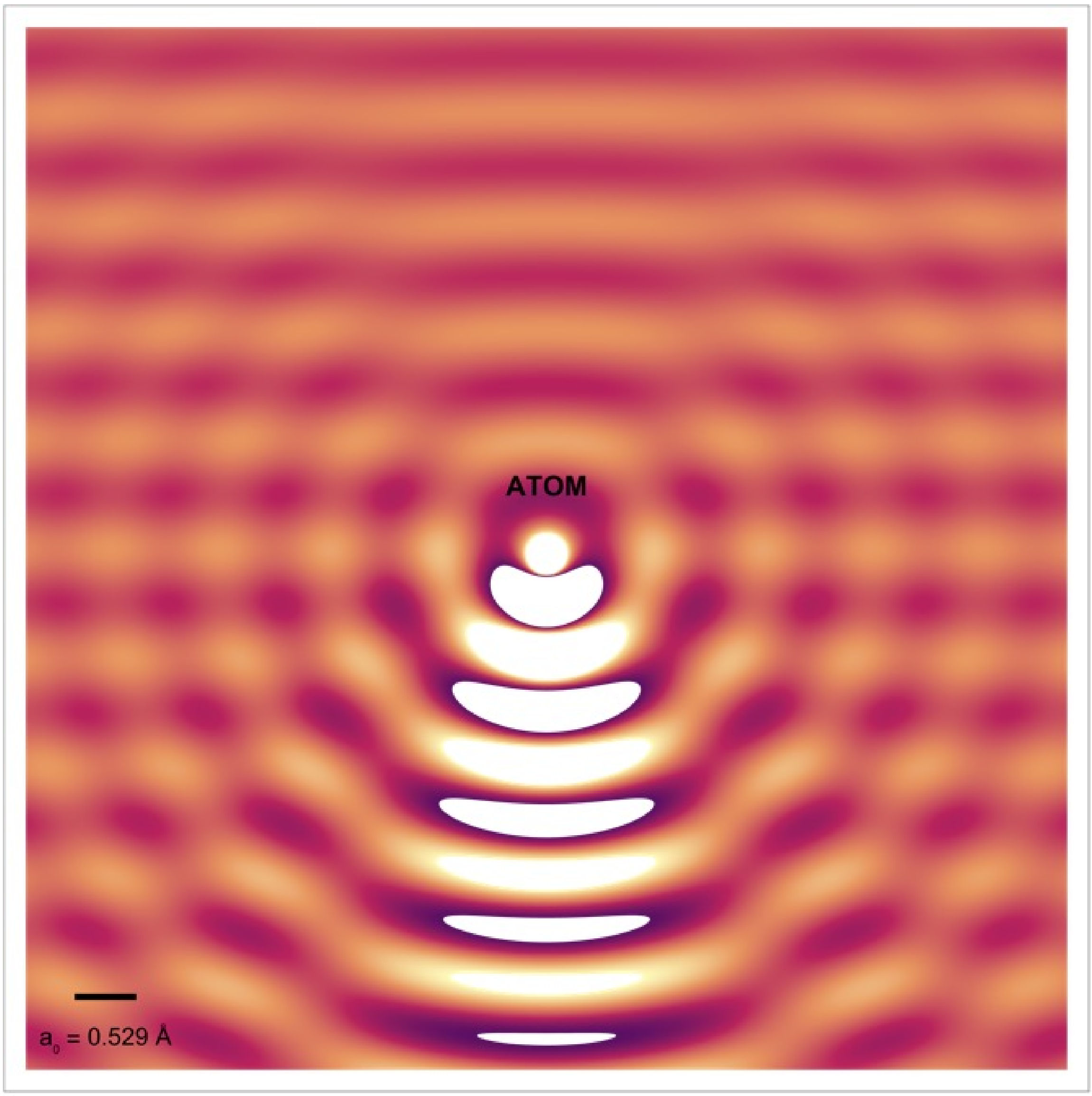

Figure 2.1: Qualitative visualization of elastic electron scattering from a single atom. The figure shows the real part of the total electron wavefunction $\Re[\Psi_\mathrm{f}(x,y)]$, obtained as the superposition of an incident plane wave propagating along the negative y direction and an outgoing spherical wave scattered by an atom located at the origin. The scattered contribution is weighted by an angle–dependent scattering amplitude $f(K)$, where the momentum transfer is $K = 2k_i \sin(\theta/2)$ and θ is the scattering angle with respect to the incident beam direction. The resulting interference pattern illustrates the wave–optical nature of electron–atom scattering and is intended as a qualitative representation rather than a quantitative observable.

sample.

However, the multislice approach is intrinsically numerical and offers limited analytical insight into the role of wavefront curvature, symmetry breaking, and angular-momentum channel activation. The simplified spherical-wave model adopted here should therefore be regarded as a complementary theoretical framework, aimed at isolating and interpreting the fundamental physical mechanisms underlying finite-distance and off-axis illumination effects, which are otherwise embedded in full multislice simulations.

From a theoretical standpoint, one convenient way to capture such effects is to replace the incident plane wave by an illumination with finite curvature, modeled here as a spherical wave associated with a source located at a finite position $\mathbf{r}_s$ relative to the scattering center. This *spherical-wave illumination* explicitly breaks translational symmetry and introduces spatially varying phases across the interaction region. It should be regarded as an idealized reference model, rather than as a complete description of a realistic STEM probe.

The finite distance and possible lateral displacement of the source remove the symmetries inherent to the plane-wave description and, in general, lead to the activation of additional angular-momentum channels in the scattering amplitude. In particular, when the illumination is not aligned with the symmetry axis of the target, partial-wave components with magnetic quantum number $m \neq 0$ contribute, whereas for an on-axis plane wave only a restricted subset of angular-momentum channels is allowed.

Such symmetry-breaking effects are especially relevant for electron energy-loss spectroscopy (EELS) and related momentum-resolved techniques, where off-axis or phase-structured illumination is routinely employed to enhance contrast, probe anisotropic excitations, or selectively access multipole-allowed transitions. In these configurations, the angular structure of the scattered signal depends not only on the intrinsic electronic properties of the target, but also on the geometry and phase distribution of the incident wavefront.

Recent advances in aberration correction, vortex-beam generation, and wavefront engineering have further emphasized the role of the incident illumination as a controllable degree of freedom. Through appropriate shaping of the phase and angular spectrum of the beam, it is possible to tailor the spatial localization of the interaction and to enhance or suppress specific symmetry channels in the scattering response. While these effects are most naturally described in terms of aperture functions and aberration phases, they can be qualitatively explored using simplified models that explicitly encode finite wavefront curvature.

In this chapter, we therefore develop a theoretical framework for *elastic* scattering from a hydrogen-like potential illuminated by a spherical wave associated with a displaced source. Within the first Born approximation, we derive a generalized expression for the scattering amplitude that explicitly depends on the source position $\mathbf{r}_s$. This formulation allows us to quantify how finite-distance illumination and lateral displacement modify the angular distribution of the scattered intensity.

Two representative geometrical configurations are considered: (i) an on-axis illumination, $\mathbf{r}_s = (0, 0, z_s)$, which preserves axial symmetry, and (ii) an off-axis illumination, $\mathbf{r}_s = (x_s, 0, z_s)$, which explicitly breaks azimuthal symmetry. These cases provide clear insight into the role of symmetry breaking and the activation of non-zero m components in the scattering amplitude.

The results presented in this chapter should be interpreted as a systematic study of finite-distance and spherical-wave illumination effects within a controlled theoretical model. They do not imply a one-to-one identification between a spherical incident wave and a realistic STEM probe. In particular, while a paraxial STEM probe with vanishing spherical aberration ($C_s = 0$) may locally reproduce the quadratic phase structure of a spherical wave at the specimen plane, this correspondence generally breaks down in the presence of aberrations ($C_s \neq 0$), where higher-order phase terms cannot be captured by a simple spherical-wave description.

The present framework therefore provides a physically transparent reference against which more complete descriptions of probe formation and aberration effects can be compared, and offers a natural starting point for future extensions to coherent imaging, localized spectroscopy, and wavefront-controlled scattering phenomena.

2.1 Theoretical Background: Scattering with spherical Illumination

In Chapter 1, the elastic scattering amplitude for an incident plane wave was defined as[1]

$$f(\mathbf{K}) = -\frac{m}{2\pi\hbar^2}\int \mathrm{d}^3\mathbf{r'}\, e^{\mathrm{i}\mathbf{K}\cdot\mathbf{r}'} V(\mathbf{r}'), \tag{2.1}$$

which, for a spherically symmetric potential, reduces to

$$f(K) = -\frac{m}{2\pi\hbar^2}\int \mathrm{d}^3\mathbf{r'}\, e^{\mathrm{i}\mathbf{K}\cdot\mathbf{r}'} V(r'). \tag{2.2}$$

The corresponding differential cross section is given by

$$\frac{\mathrm{d}\sigma}{\mathrm{d}\Omega} = \frac{\text{scattered flux}}{\text{incident flux}} = |f(K)|^2, \tag{2.3}$$

where the incident flux associated with a plane wave is spatially uniform and reads

$$\mathbf{j} = \frac{\hbar}{2m\mathrm{i}}(\psi^*\nabla\psi - \psi\nabla\psi^*) \quad\Longrightarrow\quad j_{\mathrm{inc}} = \frac{\hbar k_i}{m} = v_i. \tag{2.4}$$

When the incident illumination is no longer translationally invariant, this formalism must be generalized. To explicitly introduce finite wavefront curvature and spatially varying phase, we consider an incident field associated with a point source located at a finite position $\mathbf{r}_s$ with respect to the scattering center. The incident field is then modeled as

$$\varphi(\mathbf{r}) = A\,\frac{e^{\mathrm{i}k_i|\mathbf{r}-\mathbf{r}_s|}}{|\mathbf{r}-\mathbf{r}_s|}, \tag{2.5}$$

where A is a normalization constant fixing the source strength. This expression should be interpreted as a convenient theoretical model of spherical illumination, rather than as a direct representation of a realistic focused probe.

The associated probability current density is

$$j_{\mathrm{inc}}(\mathbf{r}) = \frac{\hbar k_i|A|^2}{m|\mathbf{r}-\mathbf{r}_s|^2}, \tag{2.6}$$

which decays as the inverse square of the distance from the source. If the spatial extent of the scattering region is small compared to the source–target distance, $|\mathbf{r}| \ll |\mathbf{r}_s|$,

---

[1] Throughout this chapter, the analysis is carried out within a non-relativistic framework. As discussed previously, relativistic corrections can be readily recovered by a multiplicative rescaling of the scattering factors by the Lorentz factor γ.

one may approximate $|\mathbf{r} - \mathbf{r}_s| \simeq r_s$, yielding an approximately uniform local incident flux at the target position,

$$j_{\text{inc}} \simeq \frac{\hbar k_i |A|^2}{m r_s^2}. \tag{2.7}$$

This approximation ensures that the notion of a differential cross section remains well defined locally, despite the absence of global translational invariance.

Within the first Born approximation, the total wavefunction can then be written as

$$\psi(\mathbf{r}) = A\left[\frac{e^{\mathrm{i}k_i|\mathbf{r}-\mathbf{r}_s|}}{|\mathbf{r}-\mathbf{r}_s|} - \frac{m}{2\pi\hbar^2}\frac{e^{\mathrm{i}k_f r}}{r}\int \mathrm{d}^3\mathbf{r}'\, e^{-\mathrm{i}\mathbf{k}_f\cdot\mathbf{r}'} V(r') \frac{e^{\mathrm{i}k_i|\mathbf{r}'-\mathbf{r}_s|}}{|\mathbf{r}'-\mathbf{r}_s|}\right]. \tag{2.8}$$

The overall factor A multiplies both the incident and scattered terms, reflecting the linearity of the Born solution with respect to the incident field.

We define the generalized scattering amplitude

$$g(k,\theta,\varphi;\mathbf{r}_s) = -\frac{m}{2\pi\hbar^2}\int \mathrm{d}^3\mathbf{r}'\, e^{-\mathrm{i}\mathbf{k}_f\cdot\mathbf{r}'} V(r') \frac{e^{\mathrm{i}k_i|\mathbf{r}'-\mathbf{r}_s|}}{|\mathbf{r}'-\mathbf{r}_s|}, \tag{2.9}$$

which explicitly depends on the source position $\mathbf{r}_s$ and encodes the effects of finite-distance illumination and wavefront curvature. The corresponding differential cross section is obtained from the ratio between the scattered flux and the local incident flux, Eq. (2.6), and reads

$$\frac{\mathrm{d}\sigma}{\mathrm{d}\Omega} = \frac{k_f}{k_i}\,|\mathbf{r}_s|^2\,|g(k,\theta,\varphi;\mathbf{r}_s)|^2. \tag{2.10}$$

In the limit of an infinitely distant source ($r_s \to \infty$), the curvature of the incident wavefront becomes negligible over the interaction region and the standard plane-wave formalism is recovered. Indeed, for large r_s one may expand

$$|\mathbf{r}' - \mathbf{r}_s| \approx r_s - \hat{\mathbf{r}}_s\cdot\mathbf{r}', \tag{2.11}$$

$$\varphi_{\text{inc}}(\mathbf{r}) \approx A\frac{e^{\mathrm{i}k_i r_s}}{r_s} e^{-\mathrm{i}k_i\hat{\mathbf{r}}_s\cdot\mathbf{r}} = A_{\text{eff}}\, e^{\mathrm{i}\mathbf{k}_i\cdot\mathbf{r}}, \tag{2.12}$$

which leads directly to the usual plane-wave Born result,

$$\frac{\mathrm{d}\sigma}{\mathrm{d}\Omega} = |f(K)|^2, \qquad \text{since} \quad \lim_{r_s\to\infty} |\mathbf{r}_s|\,|g(k,\theta,\varphi;\mathbf{r}_s)| = |f(K)|.$$

This demonstrates that Eq. (2.10) constitutes a consistent generalization of the plane-wave scattering formalism to incident fields with finite wavefront curvature and finite source distance.

2.2 Elastic Scattering with spherical Illumination:

$$e^- + \mathrm{H} \rightarrow e^- + \mathrm{H}$$

We now specialize the general formalism introduced above to the case of elastic electron scattering from a hydrogen atom in its ground state, using an incident field with finite wavefront curvature. A direct generalization of Eq. (2.8) is obtained by describing the incident electron through a spherical-wave illumination associated with a source located at $\mathbf{r}_s$:

$$\psi(\mathbf{r}_1) = A\left\{ \frac{e^{\mathrm{i}k_i|\mathbf{r}_1-\mathbf{r}_s|}}{|\mathbf{r}_1-\mathbf{r}_s|} - \frac{m}{2\pi\hbar^2}\frac{e^{\mathrm{i}k_f r_1}}{r_1} \iint \mathrm{d}^3\mathbf{r}'_1\, \mathrm{d}^3\mathbf{r}'_2\, e^{-\mathrm{i}\mathbf{k}_f\cdot\mathbf{r}'_1} \chi^*(\mathbf{r}'_2)\, V(\mathbf{r}'_1,\mathbf{r}'_2)\, \chi(\mathbf{r}'_2)\, \frac{e^{\mathrm{i}k_i|\mathbf{r}'_1-\mathbf{r}_s|}}{|\mathbf{r}'_1-\mathbf{r}_s|} \right\}. \tag{2.13}$$

The subscripts 1 and 2 distinguish the beam electron from the bound electron of the hydrogen atom. The hydrogen ground state and the interaction potential are given by

$$\chi(\mathbf{r}'_2) = \frac{1}{\sqrt{\pi a_0^3}}\, e^{-r'_2/a_0}, \qquad \text{(hydrogenic 1}s\text{ state)}, \tag{2.14}$$

$$V(\mathbf{r}'_1,\mathbf{r}'_2) = \frac{e^2}{4\pi\varepsilon_0}\left(\frac{1}{|\mathbf{r}'_1-\mathbf{r}'_2|} - \frac{1}{r'_1}\right), \tag{2.15}$$

$$\mathbf{r}_s = (x_s, y_s, z_s), \qquad \text{source position.} \tag{2.16}$$

Restricting the discussion to elastic scattering, one has $\chi^* = \chi$ and $k_f = k_i = k$, and Eq. (2.13) reduces to

$$\psi(\mathbf{r}_1) = A\left\{ \frac{e^{\mathrm{i}k|\mathbf{r}_1-\mathbf{r}_s|}}{|\mathbf{r}_1-\mathbf{r}_s|} - \frac{m}{2\pi\hbar^2}\frac{e^{\mathrm{i}kr_1}}{r_1} \iint \mathrm{d}^3\mathbf{r}'_1\, \mathrm{d}^3\mathbf{r}'_2\, e^{-\mathrm{i}\mathbf{k}_f\cdot\mathbf{r}'_1} \frac{1}{\pi a_0^3} e^{-2r'_2/a_0} V(\mathbf{r}'_1,\mathbf{r}'_2)\, \frac{e^{\mathrm{i}k|\mathbf{r}'_1-\mathbf{r}_s|}}{|\mathbf{r}'_1-\mathbf{r}_s|} \right\}. \tag{2.17}$$

In order to reintroduce the concept of momentum transfer and to connect the spherical illumination to the familiar plane-wave formulation, it is convenient to expand the spherical incident field into a continuous superposition of plane waves using the Weyl representation [45]:

$$\frac{e^{\mathrm{i}k|\mathbf{r}'_1-\mathbf{r}_s|}}{|\mathbf{r}'_1-\mathbf{r}_s|} = \frac{\mathrm{i}}{2\pi}\int \mathrm{d}^2\mathbf{k}_\perp\, \frac{e^{\mathrm{i}\mathbf{k}_\perp\cdot(\mathbf{r}'_{1\perp}-\mathbf{r}_{s\perp})+\mathrm{i}k_z|z'_1-z_s|}}{k_z}, \tag{2.18}$$

where $\mathbf{k} = (\mathbf{k}_\perp, k_z)$ is the incident wavevector and $k_z = \sqrt{k^2 - |\mathbf{k}_\perp|^2}$ is its longitudinal component.

Formally, the Weyl expansion includes transverse wavevectors with $|\mathbf{k}_\perp| > k$, for which k_z becomes purely imaginary and the corresponding contributions decay exponentially along z. These evanescent components describe near-field structure of the Green function and do not propagate energy to the far field. In the present context, which focuses on elastic far-field scattering, their contribution to the observed angular intensity is negligible. Accordingly, the integration is restricted to propagating components,

$$|\mathbf{k}_\perp| \leq k,$$

so that k_z remains real.

Equation (2.18) provides an exact plane-wave decomposition of the spherical Green function. For the purposes of the numerical evaluation that follows, it is convenient to regularize the transverse momentum spectrum by introducing a smooth envelope function. Specifically, we restrict the integration to a forward-propagating cone and weight the transverse components with a Gaussian factor:

$$\frac{e^{\mathrm{i}k|\mathbf{r}_1 - \mathbf{r}_s|}}{|\mathbf{r}_1 - \mathbf{r}_s|} \longrightarrow \frac{\mathrm{i}}{2\pi} \iint \mathrm{d}^2\mathbf{k}_\perp \, \frac{e^{\mathrm{i}\mathbf{k}_\perp \cdot (\mathbf{r}_{1\perp} - \mathbf{r}_{s\perp}) + \mathrm{i}k_z(z_1 - z_s)}}{k_z} \, e^{-\mathbf{k}_\perp^2/2\sigma_k^2}. \tag{2.19}$$

Here σ_k controls the effective transverse momentum spread and sets the maximum angular extent of the illumination.

The Gaussian envelope is introduced solely as a numerically convenient regularization of the Weyl expansion, suppressing high-$k_\perp$ components and ensuring stable convergence of the transverse momentum integrals. Physically, it mimics a finite angular spread of the incident illumination while preserving the essential features associated with finite wavefront curvature and forward propagation[2].

This formulation provides a controlled and transparent way to interpolate between the plane-wave limit and spherical illumination, and it allows the role of source position and symmetry breaking to be analyzed independently of the detailed lens aberration structure that characterizes a realistic STEM probe.

Importantly, the qualitative features of the scattered field derived below—in particular the modification of the angular distribution and the activation of additional

---

[2] In the benchmark comparisons with realistic STEM illumination discussed below, the incident field is instead described using a sharp aperture cutoff (top-hat), consistent with standard electron-optical practice.

angular-momentum channels in the off-axis geometry—do not depend on the specific functional form of the transverse envelope. They are controlled primarily by two ingredients: (i) the loss of global translational invariance introduced by a spherical incident wavefront, and (ii) the restriction of the incident angular spectrum to forward-propagating components within a finite cone.

In the forward-propagating representation adopted here, the longitudinal phase is written with an explicit propagation direction ($z_1 > z_s$), so that the modulus in Eq. (2.18) can be omitted. Accordingly, we use the regularized Weyl form

$$\frac{e^{\mathrm{i}k|\mathbf{r}_1-\mathbf{r}_s|}}{|\mathbf{r}_1-\mathbf{r}_s|} \approx \frac{\mathrm{i}}{2\pi}\iint \mathrm{d}^2\mathbf{k}_\perp \, \frac{e^{\mathrm{i}\mathbf{k}_\perp\cdot(\mathbf{r}_{1\perp}-\mathbf{r}_{s\perp})+\mathrm{i}k_z(z_1-z_s)}}{k_z} \, e^{-\mathbf{k}_\perp^2/2\sigma_k^2}, \tag{2.20}$$

where $\mathbf{r}_{1\perp} = (x_1, y_1)$ and $\mathbf{k}_\perp = (k_x, k_y)$ denote transverse coordinates and momenta, and $k_z = \sqrt{k^2 - |\mathbf{k}_\perp|^2}$ is real for propagating components.

Substituting Eq. (2.20) into Eq. (2.17) and identifying the far-field coefficient of $e^{\mathrm{i}kr_1}/r_1$ yields the generalized elastic scattering amplitude

$$\begin{aligned} g(\mathbf{k}_f) = |\mathbf{r}_s| \Bigg[-\frac{m\mathrm{i}}{(2\pi)^2\hbar^2} \int \mathrm{d}^2\mathbf{k}_\perp \iint \mathrm{d}^3\mathbf{r}'_1 \, \mathrm{d}^3\mathbf{r}'_2 \, e^{-\mathrm{i}\mathbf{k}_f\cdot\mathbf{r}'_1} \, \frac{1}{\pi a_0^3} e^{-2r'_2/a_0} \, \frac{e^2}{4\pi\varepsilon_0} \left(\frac{1}{|\mathbf{r}'_1-\mathbf{r}'_2|} - \frac{1}{r'_1} \right) \\ \times \frac{e^{\mathrm{i}\mathbf{k}_\perp\cdot(\mathbf{r}'_{1\perp}-\mathbf{r}_{s\perp})+\mathrm{i}k_z(z'_1-z_s)}}{k_z} \, e^{-\mathbf{k}_\perp^2/2\sigma_k^2} \Bigg]. \end{aligned} \tag{2.21}$$

The subsequent steps proceed analogously to the plane-wave derivation. Integrating over $\mathbf{r}'_1$ and $\mathbf{r}'_2$ yields

$$\begin{aligned} g(\mathbf{k}_f) = |\mathbf{r}_s| \Bigg[-\frac{m\mathrm{i}}{(2\pi)^2\hbar^2} \frac{1}{\pi a_0^3} \int \frac{\mathrm{d}^2\mathbf{k}_\perp \, e^{-\mathbf{k}_\perp^2/2\sigma_k^2} \, e^{-\mathrm{i}\mathbf{k}\cdot\mathbf{r}_s}}{k_z} \iint \mathrm{d}^3\mathbf{r}'_1 \, \mathrm{d}^3\mathbf{r}'_2 \, e^{-\mathrm{i}\mathbf{k}_f\cdot\mathbf{r}'_1} \times \\ \times e^{-2r'_2/a_0} \, \frac{e^2}{4\pi\varepsilon_0} \left(\frac{1}{|\mathbf{r}'_1-\mathbf{r}'_2|} - \frac{1}{r'_1} \right) e^{\mathrm{i}\mathbf{k}\cdot\mathbf{r}'_1} \Bigg], \end{aligned} \tag{2.22}$$

where $\mathbf{k} = (\mathbf{k}_\perp, k_z)$ and $\mathbf{k}\cdot\mathbf{r}'_1 = \mathbf{k}_\perp\cdot\mathbf{r}'_{1\perp} + k_z z'_1$. Performing the inner integrals as in the plane-wave case gives

$$\int \mathrm{d}^3\mathbf{r}'_1 \, e^{\mathrm{i}\mathbf{K}\cdot\mathbf{r}'_1} \frac{e^2}{4\pi\varepsilon_0} \left(\frac{1}{|\mathbf{r}'_1-\mathbf{r}'_2|} - \frac{1}{r'_1} \right) = \frac{e^2}{\varepsilon_0} \left(\frac{e^{\mathrm{i}\mathbf{K}\cdot\mathbf{r}'_2} - 1}{K^2} \right), \tag{2.23}$$

$$-\frac{me^2}{2\pi^2\hbar^2\varepsilon_0 a_0^3 K^2} \int \mathrm{d}^3\mathbf{r}'_2 \, (e^{\mathrm{i}\mathbf{K}\cdot\mathbf{r}'_2} - 1) \, e^{-2r'_2/a_0} = 2a_0 \, \frac{8 + a_0^2K^2}{(4 + a_0^2K^2)^2}. \tag{2.24}$$

Hence,

$$g(\mathbf{k}_f) = \frac{\mathrm{i}a_0}{\pi} |\mathbf{r}_s| \iint \mathrm{d}^2\mathbf{k}_\perp \, \frac{e^{-\mathrm{i}\mathbf{k}\cdot\mathbf{r}_s}}{k_z} \, e^{-\mathbf{k}_\perp^2/2\sigma_k^2} \, \frac{8 + a_0^2K^2}{(4 + a_0^2K^2)^2}, \tag{2.25}$$

where

$$K^2 = |\mathbf{K}|^2 = |\mathbf{k} - \mathbf{k}_f|^2 = (k_x - k_{fx})^2 + (k_y - k_{fy})^2 + (k_z - k_{fz})^2. \tag{2.26}$$

Since the integration is performed over $\mathrm{d}^2\mathbf{k}_\perp$, *i.e.* over the initial transverse momentum components, it is convenient to express the incident wavevector $\mathbf{k}$ in cylindrical coordinates and the detected direction $\mathbf{k}_f$ in spherical coordinates:

$$\mathbf{k} = (k_\perp \cos\phi_i,\ k_\perp \sin\phi_i,\ k_z), \tag{2.27}$$

$$\mathbf{k}_f = (k \sin\theta_f \cos\varphi_f,\ k \sin\theta_f \sin\varphi_f,\ k \cos\theta_f), \tag{2.28}$$

with $k_z = \sqrt{k^2 - k_\perp^2}$ for elastic scattering. The key difference with respect to the plane-wave formulation is that the incident direction is no longer unique: the scattering amplitude involves an explicit integration over the incident transverse components (k_x, k_y), weighted by the chosen angular spectrum.

In the following we analyze two representative geometries:

(i) an on-axis configuration, in which the source is aligned with the atomic center, and

(ii) an off-axis configuration, in which the source is laterally displaced.

These cases illustrate how spherical illumination and symmetry breaking modify the angular structure of the scattered field.

2.3 On-axis source: $\mathbf{r}_s = (0, 0, z_s)$

The simplest configuration corresponds to a source aligned with the hydrogen atom, which, without loss of generality, is placed at the origin of the coordinate system (see Fig. 2.2).

In this case, axial symmetry is preserved and all quantities are independent of the azimuthal detection angle φ_f. Hence, without loss of generality, we set $\varphi_f = 0$ throughout this section. We write

$$\mathbf{k} = (k_\perp \cos\phi_i,\ k_\perp \sin\phi_i,\ k_z), \tag{2.29}$$

$$\mathbf{k}_f = (k \sin\theta_f,\ 0,\ k \cos\theta_f), \tag{2.30}$$

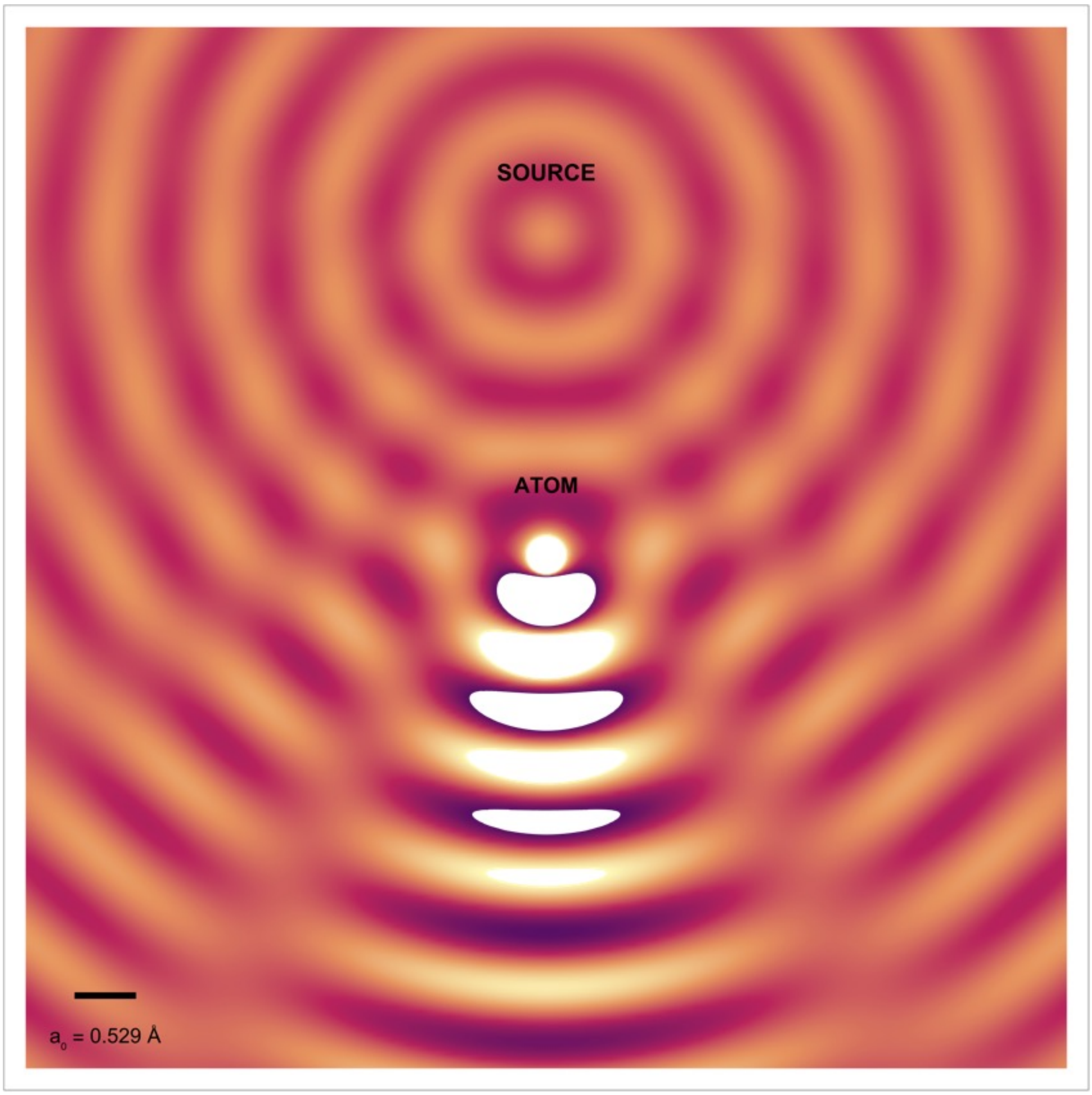

Figure 2.2: Qualitative visualization of elastic electron scattering induced by a spherical incident illumination aligned with the atom. The figure shows the real part of the total wavefunction $\Re[\Psi_{\text{tot}}(x, y)]$, obtained as the superposition of the incident field and the outgoing spherical wave elastically scattered by a single atom located at the origin. The axial alignment preserves cylindrical symmetry, resulting in an azimuthally symmetric interference pattern around the optical axis.

so that $g(\mathbf{k}_f;\mathbf{r}_s) = g(k,\theta_f;z_s)$, where θ_f plays the role of the scattering angle. Equation (2.25) can thus be rewritten as

$$g(k,\theta_f;z_s) = \frac{ia_0}{\pi}\,|z_s| \int_0^{k_{\max}} dk_\perp \int_0^{2\pi} d\phi_i\, k_\perp\, \frac{e^{-ik_z z_s}}{k_z}\, e^{-k_\perp^2/2\sigma_k^2}\, \frac{8 + a_0^2 K^2}{\left(4 + a_0^2 K^2\right)^2}, \tag{2.31}$$

with

$$\begin{aligned} K^2 &= (k_\perp \cos\phi_i - k\sin\theta_f)^2 + (k_\perp \sin\phi_i)^2 + (k_z - k\cos\theta_f)^2 \\ &= 2k^2 - 2k(k_\perp \cos\phi_i \sin\theta_f + k_z \cos\theta_f)\,. \end{aligned} \tag{2.32}$$

The Gaussian envelope naturally limits the range of $k_\perp$ by exponentially suppressing large-angle components. In practice, we truncate the integration at

$$k_{\max} = \min\bigl(k,\, n\sigma_k\bigr), \qquad n \simeq 6\text{–}10, \tag{2.33}$$

which ensures that only propagating modes ($k_z \in \mathbb{R}$) are included while retaining numerical convergence.

Figure 2.3 is presented as a consistency check of the spherical illumination formalism. The source is placed far from the target ($z_s = 1000$ Å), so that the spatial extent of the scattering region is negligible compared to $|\mathbf{r}_s|$. In this regime, the incident wavefront is locally indistinguishable from a plane wave and the standard plane-wave Born result is recovered.

The near-perfect overlap between the spherical-illumination calculation (blue solid curve) and the analytical plane-wave Born amplitude (red dashed curve) confirms the internal consistency of Eq. (2.25) and of the generalized differential cross section in Eq. (2.10). This agreement validates the framework in the asymptotic limit $|\mathbf{r}_s| \to \infty$.

Deviations from plane-wave behavior become appreciable only when the source–target distance is reduced so that the phase curvature across the interaction volume is no longer negligible. In this regime, different regions of the scattering volume experience slightly different local incidence directions and phases, an effect absent in the plane-wave description.

Reducing the source–target distance while preserving the on-axis geometry reveals the onset of finite-distance effects. Figure 2.4 shows the elastic scattering amplitude for an intermediate distance $z_s = 200$ Å, bridging the gap between the asymptotic

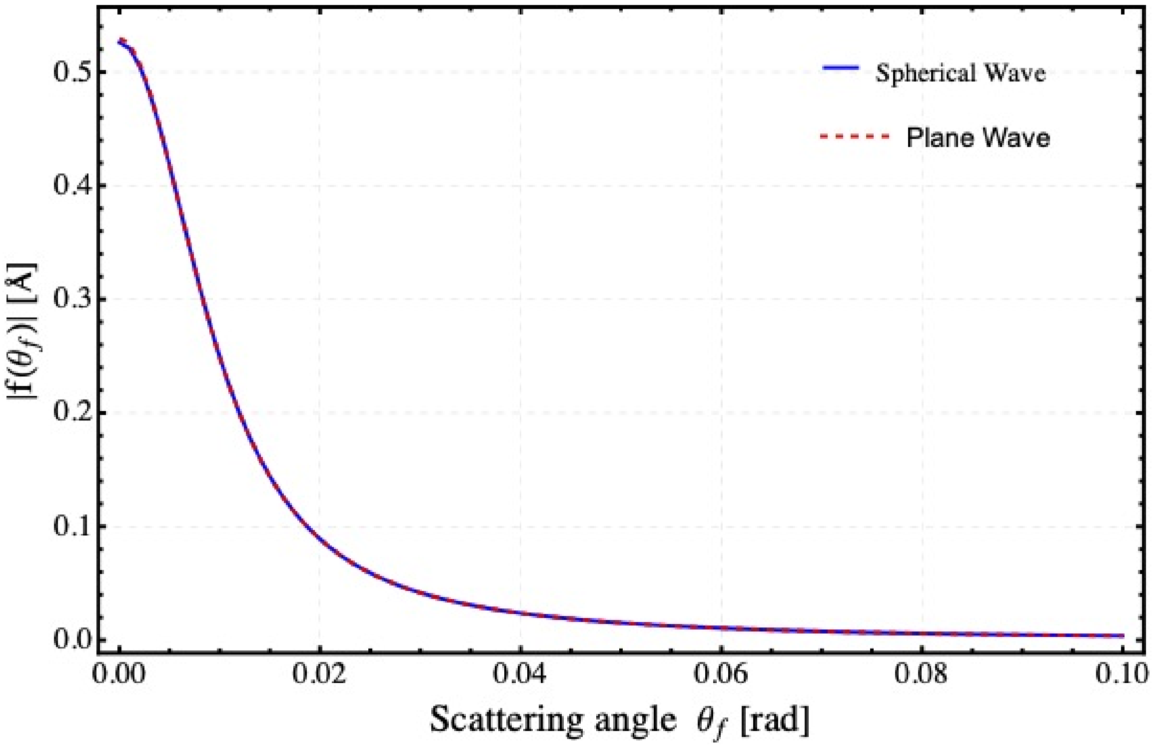

Figure 2.3: Elastic scattering amplitude for an on-axis configuration with $x_s = 0$ Å and $z_s = 1000$ Å. The blue solid line represents the numerical result obtained from the spherical illumination model, while the red dashed line shows the analytical Born result for plane-wave incidence. At large source–target distance the two curves nearly coincide, confirming that the incident wavefront becomes locally indistinguishable from a plane wave within the interaction region.

plane-wave limit and a regime where wavefront curvature becomes noticeable across the interaction region.

At this distance, the spherical-illumination result no longer perfectly overlaps with the plane-wave Born prediction. Although the deviations remain modest, they are systematic and become most pronounced at small scattering angles, where phase curvature plays a dominant role. This reflects the fact that different regions of the interaction volume experience slightly different local incidence directions and phases, an effect absent in the plane-wave description.

As the source approaches the target further, these discrepancies increase and eventually lead to qualitative modifications of the angular distribution. This trend is illustrated in Fig. 2.5, where the source is placed at $z_s = 50$ Å, comparable to the characteristic length scales of the scattering process.

This behavior reflects the progressive departure from the plane-wave regime as the

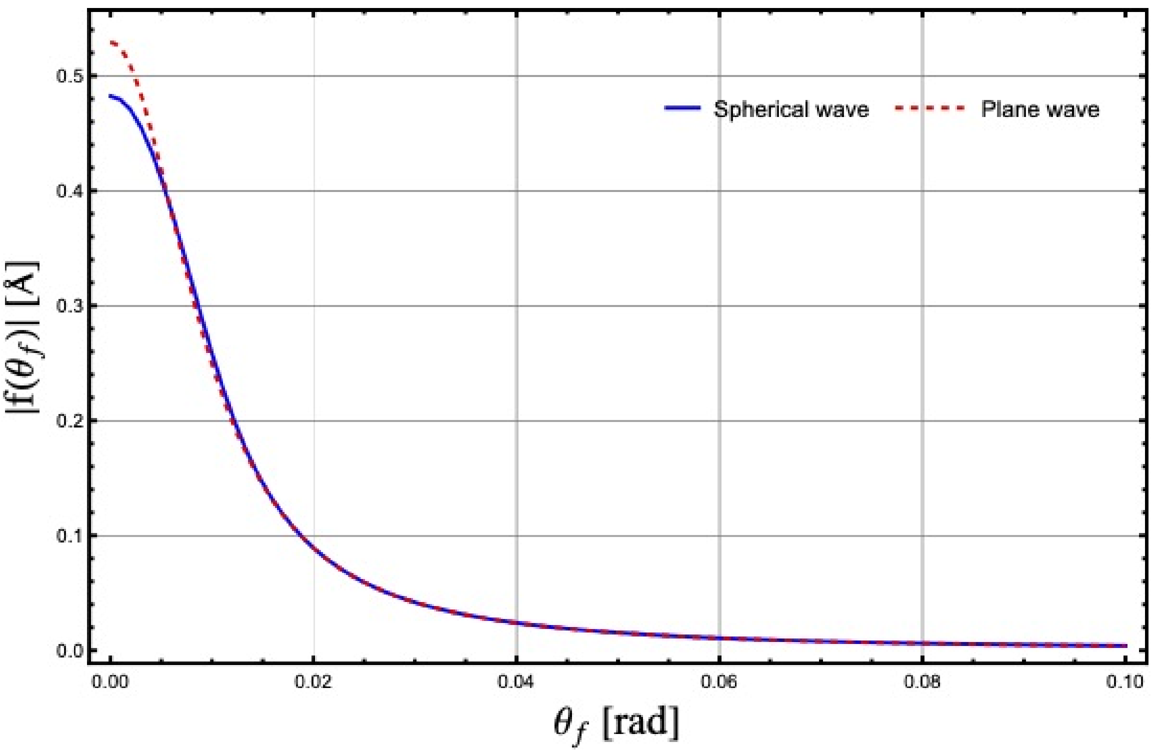

Figure 2.4: Elastic scattering amplitude for an on-axis configuration at an intermediate distance from the target ($x_s = 0$ Å, $z_s = 200$ Å). The spherical-illumination result (blue solid line) starts to deviate from the plane-wave Born prediction (red dashed line), particularly at small scattering angles. This configuration illustrates the gradual breakdown of the plane-wave approximation as the curvature of the incident wavefront becomes non-negligible over the spatial extent of the scattering region.

source–target distance becomes comparable to the spatial extent of the interaction region.

A particularly transparent way to quantify the recovery of the plane-wave regime is to consider the on-axis scattering amplitude at zero scattering angle, $g(0, z_s)$, as a function of the source–target distance. In this configuration the momentum transfer vanishes ($K = 0$), and the plane-wave Born result reduces to the constant analytical value

$$f_{\text{plane}}(0) = a_0.$$

Figure 2.6 shows the quantity $|z_s|\,|g(0, z_s)|$ as a function of z_s, together with the plane-wave limit indicated by the horizontal dashed line. For small source distances, the normalized amplitude is strongly suppressed, reflecting the pronounced curvature and spatial phase variation of the incident wavefront across the interaction region.

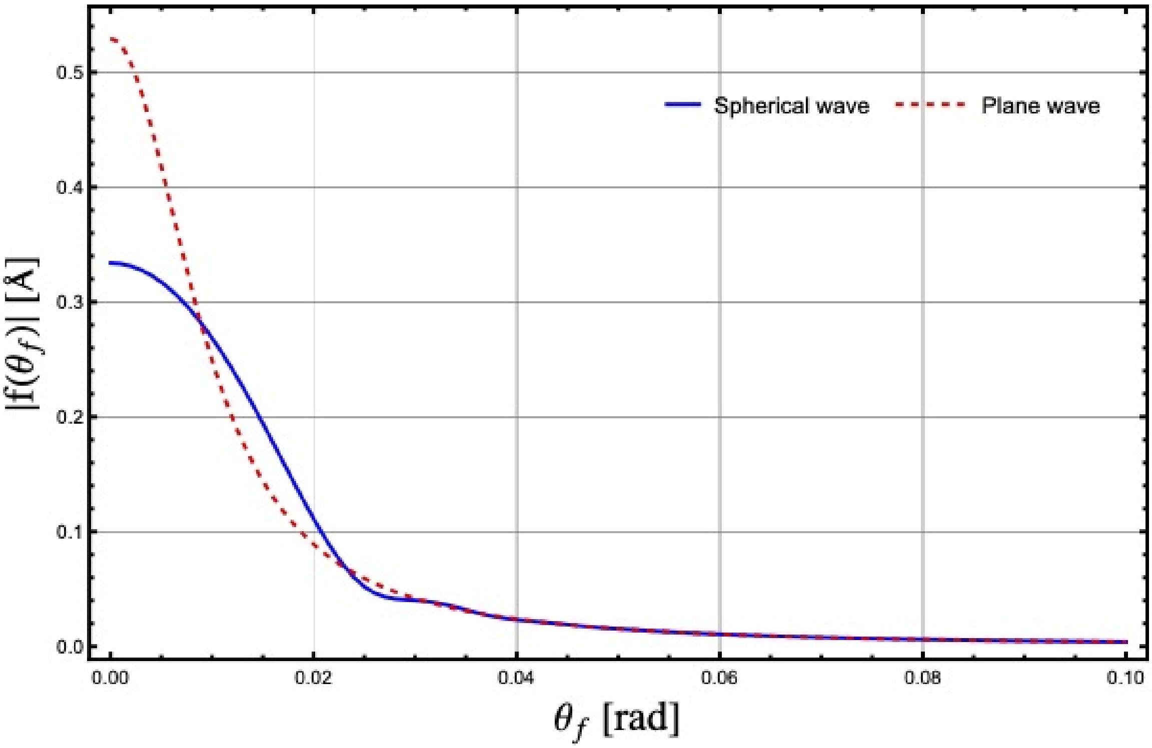

Figure 2.5: Elastic scattering amplitude for an on-axis configuration at short distance ($x_s = 0$ Å, $z_s = 50$ Å). The blue solid line shows the numerical result obtained from the spherical illumination model, while the red dashed line corresponds to the analytical Born prediction for plane-wave incidence. The finite curvature of the incident wavefront produces a noticeable reduction and reshaping of the angular dependence compared to the plane-wave result.

As the source is moved away from the target, the spherical wavefront becomes progressively flatter on the scale of the atomic potential, and the scattering amplitude converges monotonically toward the plane-wave value. This plot provides a direct and quantitative estimate of the spatial scale over which finite-curvature effects remain relevant. The plane-wave regime is recovered only when the source–target distance becomes large compared to the characteristic size of the scattering potential, here set by the Bohr radius a_0. In this sense, z_s acts as a purely geometrical control parameter governing the crossover between localized (spherical) and translationally invariant (plane-wave) illumination.

It is important to stress that the parameter z_s introduced here should not be identified with the physical distance between the electron source and the specimen in a realistic (S)TEM instrument, which is typically of the order of millimeters to meters. Rather, z_s should be interpreted as an effective geometrical parameter controlling the

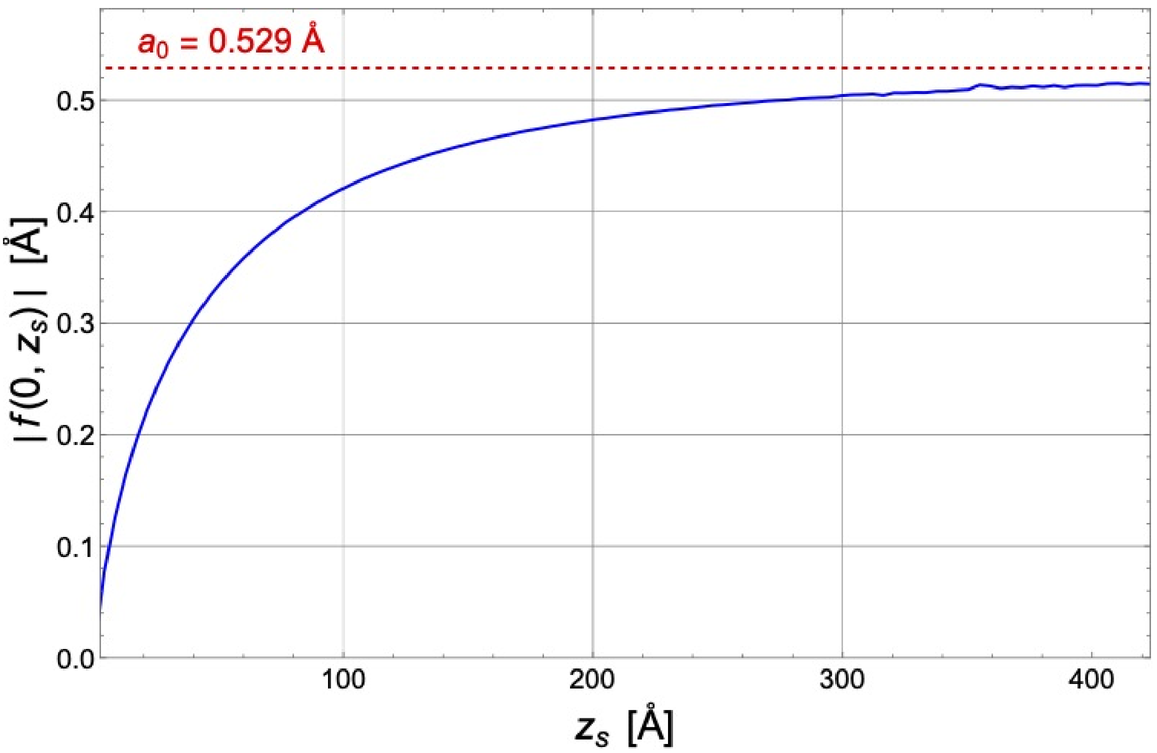

Figure 2.6: On-axis elastic scattering amplitude at zero scattering angle, normalized by the source–target distance, as a function of the source position z_s. The quantity $|z_s|\,|g(0,z_s)| = |f(0,z_s)|$ is shown for spherical illumination and compared with the plane-wave Born limit, indicated by the horizontal dashed line at $f_{\text{plane}}(0) = a_0$. As the source is moved away from the target, the normalized spherical-wave amplitude converges monotonically to the plane-wave value. The figure illustrates quantitatively how the plane-wave regime is recovered when the source–target distance becomes large compared to the characteristic spatial extent of the scattering potential.

local curvature of the incident wavefront at the scale of the interaction region.

In a real microscope, the incident probe is formed by a complex electron-optical system, and its local phase curvature at the specimen plane is determined by the objective lens, convergence angle, and aberrations, rather than by the actual distance to the emission source. The present spherical-wave model should therefore be regarded as a simplified theoretical construct that mimics finite-curvature illumination in a controlled way, without attempting a literal representation of the full electron-optical geometry.

2.4 Off-axis source: $\mathbf{r}_s = (x_s, 0, z_s)$

A more general and physically richer situation arises when the source is laterally displaced with respect to the target (see Fig. 2.7).

In this configuration, axial symmetry is lost and the generalized scattering amplitude depends on both the polar and azimuthal detection angles, $g = g(k, \theta_f, \varphi_f; \mathbf{r}_s)$. Without loss of generality, we set $\mathbf{r}_s = (x_s, 0, z_s)$, corresponding to a displacement along the x axis. Equation (2.25) becomes

$$g(k, \theta_f, \varphi_f; \mathbf{r}_s) = \frac{ia_0}{\pi} |\mathbf{r}_s| \int_0^{k_{\max}} dk_\perp \int_0^{2\pi} d\phi_i \, k_\perp \, e^{-ik_\perp x_s \cos\phi_i} \, \frac{e^{-ik_z z_s}}{k_z} \, e^{-k_\perp^2/2\sigma_k^2} \, \frac{8 + a_0^2 K^2}{(4 + a_0^2 K^2)^2}, \tag{2.34}$$

where

$$\begin{aligned} K^2 &= (k_\perp \cos\phi_i - k \sin\theta_f \cos\varphi_f)^2 + (k_\perp \sin\phi_i - k \sin\theta_f \sin\varphi_f)^2 + (k_z - k\cos\theta_f)^2 \\ &= 2k^2 - 2k[k_\perp \sin\theta_f \cos(\varphi_f - \phi_i) + k_z \cos\theta_f]\,. \end{aligned} \tag{2.35}$$

The exponential factor $e^{-ik_\perp x_s \cos\phi_i}$ encodes the transverse phase gradient introduced by the lateral displacement of the source and couples the azimuthal integration variable ϕ_i to the detection azimuth φ_f. As a result, the amplitude $g(k, \theta_f, \varphi_f; \mathbf{r}_s)$ does not factorize, and axial symmetry is broken.

These results demonstrate how lateral displacement modifies the angular structure of the scattered field. At large z_s the plane-wave limit is recovered, whereas at finite distances and nonzero x_s the broken axial symmetry activates additional angular components and produces azimuthally modulated scattering profiles. Such effects are relevant whenever the incident illumination possesses a controlled phase gradient or an off-axis angular spectrum, and they provide a useful reference for understanding how symmetry breaking can redistribute scattering intensity among angular channels.

2.4.1 Relation to multislice STEM simulations

In practical STEM modeling, probe formation and propagation through a specimen are routinely described within the multislice formalism [21], which numerically solves the (paraxial) Schrödinger equation for a given illumination function. As a result, multislice naturally captures the dependence of scattering signals on probe displacement, convergence angle, defocus, and aberrations.

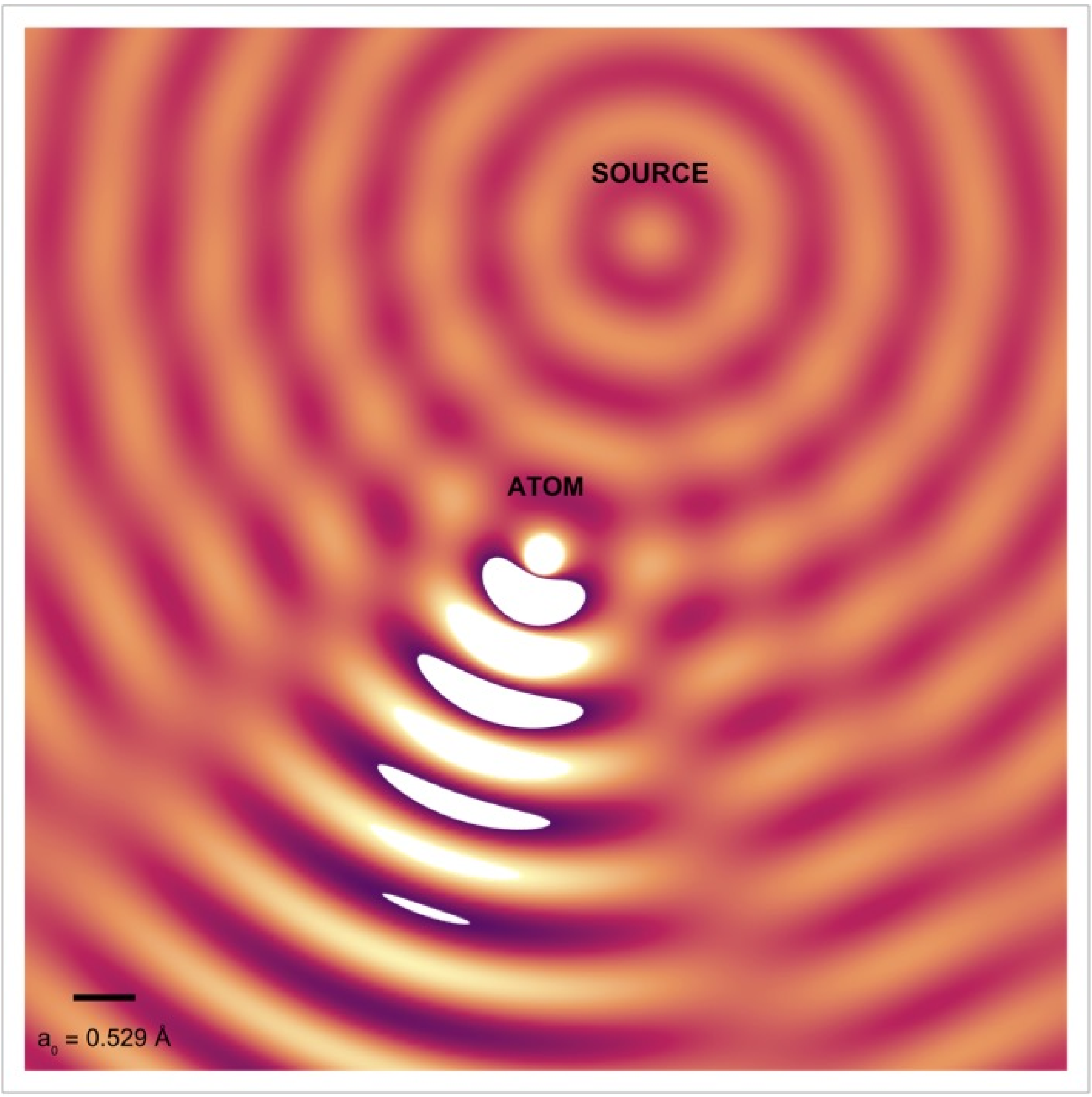

Figure 2.7: Qualitative visualization of elastic scattering induced by a spherical incident illumination laterally displaced with respect to the atom. The real part of the total wavefunction $\Re[\Psi_{\mathrm{tot}}(x, y)]$ is shown as the superposition of the incident field and the outgoing elastically scattered wave from a single atom located at the origin. The lateral displacement breaks axial symmetry, resulting in an asymmetric interference pattern that highlights the geometrical dependence of the scattering process.

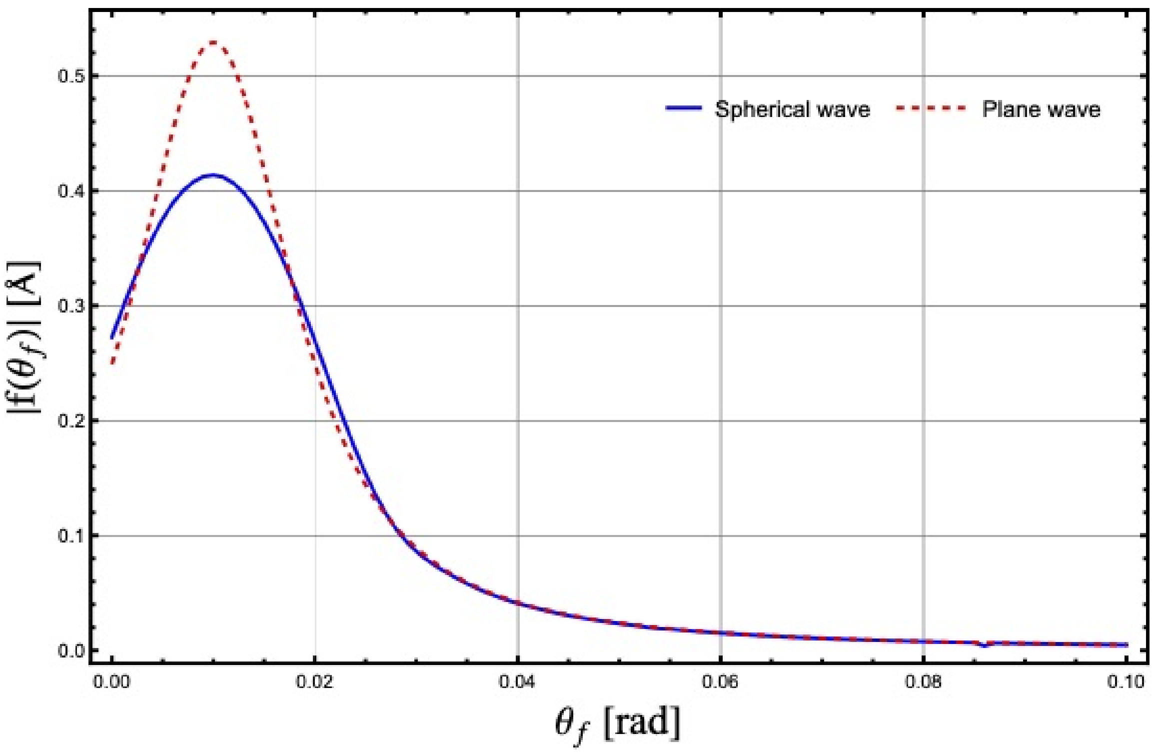

Figure 2.8: Elastic scattering amplitude for an off-axis configuration with $x_s = 1$ Å and $z_s = 100$ Å. The blue solid line represents the numerical result obtained from the spherical illumination model, while the red dashed line shows the analytical Born result for plane-wave incidence. The lateral displacement breaks cylindrical symmetry, producing an azimuthally dependent profile and a moderate reduction in overall amplitude.

The purpose of the present semi-analytical treatment is complementary. Rather than providing a full instrument-level simulation, it isolates, within a controlled Born framework, the specific effects of finite-curvature and off-axis illumination on the scattering process. In particular, the loss of global translational and azimuthal symmetry activates additional angular-momentum components in the scattering amplitude, which are often difficult to disentangle in fully numerical approaches. This channel-based viewpoint, together with the explicit recovery of the plane-wave limit, provides a transparent analytical reference for interpreting trends observed in multislice STEM calculations.

Concerning the role of the parameter z_s, it should be stressed that it does not represent a literal source–specimen distance in a microscope. Instead, z_s is an effective parameter controlling the local curvature of the incident wavefront at the interaction region. In realistic electron optics, this curvature is determined by lens focusing

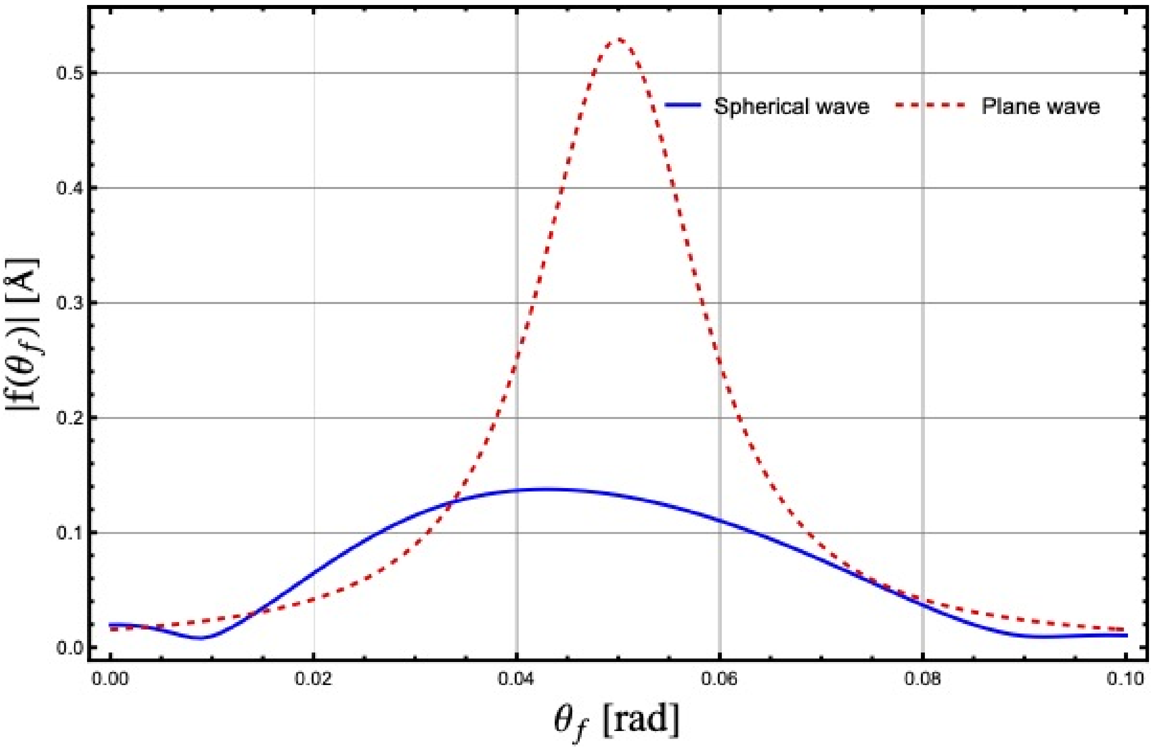

Figure 2.9: Elastic scattering amplitude for an off-axis, nearby configuration with $x_s = 1$ Å and $z_s = 20$ Å. At short source distances, the stronger phase curvature and lateral phase gradient significantly reshape both the magnitude and angular dependence of the scattering pattern, leading to a pronounced redistribution of intensity compared to plane-wave incidence (red dashed line).

and aberrations and is therefore already encoded in the incident probe function used in multislice simulations. From this perspective, the present model does not aim to introduce additional physical effects beyond those captured by multislice in the paraxial regime, but rather to provide an analytical benchmark and a symmetry-based interpretation of probe-dependent scattering.

2.4.2 Geometrical remark: relation to an on-axis configuration

The off-axis geometry considered here can be made formally equivalent to an on-axis configuration through a rigid rotation of the coordinate system. By choosing a rotated axis $\hat{\mathbf{z}}'$ aligned with the source position $\mathbf{r}_s$, one obtains

$$\mathbf{r}'_s = (0, 0, z'_s), \qquad z'_s = \sqrt{x_s^2 + z_s^2},$$

so that the incident field becomes axially symmetric with respect to the new axis.

However, the measurable quantity in the present problem is the scattering amplitude into a fixed laboratory detector direction $\mathbf{k}_f = (k, \theta_f, \varphi_f)$. Under the same rotation, the detector direction would generally transform to a different pair (θ'_f, φ'_f). Therefore, while the rotated viewpoint is useful for interpreting the geometric origin of the symmetry breaking, it does not eliminate the off-axis character of the problem when the detector is kept fixed in the laboratory frame. For this reason, the explicit dependence on the lateral source coordinate x_s in Eq. (2.34) remains physically meaningful, as it quantifies how a lateral phase gradient in the incident illumination redistributes intensity over a given detector geometry.

2.5 Numerical Evaluation and Physical Discussion

This section presents a numerical evaluation of the spherical-illumination scattering amplitude derived from Eq. (2.25), implemented in MATHEMATICA. The aim is to provide a quantitative comparison between spherical-wave and plane-wave scattering factors and to analyze the influence of the parameters controlling the incident angular spectrum and the source position $\mathbf{r}_s$.

The numerical implementation performs a two-dimensional integration over the transverse momentum components (k_x, k_y), expressed in cylindrical coordinates as $(k_\perp, \phi_i)$, while keeping the scattering direction (θ_f, φ_f) fixed. For computational efficiency, the Gaussian envelope is truncated at $k_\perp \leq 6\sigma_k$ (up to $10\sigma_k$ for convergence tests), ensuring that only propagating components with real $k_z = \sqrt{k^2 - k_\perp^2}$ contribute, while evanescent terms remain negligible in the far-field elastic signal.

The parameter σ_k controls the effective transverse momentum spread and may, if desired, be related to an effective cone semi-angle α through $\sigma_k = k \sin\alpha$. In the following, σ_k is used as a convenient measure of the angular spread of the illumination, interpolating between a near-plane-wave spectrum (small σ_k) and a broader forward cone (larger σ_k).

The scattering amplitude is evaluated as

$$g(k, \theta_f, \varphi_f) = \frac{\mathrm{i}a_0}{\pi} |\mathbf{r}_s| \int_0^{k_{\perp,\max}} \mathrm{d}k_\perp \int_0^{2\pi} \mathrm{d}\phi_i \, k_\perp \, \frac{e^{-\mathrm{i}[k_z z_s + k_\perp x_s \cos\phi_i]}}{k_z} \, e^{-k_\perp^2/2\sigma_k^2} \, \frac{8 + a_0^2 K^2}{(4 + a_0^2 K^2)^2}, \tag{2.36}$$

where

$$K^2 = (k_\perp \cos\phi_i - k \sin\theta_f \cos\varphi_f)^2 + (k_\perp \sin\phi_i - k \sin\theta_f \sin\varphi_f)^2 + (k_z - k \cos\theta_f)^2,$$

and $k_{\perp,\max} \in [6\sigma_k, 10\sigma_k]$ ensures numerical convergence. The modulus $|g|$, together with the normalization introduced in Eq. (2.10), provides the quantity proportional to the observable elastic scattering factor for the present illumination model.

2.5.1 Comparison between spherical-wave and plane-wave scattering

In the standard plane-wave formalism, translational invariance implies that the elastic scattering factor depends only on the momentum transfer

$$K = 2k \sin\left(\frac{\theta_f}{2}\right), \tag{2.37}$$

yielding the analytical Born result for scattering from a hydrogenic $1s$ orbital:

$$f_{\text{plane}}(K) = 2a_0 \, \frac{8 + a_0^2 K^2}{(4 + a_0^2 K^2)^2}. \tag{2.38}$$

When the incident illumination is described by a finite-curvature wavefront, global translational symmetry is lost and the scattering factor $g(k, \theta_f, \varphi_f; \mathbf{r}_s)$ depends explicitly on both the detection direction and the source position $\mathbf{r}_s = (x_s, 0, z_s)$. Numerical evaluations show that this geometrical modification leads to systematic changes in both the magnitude and the angular dependence of the elastic scattering signal.

Two main physical effects can be identified:

1. **Amplitude reduction and angular smoothing.** The spatially varying phase associated with a curved wavefront causes contributions from different regions of the interaction volume to interfere less constructively than in the plane-wave case. As a consequence, the coherent elastic amplitude $|g|$ is generally reduced, and its angular dependence appears smoother than that of $|f_{\text{plane}}|$.

2. **Azimuthal modulation due to symmetry breaking.** For laterally displaced configurations ($x_s \neq 0$), the phase factor $e^{-\mathrm{i}[k_z z_s + k_\perp x_s \cos\phi_i]}$ introduces an explicit coupling between the incident azimuth ϕ_i and the detector azimuth φ_f. This breaks cylindrical symmetry and produces azimuthally dependent scattering patterns, including intensity redistributions and interference-like modulations in the diffraction plane. More generally, analogous asymmetries arise whenever the incident illumination carries a controlled phase gradient or an off-axis angular spectrum.

2.5.2 Relation to a realistic STEM probe: aperture formalism, phase structure, and limits of equivalence

The spherical-wave illumination model introduced in this chapter has been specifically designed to break translational invariance and to isolate the role of finite wavefront curvature and lateral phase gradients in elastic scattering within the first Born approximation. Since, in scanning transmission electron microscopy, the incident field is not emitted as a free-space point source but is instead generated by electron-optical elements, it is essential to clarify the precise relation between the present model and a realistic STEM probe, as well as the scope and limitations of any possible equivalence between the two descriptions.

2.5.3 STEM probe formation at the specimen plane

In coherent STEM, the electron probe at the specimen plane ($z = 0$) is formed by the condenser–objective lens system as a coherent superposition of plane-wave components confined within a finite angular aperture. In reciprocal space, the probe wavefunction can be written as

$$\psi_{\mathrm{STEM}}(\mathbf{r}_\perp, 0) = \mathcal{N} \iint_{|\mathbf{k}_\perp| \le k \sin\alpha} A(\mathbf{k}_\perp)\, \exp\big[-i\,\chi(\mathbf{k}_\perp)\big]\, \exp\big(i\mathbf{k}_\perp \cdot \mathbf{r}_\perp\big)\, \mathrm{d}^2\mathbf{k}_\perp, \quad (2.39)$$

where α is the convergence semi-angle, $A(\mathbf{k}_\perp)$ describes the illumination of the objective aperture (and may include partial-coherence envelopes), and $\chi(\mathbf{k}_\perp)$ is the aberration phase function imposed by the electron-optical system.

For a rotationally symmetric and isotropic probe, the aberration phase may be expanded in powers of the spatial frequency as

$$\chi(q) = \pi\lambda\, \Delta f\, q^2 + \frac{\pi}{2} C_s\, \lambda^3 q^4 + \cdots, \quad (2.40)$$

where $q = \sin\theta/\lambda \simeq \theta/\lambda$, Δf is the defocus, and C_s is the spherical aberration coefficient.[3] To connect this standard electron-optical notation with the scattering formalism adopted throughout the present work, it is convenient to rewrite the aber-

---

[3] In conventional (non-aberration-corrected) transmission and scanning transmission electron microscopes, the spherical aberration coefficient C_s of the objective lens typically ranges between 0.5 and 2 mm, with values around 1 mm being common in modern uncorrected instruments.

ration phase in terms of the transverse wavevector $k_\perp$. For small convergence angles,

$$k_\perp = k \sin\theta \simeq \frac{2\pi}{\lambda}\,\theta, \qquad q \simeq \frac{k_\perp}{2\pi}, \tag{2.41}$$

which leads to

$$\chi(k_\perp) = \pi\lambda\,\Delta f \left(\frac{k_\perp}{2\pi}\right)^2 + \frac{\pi}{2} C_s\,\lambda^3 \left(\frac{k_\perp}{2\pi}\right)^4 + \cdots . \tag{2.42}$$

Equation (2.39) highlights that, even for an ideal aberration-free instrument, a STEM probe is fundamentally characterized by a restricted angular spectrum and by a phase structure imposed by electron optics, rather than by a free-space Green function. The probe corresponds to a *converging* wavefield toward a focal point, and not to a diverging spherical wave emitted from a localized source. Any formal comparison with spherical-wave illumination must therefore be understood as a comparison at the level of the wavefront structure at the specimen plane, rather than as a statement about global propagation.

2.5.4 Role of the specimen plane in the Born approximation

Within the first Born approximation, the elastic scattering amplitude is given by the standard expression (1.43), which may be written as

$$f \;\propto\; \int \mathrm{d}^3\mathbf{r}\,\varphi_{\mathrm{inc}}(\mathbf{r})\,V(\mathbf{r})\,e^{-i\mathbf{k}_f\cdot\mathbf{r}}. \tag{2.43}$$

For elastic scattering from a localized atomic potential, the dominant contribution to the scattering integral arises from the spatial region where the incident wavefield overlaps with the specimen, i.e. from the immediate vicinity of the specimen plane ($z = 0$). As a result, the scattering process is sensitive only to the local amplitude and phase structure of the incident wavefront at the sample, and not to the global propagation characteristics of the field away from the interaction region.

This observation implies that any meaningful comparison between different illumination models—such as a free-space spherical wave and a focused STEM probe—must be carried out at the level of the wavefront evaluated at the specimen plane. All equivalence statements discussed in the following sections are therefore understood in this restricted and physically motivated sense, and are specific to the first Born approximation and to localized scattering potentials.

2.5.5 Spherical wave and Weyl expansion

A free-space spherical Green function centered at the source position $\mathbf{r}_s$ may be expressed, for forward-propagating components, as a continuous superposition of plane waves through the Weyl expansion,

$$\frac{e^{ik|\mathbf{r}-\mathbf{r}_s|}}{|\mathbf{r}-\mathbf{r}_s|} \simeq \frac{i}{2\pi} \iint \frac{\mathrm{d}^2\mathbf{k}_\perp}{k_z} \exp\Big[i\mathbf{k}_\perp \cdot (\mathbf{r}_\perp - \mathbf{r}_{s\perp}) + ik_z(z - z_s)\Big], \qquad k_z = \sqrt{k^2 - k_\perp^2}. \tag{2.44}$$

This representation makes explicit that a spherical wave may be viewed as a superposition of plane-wave components spanning a continuous angular spectrum, with amplitudes weighted by the longitudinal wavevector k_z. It therefore provides a natural framework for comparing spherical-wave illumination with aperture-limited STEM probes, which are likewise constructed as superpositions of plane waves with transverse wavevectors $|\mathbf{k}_\perp| \leq k \sin\alpha$.

In the paraxial regime ($k_\perp \ll k$), the longitudinal wavevector admits the well-known expansion

$$k_z \simeq k - \frac{k_\perp^2}{2k} - \frac{k_\perp^4}{8k^3} + O(k_\perp^6), \tag{2.45}$$

which separates the rapidly varying carrier phase from the slowly varying transverse phase terms responsible for wavefront curvature and higher-order aberration-like effects.

2.5.6 Local phase curvature and effective defocus

Substituting Eq. (2.45) into the longitudinal phase factor $\exp[-ik_z z_s]$ appearing in Eq. (2.44), and discarding the irrelevant global phase factor $\exp(-ikz_s)$, one obtains

$$e^{-ik_z z_s} = \exp\Big[+i\,\frac{z_s}{2k}\,k_\perp^2 + i\,\frac{z_s}{8k^3}\,k_\perp^4 + O(k_\perp^6)\Big]\,. \tag{2.46}$$

The leading quadratic term in Eq. (2.46) has the same functional dependence on $k_\perp$ as the defocus contribution to the STEM aberration phase,

$$\chi_{\text{def}}(k_\perp) = -\frac{\Delta f}{2k}\,k_\perp^2. \tag{2.47}$$

As a consequence, within the paraxial regime and over a sufficiently narrow angular spectrum, a spherical wave can *locally* reproduce the phase curvature of a defocused

STEM probe at the specimen plane. This correspondence may be expressed in terms of an effective defocus parameter,

$$\Delta f_{\text{eff}} \simeq s\, z_s, \tag{2.48}$$

where the sign factor $s = \pm 1$ depends on whether the spherical wave is converging or diverging and on the adopted phase convention.

It is important to emphasize that this equivalence is strictly local and limited to the quadratic phase term. The spherical wave does not possess a true focal plane in the optical sense, and the higher-order terms in Eq. (2.46) have no direct counterpart in a purely defocus-tuned STEM probe. These higher-order contributions ultimately limit the validity of the spherical–STEM equivalence and become increasingly relevant for larger angular apertures or when spherical aberration is present.

2.5.7 Benchmarking spherical illumination against STEM probes: caustics and specimen-plane profiles

The relation between spherical illumination and aperture-based STEM probes, previously discussed at the level of angular spectra and phase structure, is further illustrated here through a set of representative wavefront-level figures. These figures are not intended as instrument-level STEM simulations. Rather, they provide controlled diagnostics aimed at clarifying which aspects of the incident field can be meaningfully compared within the Born-scattering framework, and which differences are intrinsic and unavoidable.

Two complementary classes of figures are considered: (i) longitudinal intensity maps $I(x,z)$ (caustics), and (ii) complex line profiles of the incident wavefunction at the specimen plane, $\psi(x, z = 0)$, displayed through their intensity, real part, and imaginary part.

For all STEM-probe figures shown in this section, the convergence semi-angle and defocus are chosen consistently with the Scherzer condition [46],

$$\alpha_{\text{Sch}} = 1.4\,(\lambda/C_s)^{1/4}, \qquad \Delta f_{\text{Sch}} = -\sqrt{C_s \lambda}, \tag{2.49}$$

which defines the optimal compromise between defocus and spherical aberration in conventional electron optics and provides a common, physically meaningful reference condition across all comparisons. Throughout this section, the electron wavelength is fixed to $\lambda = 0.02\,\text{Å}$, the spherical aberration coefficient to $C_s = 1.0 \times 10^7\,\text{Å}$, yielding $\Delta f_{\text{Sch}} = -4.47 \times 10^2\,\text{Å}$ and $\alpha_{\text{Sch}} = 9.36 \times 10^{-3}\,\text{rad}$. All STEM-probe figures use this convergence semi-angle, $\alpha = \alpha_{\text{Sch}}$, while spherical-wave illumination is evaluated with a fixed source position $z_s = 50\,\text{Å}$ and the same angular aperture.

Longitudinal intensity maps $I(x, z)$

The first class consists of two-dimensional intensity maps,

$$I(x, z) = |\psi(x, z)|^2, \tag{2.50}$$

displayed as a function of a transverse coordinate x and the propagation direction z. Such caustics provide a compact visualization of how the angular spectrum and the associated phase structure shape the global beam envelope during propagation, making them useful for qualitative comparisons of different illumination models.

Figure 2.10 shows the caustic corresponding to spherical illumination with a source position $z_s = 50\,\text{Å}$, evaluated using the same angular aperture as the STEM probes. While the wavefront can be tuned to locally reproduce a given phase curvature at the specimen plane, the overall propagation pattern already reflects the presence of higher-order paraxial terms that are rigidly fixed by free-space propagation and cannot be independently adjusted.

Figure 2.11 shows the corresponding caustic for a defocus-only STEM probe ($C_s = 0$) with $\Delta f = -z_s$. In this case, the quadratic phase curvature of the STEM probe matches that of the spherical wave at the specimen plane, resulting in a qualitatively similar paraxial propagation near $z = 0$, despite the fundamentally different physical origins of the two fields.

By contrast, Fig. 2.12 shows the caustic of a Scherzer-tuned STEM probe. Here, the presence of a genuine $k_\perp^4$ aberration term produces a markedly different propagation behavior, which cannot be reproduced by free-space spherical illumination through a single geometrical parameter such as the source position z_s.

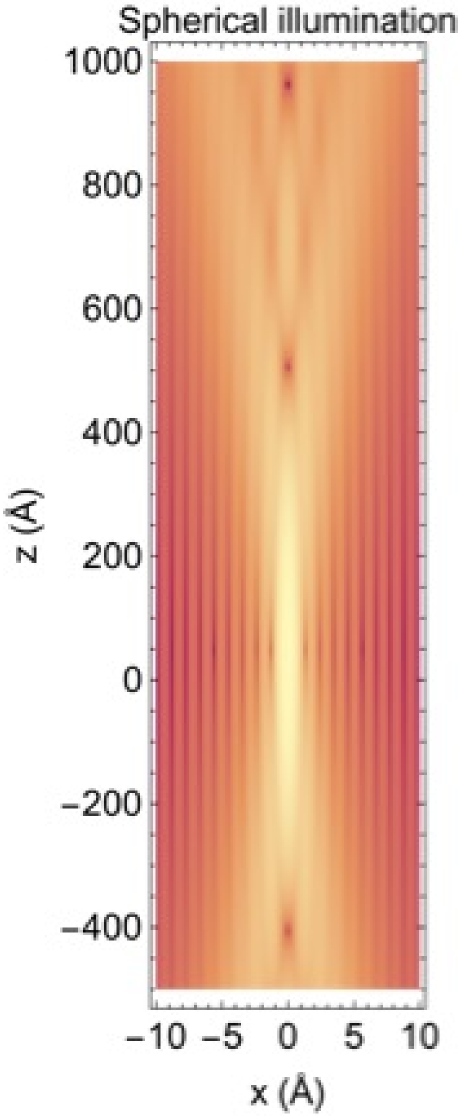

Figure 2.10: Longitudinal intensity map (caustic) $I(x,z) = |\psi(x,z)|^2$ for spherical illumination with source position $z_s = 50\,\text{Å}$, evaluated using the same angular aperture as the STEM probes ($\alpha = \alpha_{\text{Sch}}$).

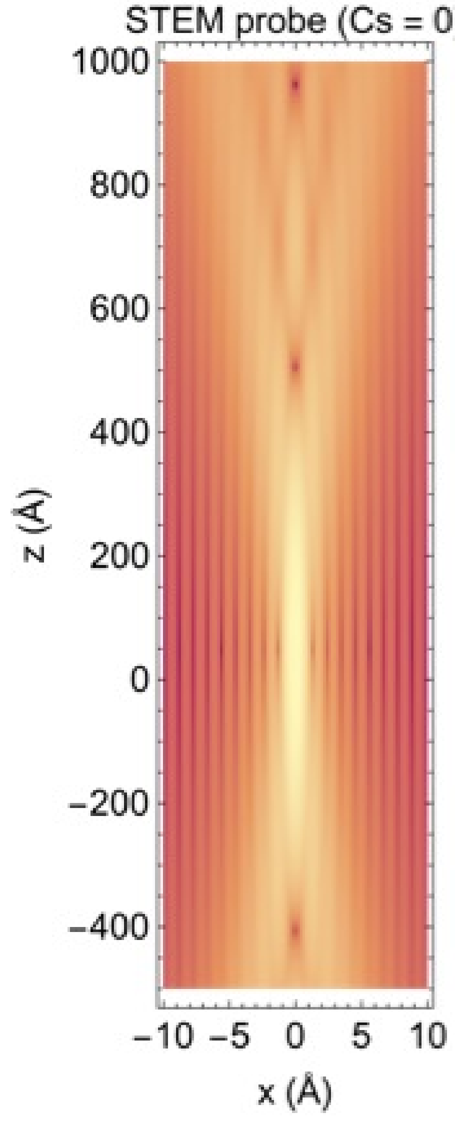

Figure 2.11: Longitudinal intensity map (caustic) for a defocus-only STEM probe ($C_s = 0$, $\Delta f = -z_s = -50\,\text{Å}$), evaluated with convergence semi-angle $\alpha = \alpha_{\text{Sch}}$.

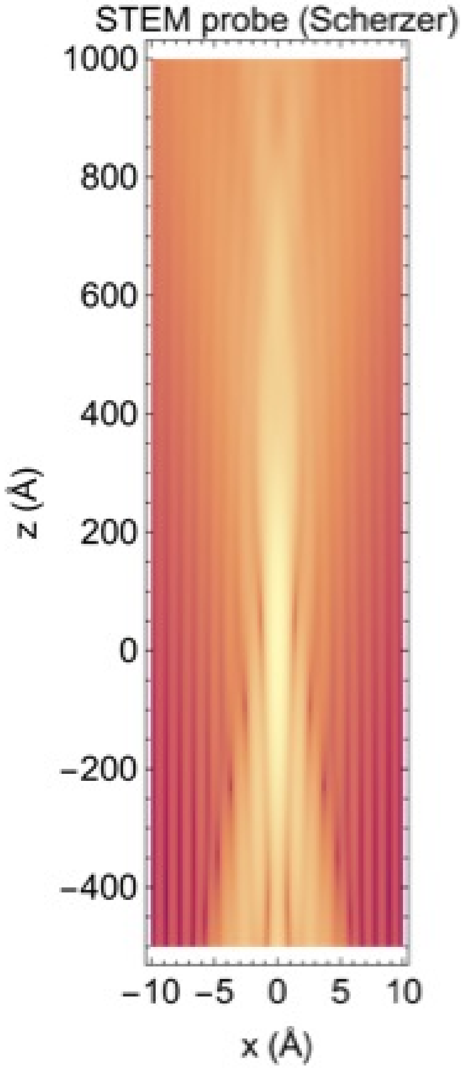

Figure 2.12: Longitudinal intensity map (caustic) for a Scherzer-tuned STEM probe ($C_s = 1.0 \times 10^7$ Å), with defocus $\Delta f_{\mathrm{Sch}} = -\sqrt{C_s \lambda} = -447$ Å and convergence semi-angle $\alpha_{\mathrm{Sch}} = 9.36 \times 10^{-3}$ rad.

These longitudinal intensity maps are not intended to suggest that elastic scattering depends on the full propagation history of the beam. Rather, they provide essential qualitative context for the specimen-plane analysis by making explicit that any apparent similarity between spherical illumination and a STEM probe is necessarily local, aperture-dependent, and limited to specific phase terms. The physically relevant comparison for scattering within the Born approximation is therefore carried out at the level of the wavefront evaluated at the specimen plane, which is addressed in the following subsection.

In this context, the Scherzer-tuned probe is adopted throughout this work as the natural reference condition for realistic STEM illumination. It reflects the optimal compromise imposed by electron optics in the presence of spherical aberration and provides a consistent benchmark, even when no quantitative equivalence with spherical-wave illumination exists.

Specimen-plane profiles at $z = 0$

The second class of figures focuses on the incident wavefunction evaluated directly at the specimen plane, $z = 0$, which is the spatial region sampled by the Born scattering integral for a localized atomic potential. As discussed above, it is this local wavefront—rather than the global propagation behavior—that determines the elastic scattering amplitude within the first Born approximation. All three profiles shown below are computed using the same convergence semi-angle, $\alpha = \alpha_{\mathrm{Sch}} = 1.4(\lambda/C_s)^{1/4}$, i.e. with the same aperture cutoff $k_{\perp,\mathrm{max}} = k \sin\alpha$.

Figure 2.13 shows the specimen-plane intensity profile $|\psi(x,0)|^2$ for spherical illumination and for the two representative STEM probes considered here. While the probe widths may appear comparable over a limited spatial range, intensity alone does not capture the phase structure of the incident field and therefore provides only partial information about the scattering-relevant wavefront.

Additional insight is provided by the real part of the wavefunction, shown in Fig. 2.14. Phase variations across the probe, which are completely invisible in the intensity profile, become explicit and directly influence the coherent superposition entering the scattering integral.

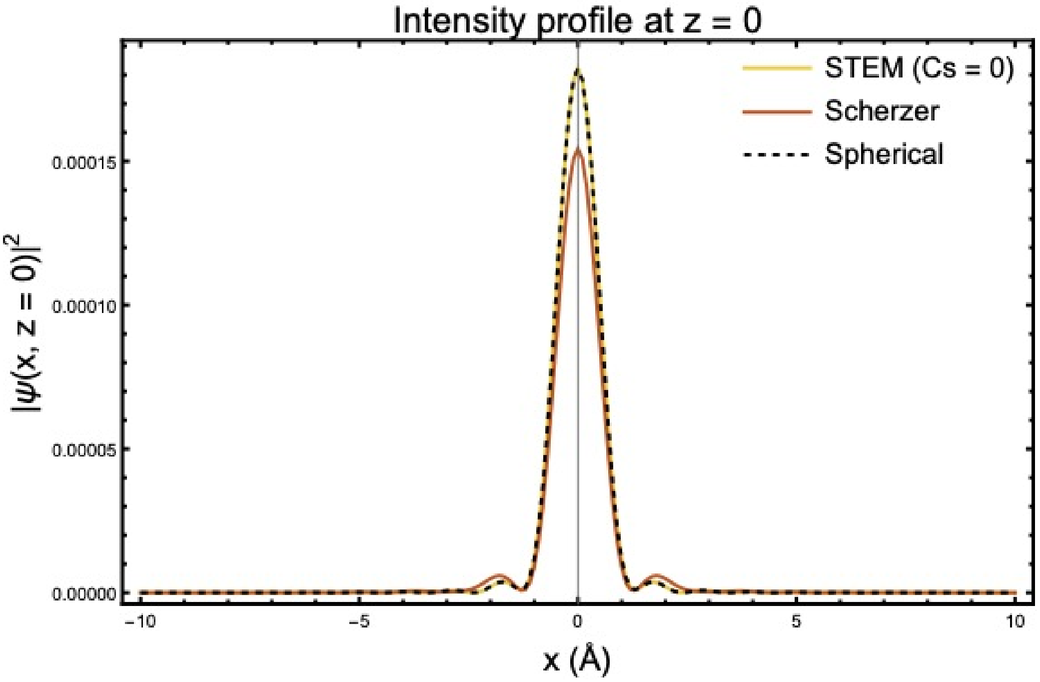

Figure 2.13: Specimen-plane intensity profile $|\psi(x, 0)|^2$ comparing spherical illumination, a defocus-only STEM probe ($C_s = 0$, $\Delta f = -z_s$), and a Scherzer-tuned STEM probe ($C_s = 1 \times 10^7$ Å, $\Delta f_{\mathrm{Sch}} = -447$ Å), all evaluated with the same convergence semi-angle $\alpha = \alpha_{\mathrm{Sch}} = 9.36 \times 10^{-3}$ rad.

Finally, Fig. 2.15 shows the imaginary part of the specimen-plane wavefunction. Under Scherzer conditions, the additional $k_\perp^4$ phase contribution introduced by spherical aberration generates phase structure that cannot be replicated by free-space spherical illumination beyond the quadratic regime, even when the corresponding intensity profiles remain qualitatively similar.

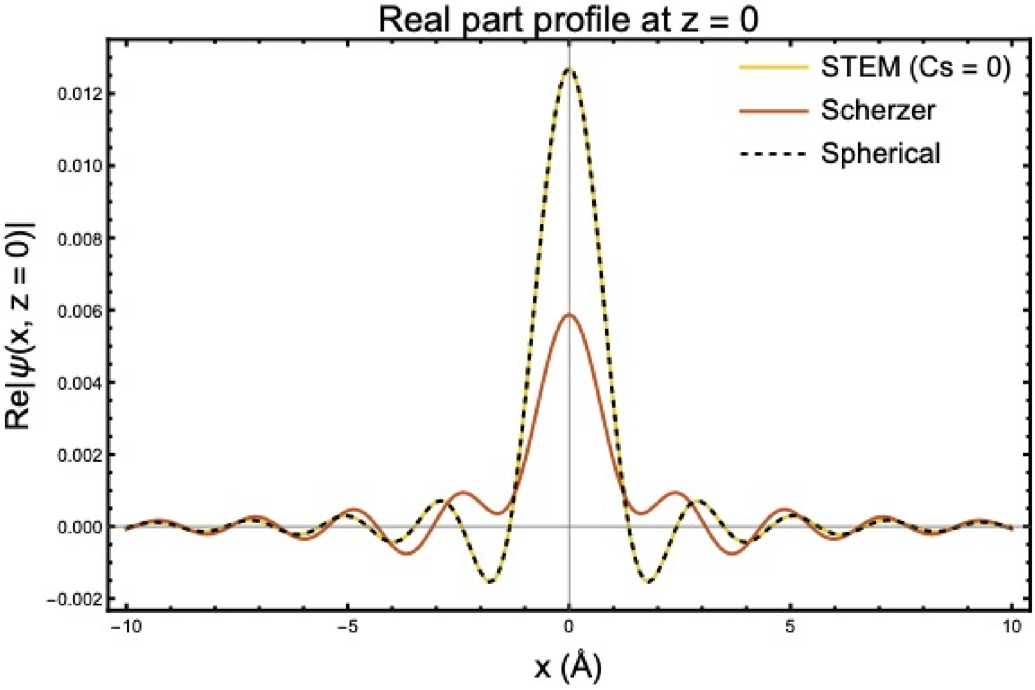

Figure 2.14: Real part of the specimen-plane wavefunction $\Re[\psi(x,0)]$ for spherical illumination and for the two representative STEM probes (same parameters of the previous plots $\alpha = \alpha_{\mathrm{Sch}}$, Δf_{Sch}, C_s).

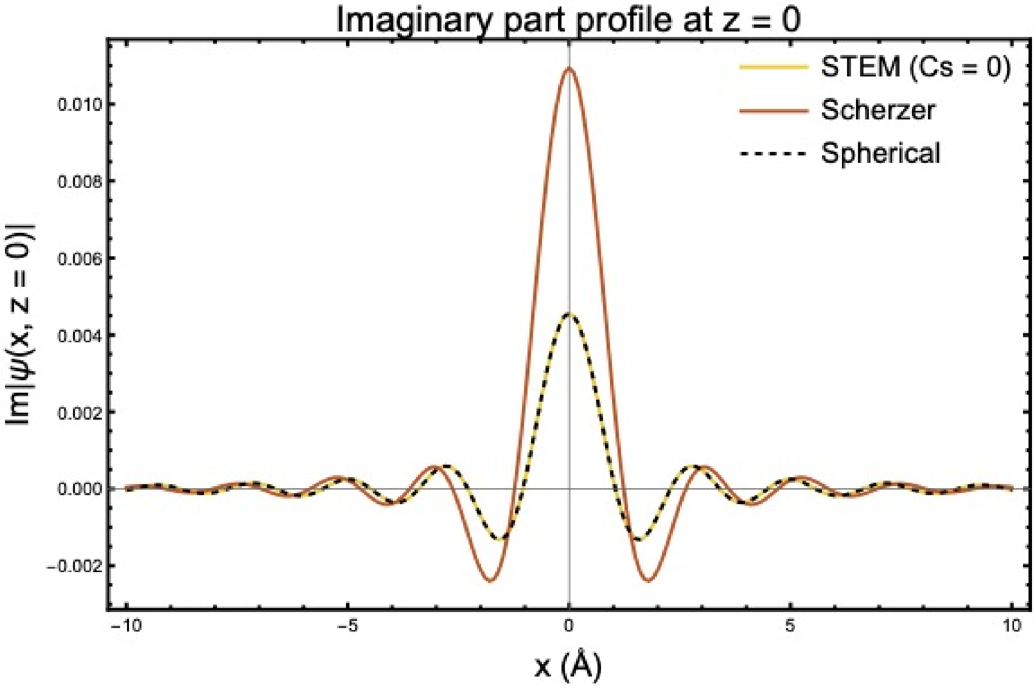

Figure 2.15: Imaginary part of the specimen-plane wavefunction $\Im[\psi(x,0)]$, highlighting the breakdown of the equivalence between spherical illumination and a Scherzer-tuned STEM probe beyond the quadratic phase regime (same parameters of the previous plots $\alpha = \alpha_{\mathrm{Sch}}$, Δf_{Sch}, C_s).

It should be emphasized that the spherical-wave reference adopted here is not intended to reproduce the detailed aperture function of a realistic STEM probe. Rather, it is designed to capture the local phase curvature of the incident wavefront at the specimen plane, which is the quantity directly entering the Born scattering integral for a localized potential.

State-of-the-art electron microscopes are routinely equipped with advanced aberration correctors[4], allowing independent compensation of spherical and higher-order aberrations. Under such conditions, modern STEM probes can be tuned to operate close to a curvature-dominated regime, in which residual aberrations are minimized and the wavefront at the specimen plane is well approximated by a smoothly varying phase profile.

In this light, the use of spherical-wave illumination as a reference model should not be regarded as artificial. Instead, it provides a physically motivated first-order description of the local wavefront curvature experienced by the specimen, onto which controlled aperture-induced and aberration-induced deviations may be systematically reintroduced.

Even in the absence of full aberration correction, operation under Scherzer conditions ensures that the dominant contribution to the probe phase at the specimen plane remains quadratic over a restricted angular range. This justifies the use of spherical-wave illumination as a controlled first-order reference for local scattering, without implying a full equivalence with a realistic STEM probe.

2.5.8 Converging versus diverging waves and phase sensitivity

In an ideal aberration-free electron-optical system, the specimen is illuminated by a *converging* wavefield. A converging spherical wave may be regarded as the time-reversed (complex conjugate) solution of the diverging free-space Green function and therefore differs only by the sign of the propagation phase. Within the present formalism, this distinction amounts to a complex conjugation of the incident phase factor in reciprocal space.

---

[4] In aberration-corrected electron microscopes, the spherical aberration coefficient C_s can be reduced to the micrometer range, typically 1–10 μm (i.e. 10^{-3}–10^{-2} mm), and can be tuned close to zero or even slightly negative depending on the correction settings.

While intensity-based observables are generally insensitive to this sign change, phase-sensitive quantities retain this distinction explicitly. As a consequence, the sign of the wavefront curvature becomes physically relevant when analyzing observables that depend on the complex scattering amplitude, such as phase-resolved or interference-based measurements. This distinction is particularly important when comparing spherical illumination with focused STEM probes, for which the converging nature of the wavefield is fixed by the electron-optical configuration.

2.5.9 Scope and limitations of the present model

For these reasons, the spherical-wave illumination employed in this chapter should not be interpreted as a full simulation of a realistic STEM probe. Rather, it provides a controlled reference model designed to isolate the effects of finite wavefront curvature, source displacement, and symmetry breaking on elastic scattering within the first Born approximation.

Within the paraxial, defocus-dominated regime, and when only the local structure of the incident wavefront at the specimen plane is physically relevant, qualitative connections with focused STEM probes can be established through the effective-curvature mapping discussed above. Outside these limits—most notably in the presence of spherical aberration or for large convergence angles—a quantitative description of STEM scattering necessarily requires the explicit aperture-and-aberration formalism of Eq. (2.39). From this perspective, the spherical-wave model should be understood as a first-order description of the local wavefront curvature experienced by the specimen, rather than as a substitute for a full electron-optical treatment.

2.5.10 Remark on lateral shifts: spherical illumination versus STEM probe

In the present spherical-illumination model, a lateral displacement of the source position $\mathbf{r}_s = (x_s, 0, z_s)$ modifies the geometry of the incident wavefront itself. This operation introduces a genuine transverse phase gradient, breaks azimuthal symmetry at the level of the incident field, and directly enters the Born scattering integral. As a result, non-zero angular momentum components are activated in the elastic scattering amplitude as an intrinsic consequence of the illumination geometry.

By contrast, in a realistic STEM experiment a lateral displacement of the probe at the specimen plane corresponds to a rigid translation of the focused probe during scanning. For an isolated atom, such a shift is equivalent to a change of coordinate origin and does not alter the intrinsic angular structure of the elastic scattering cross section. Mathematically, this operation introduces only a global phase factor in reciprocal space, leaving both the probe curvature and angular spectrum unchanged.

While the intrinsic scattering physics is unaffected by probe translation, the recorded STEM signal does depend on probe position, since the measured intensity reflects the spatial overlap between the probe and the scattering potential during scanning. For this reason, the off-axis configuration considered in the present work should not be interpreted as a probe scan in STEM, but rather as a controlled modification of the incident wavefront geometry. This distinction is essential for isolating curvature- and symmetry-breaking effects in elastic scattering.

2.5.11 Expected effects in inelastic scattering

Although the present chapter is restricted to elastic scattering, the physical mechanisms identified here naturally extend to inelastic processes. In electron energy-loss spectroscopy (EELS), differential cross sections depend on the spatial overlap between the incident illumination and the electronic excitation, as well as on the transferred momentum and on the phase structure of the incoming wavefront.

Within a plane-wave description, translational invariance enforces strict momentum selection rules, and excitation probabilities depend primarily on the magnitude of the transferred momentum. Illumination with finite wavefront curvature breaks this symmetry by introducing a distribution of local incidence directions and relative phases across the interaction region. As a consequence, the inelastic scattering process can no longer be described in terms of a single well-defined momentum transfer.

A natural theoretical framework capturing coherence effects, phase correlations, and multiple momentum-transfer channels in inelastic scattering is provided by the theory of mixed dynamic form factors (MDFF), which extends the conventional dynamic form factor beyond the plane-wave approximation [20, 47, 48]. Within this formalism, the phase structure and spatial coherence of the incident probe explicitly enter the inelastic scattering probability.

As a result, finite-curvature and symmetry-breaking effects are expected to modify inelastic cross sections in several ways: (i) a reduction of excitation probability associated with partial spatial coherence across the interaction region, (ii) a redistribution of spectral weight among different multipolar excitation channels, and (iii) an enhanced sensitivity to localized and non-dipolar excitations, particularly for off-axis or phase-structured illumination.

These effects are anticipated to become especially relevant when the spatial extent of the probe approaches that of the electronic excitation. In this regime, the local phase structure of the incident wavefront plays a role comparable to that of beam energy and angular spread in shaping the measured EELS signal. A full quantitative treatment of inelastic scattering under spherical illumination, including an explicit MDFF-based formulation, is beyond the scope of the present work and will be addressed in future studies.

Chapter 3

Inelastic Scattering and Plasma Formation

3.1 Temporal Evolution of Ionization and Recombination Processes

As discussed in the previous chapter, the screening length λ_{TF} depends explicitly on the local free-electron density n_e. Consequently, as the sample is continuously irradiated by the primary electron beam, progressive ionization of hydrogen atoms increases n_e, thereby modifying λ_{TF} as well as the effective potential experienced by subsequent incident electrons. Quantifying this temporal evolution requires describing how the densities of the various species within the sample change under sustained beam exposure [9, 12].

3.1.1 Density evolution under electron-beam irradiation

Consider a sample composed solely of hydrogen atoms. As the primary electrons interact with the target, a fraction of the atoms undergo excitation, others are ionized, while the rest remain neutral [9, 12]. Under irradiation, the sample is thus characterized by the time-dependent number densities

1. Neutral hydrogen: $n_H(t) = N_H/V$, the number of neutral H atoms per unit volume;
2. Proton density: $n_p(t) = N_p/V$, the number of ionized hydrogen nuclei (protons) per unit volume;
3. Free-electron density: $n_e(t) = N_e/V$, the number of unbound electrons per unit volume.

For a hydrogen-only system, each ionization event produces exactly one proton and one free electron. Here, ionization is understood as the promotion of an electron from a bound atomic state into the continuum of the *irradiated sample*, rather than into the vacuum. In other words, the zero of energy is taken inside the material, and the ejected electron remains available for subsequent recombination processes. Emission of secondary electrons into vacuum is neglected in the present model.

Therefore,

$$n_e(t) = n_p(t) \equiv n(t). \tag{3.1}$$

Since the number of hydrogen nuclei is conserved, neutral and ionized atoms satisfy

$$n_H(t) + n(t) = n_H(0) \equiv n_H^0. \tag{3.2}$$

Atoms are thus redistributed between neutral and ionized states, but their total number remains constant.

Besides ionization, recombination must also be included in the balance: a free electron may recombine with a proton, forming a neutral atom. The two competing processes are therefore

- **Ionization**, driven by collisions between primary beam electrons and target atoms;
- **Recombination**, driven by electron–ion encounters inside the sample.

The *ionization rate* per unit volume and time is

$$G = \sigma_{\text{ion}}\, \Phi\, n_H, \tag{3.3}$$

where σ_{ion} is the total ionization cross section per atom, and

$$\Phi = \frac{J}{e} = \frac{I}{eA}$$

is the incident electron flux, i.e. the number of primary electrons crossing a unit area per unit time.

It is important to underline that the source term G represents the *net* generation rate of free carriers under electron irradiation. While in an isolated-atom picture this can be associated with single-electron ionization events, in *condensed matter* the dominant inelastic energy-loss channel of fast electrons often excites *collective* modes (plasmons), which subsequently decay into electron–hole pairs and secondary-electron cascades. Therefore, throughout this chapter σ_{ion} should be understood as an *effective carrier-generation cross section* (or, equivalently, an effective yield per incident electron) that may implicitly include plasmon excitation and decay processes, rather than a microscopic single-channel ionization cross section. This distinction is discussed, for example, in the plasmon-based description of electron–hole pair production introduced by Rothwarf [49], and in later analyses of plasmon decay into single-particle excitations [50].

The *recombination rate* is given by

$$R = \alpha_{\text{rec}}\, n_p\, n_e = \alpha_{\text{rec}}\, n^2, \tag{3.4}$$

where α_{rec} is the recombination coefficient (see [51]). The time evolution of the densities becomes

$$\frac{\mathrm{d}n_H}{\mathrm{d}t} = -G + R = -\sigma_{\text{ion}}\Phi n_H + \alpha_{\text{rec}} n^2, \tag{3.5}$$

$$\frac{\mathrm{d}n_p}{\mathrm{d}t} = +G - R = \sigma_{\text{ion}}\Phi n_H - \alpha_{\text{rec}} n^2, \tag{3.6}$$

$$\frac{\mathrm{d}n_e}{\mathrm{d}t} = +G - R = \sigma_{\text{ion}}\Phi n_H - \alpha_{\text{rec}} n^2. \tag{3.7}$$

Using $n_e = n_p = n$ and $n_H = n_H^0 - n$, the system reduces to a single nonlinear differential equation:

$$\boxed{\frac{\mathrm{d}n}{\mathrm{d}t} = \sigma_{\text{ion}}\Phi\left(n_H^0 - n\right) - \alpha_{\text{rec}} n^2} \tag{3.8}$$

with initial condition $n(0) = 0$ (initially neutral sample).

Equation (3.8) is a Riccati-type equation of the form

$$\dot{n} = A - B\, n - C\, n^2, \qquad \text{with} \qquad A = \sigma_{\text{ion}}\Phi n_H^0, \quad B = \sigma_{\text{ion}}\Phi, \quad C = \alpha_{\text{rec}}.$$

3.1.2 Recombination mechanisms

The effective recombination coefficient α_{rec} depends on the electron temperature T_e, the electron density n_e, and on the microscopic channel involved. In the following we report the standard *scaling laws* used in plasma physics to highlight the parametric dependence; accurate rate coefficients for specific charge states require tabulated fits (e.g. the NRL Plasma Formulary and dedicated atomic-physics references) [52, 53, 54].

The dominant recombination mechanisms are:

1. **Radiative recombination (RR)**

   $$Z^+ + e^- \to Z + h\nu, \qquad \alpha_{\mathrm{RR}}(T_e) \propto T_e^{-1/2} \quad [\mathrm{m}^3/\mathrm{s}],$$

   typical of low-temperature and low-density plasmas [52].

2. **Three-body recombination (TBR)**

   $$Z^+ + e^- + e^- \to Z + e^-, \qquad \alpha_{\mathrm{TBR}}(T_e) \propto n_e T_e^{-9/2} \quad [\mathrm{m}^6/\mathrm{s}],$$

   relevant in high-density and low-temperature conditions [52, 55, 56].

3. **Dielectronic recombination (DR)**

   $$Z^+ + e^- \to (Z^{**}) \to Z + h\nu, \qquad \alpha_{\mathrm{DR}}(T_e) \sim \sum_j C_j T_e^{-3/2} \exp(-E_j/k_B T_e) \quad [\mathrm{m}^3/\mathrm{s}],$$

   where Z^{**} is an autoionizing doubly excited state that can stabilize radiatively [53, 54].

Dimensional consistency requires

$$[\alpha_{\mathrm{RR}}] = [\alpha_{\mathrm{DR}}] = L^3 T^{-1}, \qquad [\alpha_{\mathrm{TBR}}] = L^6 T^{-1}.$$

3.1.3 Analytical solution of the Riccati equation

Equation (3.8) can be solved analytically. Introducing the auxiliary quantities

$$n_\pm = \frac{-B \pm \sqrt{B^2 + 4AC}}{2C},$$

the solution reads

$$n(t) = n_+ \frac{1 - e^{-C(n_+ - n_-)t}}{1 - \dfrac{n_+}{n_-} e^{-C(n_+ - n_-)t}}. \tag{3.9}$$

The initial condition $n(0) = 0$ is readily verified by taking the limit $t \to 0$. Since $e^{-C(n_+ - n_-)t} \to 1$, the numerator vanishes while the denominator remains finite for $n_+ \neq n_-$, yielding $n(0) = 0$.

It is convenient to rewrite the result by introducing the dimensionless parameter

$$\varrho = \frac{\sigma_{\mathrm{ion}} \Phi}{\alpha_{\mathrm{rec}}},$$

which measures the relative importance of ionization to recombination. After some algebra, and defining

$$\varsigma = \sqrt{1 + \frac{4n_H^0}{\varrho}},$$

one obtains the compact expression

$$\boxed{n(t) = \frac{\varrho}{2}\left(-1+\varsigma\right) \frac{1 - e^{-\sigma_{\mathrm{ion}}\,\Phi\,\varsigma\,t}}{1 - \dfrac{1-\varsigma}{1+\varsigma} e^{-\sigma_{\mathrm{ion}}\,\Phi\,\varsigma\,t}}.} \tag{3.10}$$

The initial condition is again recovered by taking the limit $t \to 0$, for which the exponential term tends to unity and the numerator vanishes, ensuring $n(0) = 0$. This solution describes the build-up of a transient plasma inside the irradiated volume, driven by the competition between beam-induced ionization and recombination processes.

Figure 3.1 illustrates how the interplay between ionization and recombination shapes the transient plasma dynamics under different physical conditions.

3.1.4 Steady-state and stability analysis

The steady state of the system is obtained by setting $\dot{n} = 0$ in Eq. (3.8), which yields the balance condition

$$\sigma_{\mathrm{ion}}\Phi(n_H^0 - n_{\mathrm{eq}}) = \alpha_{\mathrm{rec}} n_{\mathrm{eq}}^2.$$

Solving the resulting quadratic equation leads to the physically meaningful positive root

$$n_{\mathrm{eq}} = \frac{\varrho}{2}\left(-1+\varsigma\right), \tag{3.11}$$

which represents the steady-state free-carrier density established under continuous irradiation.

The stability of this equilibrium can be assessed by linearizing Eq. (3.8) around n_{eq}, writing $n(t) = n_{\mathrm{eq}} + \Delta n(t)$. To first order in Δn, one obtains

$$\frac{\mathrm{d}(\Delta n)}{\mathrm{d}t} \simeq -(B + 2Cn_{\mathrm{eq}})\,\Delta n,$$

showing that small perturbations decay exponentially in time. Indeed, the derivative of the rate function evaluated at the fixed point is

$$f'(n_{\mathrm{eq}}) = -B - 2Cn_{\mathrm{eq}} < 0,$$

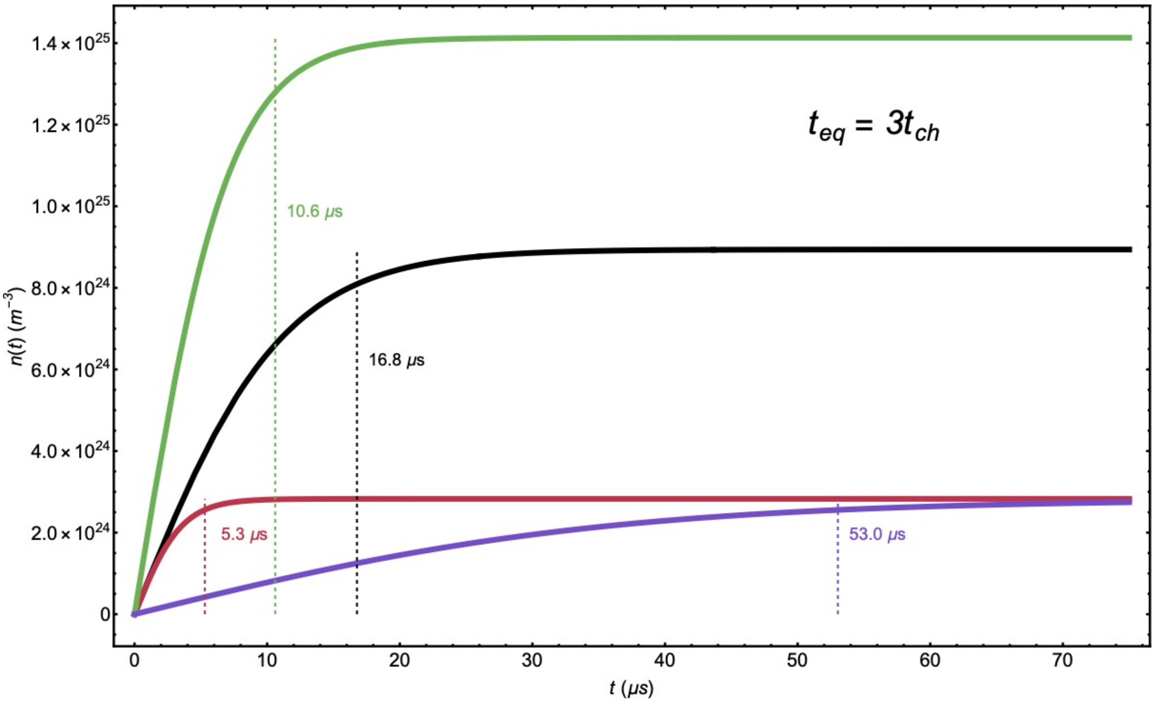

Figure 3.1: Time evolution of the free-electron density $n(t)$ obtained from Eq. (3.10). The four curves correspond to: (black) reference case $\{\sigma_{\text{ion}} = 10^{-20}\,\text{m}^2$, $n_H^0 = 10^{28}\,\text{m}^{-3}$, $\Phi = 8 \times 10^{21}\,\text{m}^{-2}\text{s}^{-1}$, $\alpha_{\text{rec}} = 10^{-20}\,\text{m}^3/\text{s}\}$; (red) higher recombination $\alpha_{\text{rec}} = 10^{-19}\,\text{m}^3/\text{s}$; (green) higher flux $\Phi = 2 \times 10^{22}\,\text{m}^{-2}\text{s}^{-1}$; (purple) lower initial density $n_H^0 = 10^{27}\,\text{m}^{-3}$. Increasing the flux accelerates ionization and increases the equilibrium density, while stronger recombination suppresses it. A reduced initial neutral density lowers both the growth rate and the steady-state value. Dashed vertical lines mark the equilibration time $t_{\text{eq}} \equiv 3\,t_{\text{ch}}$, as defined in Eq. (3.15), with the corresponding numerical values reported on the plot. For the reference case (black curve), the dashed vertical line marks an equilibration time of $t_{\text{eq}} \simeq 16.8\,\mu\text{s}$, which is consistent with the analytical estimate $t_{\text{eq}} \approx 17\,\mu\text{s}$ obtained for the same parameters.

demonstrating that the steady state is linearly stable for all physically admissible parameter values.

The global dynamical behavior is conveniently visualized by means of the phase portrait of the rate equation. Figure 3.2 shows the normalized time derivative $(1/n_H^0)\,\text{d}n/\text{d}t$ as a function of the normalized carrier density n/n_H^0 for a representative set of TEM parameters.

The phase portrait, defined here as the representation of the one-dimensional dynamical system in the phase space spanned by the carrier density n and its time derivative $\dot{n} = G - R$, is given by the plot of the net carrier generation rate $(G - R)$ as a function of n. It exhibits a single zero crossing corresponding to n_{eq}, with a negative

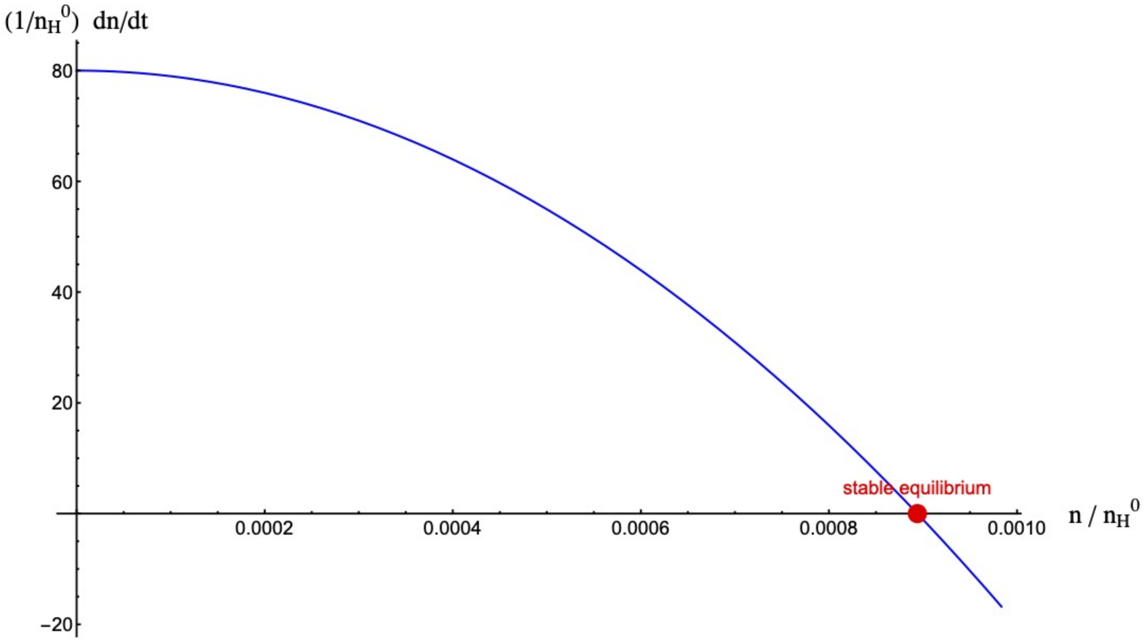

Figure 3.2: Phase portrait of the normalized rate equation, showing $(1/n_H^0)\,\mathrm{d}n/\mathrm{d}t$ as a function of the normalized carrier density n/n_H^0. The system exhibits a single fixed point corresponding to the steady-state carrier density n_{eq}. The negative slope at the zero crossing indicates that the equilibrium is a stable attractor, ensuring convergence toward equilibrium for any physically admissible initial condition.

slope at the intersection. For carrier densities below n_{eq}, ionization dominates and the carrier density increases, whereas for densities above n_{eq} recombination prevails and drives the system back toward equilibrium. This confirms that the steady state is globally stable and that the carrier density monotonically converges toward n_{eq} under continuous irradiation, independently of the initial condition.

3.1.5 Implications for Thomas–Fermi screening and elastic scattering

The steady-state carrier density n_{eq} obtained above provides a direct quantitative estimate of the screening length λ_{TF} introduced at the end of the first chapter. In the degenerate Thomas–Fermi model,

$$k_{\mathrm{TF}}^2 = \frac{3n_e e^2}{2\varepsilon_0 E_{\mathrm{F}}}, \qquad E_{\mathrm{F}} = \frac{\hbar^2}{2m}(3\pi^2 n_e)^{2/3}, \qquad \lambda_{\mathrm{TF}} = \frac{1}{k_{\mathrm{TF}}},$$

so that $k_{\mathrm{TF}} \propto n_e^{1/6}$ and therefore

$$\lambda_{\mathrm{TF}} \propto n_e^{-1/6}. \tag{3.12}$$

This weak scaling implies that even large variations of n_e translate into comparatively modest changes of λ_{TF}.

In the present hydrogenic model, charge neutrality gives $n_e(t) = n_p(t)$ and the stationary ionization fraction is

$$x \equiv \frac{n_{\mathrm{eq}}}{n_H^0}.$$

For the representative TEM parameter set used in Fig. 3.1, the steady state corresponds to $x \sim 10^{-3}$–2×10^{-3}, i.e. approximately 1–2 ionized atoms per 10^3 hydrogen atoms. This result provides a simple and intuitive physical picture of the steady state: under continuous TEM irradiation, the sample remains largely neutral, with only a very small fraction of atoms ionized at any given time, while this tiny ionized population is nevertheless sufficient to induce atomic-scale screening effects.

With $n_H^0 \simeq 10^{28}\,\mathrm{m}^{-3}$, this yields

$$n_e^{\mathrm{eq}} = n_{\mathrm{eq}} \simeq x\, n_H^0 \sim (1\text{–}2) \times 10^{25}\,\mathrm{m}^{-3}.$$

Inserting this density in the Thomas–Fermi expressions gives a screening length of order

$$\lambda_{\mathrm{TF}}(n_e^{\mathrm{eq}}) \simeq (0.22\text{–}0.25)\,\mathrm{nm} \simeq (4.2\text{–}4.7)\,a_0, \tag{3.13}$$

i.e. screening on sub-nanometer length scales comparable to atomic dimensions.

At early irradiation times the sample is initially neutral and the free-carrier density is essentially negligible. In that limit, carrier-mediated screening (Debye/Thomas–Fermi) formally yields $\lambda \to \infty$, reflecting the absence of an electron gas and therefore the absence of free-carrier screening. The Yukawa/Thomas–Fermi description becomes meaningful once a finite n_e has been generated. Because $\lambda_{\mathrm{TF}} \propto n_e^{-1/6}$, even an increase of n_e by several orders of magnitude reduces λ_{TF} only by a factor of a few. For instance, taking a conservative onset density $n_{e,\min} \sim 10^{22}$–$10^{23}\,\mathrm{m}^{-3}$ (one to three orders of magnitude below the stationary value) gives $\lambda_{\mathrm{TF}}(n_{e,\min}) \sim 0.5$–$0.8\,\mathrm{nm}$, so that the overall evolution from early times to steady state is typically a reduction of λ_{TF} by a factor ~ 2–4 rather than by orders of magnitude.

The screening length enters nonlinearly in the Yukawa scattering amplitude derived in the previous chapter,

$$f(K) = \frac{2}{a_0}\frac{1}{K^2 + 1/\lambda_{\mathrm{TF}}^2}, \qquad \frac{d\sigma}{d\Omega} = |f(K)|^2 \propto \frac{1}{(K^2 + 1/\lambda_{\mathrm{TF}}^2)^2}.$$

A convenient measure of the screening effect is the ratio to the formally unscreened Coulomb-like behavior ($\lambda_{\rm TF} \to \infty$), which scales as $1/K^4$:

$$\mathcal{R}(K) \equiv \frac{(\mathrm{d}\sigma/\mathrm{d}\Omega)_{\rm screened}}{(\mathrm{d}\sigma/\mathrm{d}\Omega)_{\rm unscreened}} = \left(\frac{K^2}{K^2 + 1/\lambda_{\rm TF}^2}\right)^2 . \tag{3.14}$$

For $\lambda_{\rm TF} \simeq 0.22$–$0.25\,\mathrm{nm}$ one has $1/\lambda_{\rm TF} \simeq 0.40$–$0.45\,\mathrm{\AA}^{-1}$. Thus, screening primarily affects very small momentum transfers ($K \lesssim 1/\lambda_{\rm TF}$), i.e. the forward-scattering regime, while the modification becomes modest at larger K. For example, using $1/\lambda_{\rm TF} = 0.45\,\mathrm{\AA}^{-1}$,

$$K = 1\,\mathring{A}^{-1}: \;\; \mathcal{R} \simeq \left(\frac{1}{1+0.45^2}\right)^2 \approx 0.69, \qquad K = 2\,\mathring{A}^{-1}: \;\; \mathcal{R} \simeq \left(\frac{4}{4+0.45^2}\right)^2 \approx 0.91.$$

Therefore, stationary ionization levels of order $x \sim 10^{-3}$ correspond to atomic-scale screening lengths and can significantly suppress very-small-angle elastic scattering, while altering medium/high-K scattering only at the level of a few to a few tens of percent, depending on the angular acceptance of the measurement.

3.1.6 Characteristic time in TEM conditions

The linearization of Eq. (3.8) around the steady-state solution $n_{\rm eq}$, introduced in the previous section to assess stability, also provides direct access to the characteristic timescale governing the asymptotic approach to equilibrium.

Although Eq. (3.8) admits an exact analytical solution, the timescale controlling the relaxation toward the steady state is not immediately transparent from the full nonlinear expression. Instead, it naturally emerges from the linearized dynamics in the vicinity of $n_{\rm eq}$.

Writing again

$$n(t) = n_{\rm eq} + \Delta n(t), \qquad |\Delta n| \ll n_{\rm eq},$$

the first-order expansion of the rate equation yields

$$\frac{\mathrm{d}(\Delta n)}{\mathrm{d}t} \simeq -\left(\sigma_{\rm ion}\Phi + 2\alpha_{\rm rec} n_{\rm eq}\right)\Delta n.$$

This linear equation describes the late-time dynamics, once the carrier density is sufficiently close to equilibrium. In this regime, the nonlinear ionization–recombination balance effectively reduces to a simple exponential relaxation toward $n_{\rm eq}$.

The associated characteristic time

$$t_{\mathrm{ch}} = (\sigma_{\mathrm{ion}}\Phi + 2\alpha_{\mathrm{rec}} n_{\mathrm{eq}})^{-1}$$

therefore controls the asymptotic convergence to the steady state and provides a natural timescale for comparison with experimentally relevant beam modulation times, such as pixel dwell times or beam blanking intervals.

Importantly, the linearized description does not replace the full Riccati equation, which governs the global temporal evolution. Rather, the two formulations play complementary roles: the nonlinear equation determines the steady-state density and the full transient behavior, while the linearized form isolates the local relaxation dynamics and the characteristic time, t_{ch}, which describes how rapidly the system approaches steady state.

Then, continuing with the linearization already performed in Eq. (3.8), we have

$$\Delta n(t) = \Delta n(0)\, e^{-t/t_{\mathrm{ch}}}, \qquad t_{\mathrm{ch}} = \frac{1}{\sigma_{\mathrm{ion}}\Phi + 2\alpha_{\mathrm{rec}} n_{\mathrm{eq}}}. \tag{3.15}$$

Under typical TEM operating conditions, the beam current lies in the range 10 pA $\lesssim I \lesssim$ 1 nA, depending on the measurement mode and damage constraints. Currents in the microampere range are not considered here and would in practice lie far outside standard TEM and STEM operation. In the following, a representative upper–bound value $I \simeq 1$ nA is adopted to provide a conservative estimate of the characteristic relaxation time.

For a probe diameter $d \simeq 1\,\mu$m, the illuminated area is $A = 7.85 \times 10^{-13}\,\mathrm{m}^2$. Using $n_H^0 \simeq 10^{28}\,\mathrm{m}^{-3}$, $\sigma_{\mathrm{ion}} \simeq 10^{-20}\,\mathrm{m}^2$, and $\alpha_{\mathrm{rec}} \simeq 10^{-20}\,\mathrm{m}^3/\mathrm{s}$, the incident flux becomes

$$\Phi = \frac{I}{eA} \simeq 8 \times 10^{21}\,\mathrm{m}^{-2}\,\mathrm{s}^{-1}.$$

The equilibrium time is therefore

$$t_{\mathrm{eq}} \approx 3t_{\mathrm{ch}} = \frac{3}{\sigma_{\mathrm{ion}}\Phi + 2\alpha_{\mathrm{rec}} n_{\mathrm{eq}}} \simeq 1.7 \times 10^{-5}\,\mathrm{s} \quad (\text{approximately } 17\ \mu\mathrm{s}).$$

Since t_{ch}^{-1} depends linearly on the incident flux Φ, the equilibrium time scales inversely with the beam current and can therefore be readily rescaled to lower, damage–free operating conditions.

This value, highlighted in fig. 3.1 and corresponding to the black line, provides an order-of-magnitude estimate for the timescale over which a thin irradiated hydrogenic sample reaches quasi-equilibrium under typical TEM operating conditions. It constitutes the temporal foundation for the full spatial analysis carried out in the next chapter, where diffusion, drift, and space-charge effects are coupled self-consistently through the Poisson equation.

For the reference parameters, the equilibrium time extracted from Eq. (3.8) yields $t_{\rm eq} \approx 17\ \mu$s, which is fully consistent with the behavior observed in Fig. 3.1, where the free-electron density approaches its steady-state value within the first $\sim 20\ \mu$s.

The dependence of the equilibrium time on the ionization cross section is shown in Fig. 3.3.

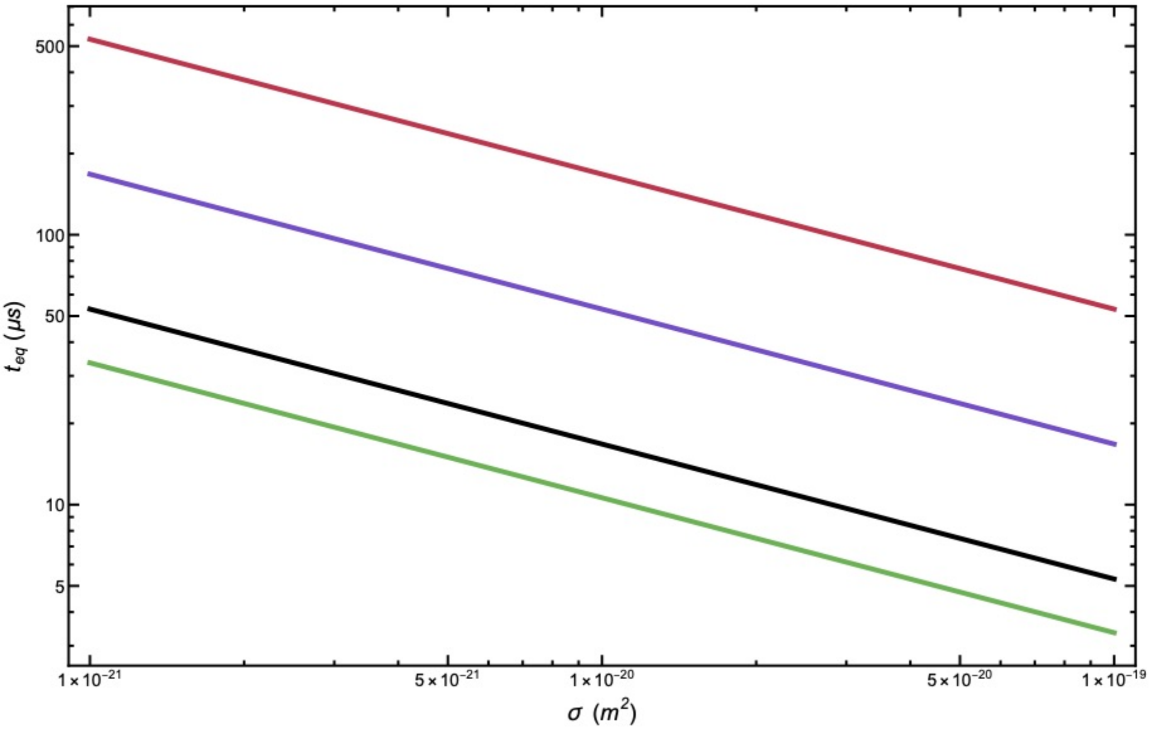

Figure 3.3: Equilibrium time $t_{\rm eq}$ as a function of the ionization cross section $\sigma_{\rm ion}$, shown in a double–logarithmic scale. Four parameter sets are represented: (black) reference case $\{\Phi = 8 \times 10^{21}\,{\rm m^{-2}s^{-1}}$, $\alpha_{\rm rec} = 10^{-20}\,{\rm m^3/s}$, $n_H^0 = 10^{28}\,{\rm m^{-3}}\}$; (red) higher recombination $\alpha_{\rm rec} = 10^{-19}\,{\rm m^3/s}$; (green) higher flux $\Phi = 2 \times 10^{22}\,{\rm m^{-2}s^{-1}}$; (purple) lower initial density $n_H^0 = 10^{27}\,{\rm m^{-3}}$. The log–log representation highlights a linear decrease of $t_{\rm eq}$ with increasing $\sigma_{\rm ion}$, illustrating the strong sensitivity of the relaxation dynamics to the ionization probability.

This plot illustrates how $t_{\rm eq}$ varies across several orders of magnitude of $\sigma_{\rm ion}$ and how flux, recombination efficiency, and initial density affect the overall relaxation dynamics.

3.2 Beam Switch-Off and Plasma Relaxation

In STEM, the temporal modulation of the electron beam is naturally characterized by a pixel dwell time. In conventional TEM, although no pixel-by-pixel scanning is involved, the beam is nevertheless temporally interrupted due to electronic beam blanking, finite exposure times, and acquisition pauses. Throughout this work, the term *beam switch-off time* is therefore used as a general descriptor of the interruption of electron irradiation, applicable to both TEM and STEM configurations.

The analysis presented so far describes the build-up of a transient plasma under continuous electron-beam irradiation. A complementary and physically crucial question concerns the *relaxation dynamics* of the system once the external excitation is removed.

In a TEM experiment, the illumination is never truly permanent: beam blanking, scanning strategies, or pulsed operation routinely interrupt the irradiation. Understanding how fast an irradiated sample returns to its initial electrical state is therefore essential for assessing cumulative charging effects, memory phenomena, and the validity of steady-state assumptions.

In the present section, we investigate the temporal evolution of the system after the electron beam is switched off, under the same idealized assumptions adopted previously:

- homogeneous illumination before switch-off;
- no spatial transport (no diffusion or drift);
- local charge neutrality;
- recombination governed by a single effective coefficient α_{rec}.

We emphasize that the present relaxation model neglects spatial transport (diffusion and drift) and therefore applies most directly to conditions of approximately uniform (parallel) illumination, as commonly encountered in TEM. For a focused

STEM probe, strong lateral gradients in the carrier density are expected, and diffusion can substantially modify the apparent relaxation dynamics by redistributing carriers during and after irradiation. In that case, the effective relaxation time may differ from the purely local estimate derived here and must be obtained from the coupled drift–diffusion–recombination equations discussed in the next chapter.

Unlike the purely hydrogenic case discussed earlier, we now explicitly allow for the presence of an intrinsic carrier density when appropriate.

3.2.1 Total and excess carrier densities

In real materials, a finite carrier density may exist even in the absence of irradiation. It is therefore convenient to decompose the total free-carrier density as

$$n(t) = n_i + \Delta n(t), \tag{3.16}$$

where n_i denotes the intrinsic equilibrium carrier density and $\Delta n(t)$ represents the excess population generated by the electron beam.

The hydrogenic model discussed in the previous sections corresponds to the limiting case $n_i = 0$, appropriate for initially neutral systems such as gases or wide-bandgap insulators.

3.2.2 Density evolution after beam switch-off

Let $t = t_0$ denote the instant at which the electron beam is switched off. The switch-off time is chosen such that the system has already reached the steady state established under continuous irradiation. In practice, we set

$$t_0 = 3\,t_{\mathrm{ch}},$$

where t_{ch} is the characteristic time defined in eq. (3.15). For $t > t_0$, the incident flux vanishes,

$$\Phi(t) = 0,$$

and ionization processes immediately cease.

The subsequent evolution is governed solely by recombination. Starting from the general rate equation,

$$\frac{\mathrm{d}n}{\mathrm{d}t} = -\alpha_{\mathrm{rec}}\left(n^2 - n_i^2\right),$$

and using $n = n_i + \Delta n$, one obtains

$$\boxed{\frac{\mathrm{d}(\Delta n)}{\mathrm{d}t} = -\alpha_{\mathrm{rec}}\left(\Delta n^2 + 2n_i\Delta n\right).} \tag{3.17}$$

The initial condition is

$$\Delta n(t_0) = \Delta n_{\mathrm{eq}},$$

where Δn_{eq} is the excess steady-state density reached under irradiation. This choice reflects the fact that the transient plasma is fully developed at $t = t_0$, so that the subsequent dynamics probe the intrinsic relaxation of the system in the absence of external excitation.

3.2.3 Analytical solution of the relaxation phase

Equation (3.17) is separable and admits an exact analytical solution. Integrating from t_0 to t yields

$$\int_{\Delta n_{\mathrm{eq}}}^{\Delta n(t)} \frac{\mathrm{d}(\Delta n)}{\Delta n(\Delta n + 2n_i)} = -\alpha_{\mathrm{rec}} \int_{t_0}^{t} \mathrm{d}t.$$

After straightforward algebra, the solution can be written as

$$\boxed{\Delta n(t) = \frac{2n_i\Delta n_{\mathrm{eq}}\, e^{-2\alpha_{\mathrm{rec}} n_i (t-t_0)}}{2n_i + \Delta n_{\mathrm{eq}}\left[1 - e^{-2\alpha_{\mathrm{rec}} n_i (t-t_0)}\right]}.} \tag{3.18}$$

Two limiting regimes naturally emerge:

- for $n_i \to 0$, the decay becomes algebraic, $\Delta n(t) = \Delta n_{\mathrm{eq}}/\big[1 + \alpha_{\mathrm{rec}}\Delta n_{\mathrm{eq}}(t - t_0)\big]$, recovering the hydrogenic result;
- for $n_i \gg \Delta n$, the decay is exponential (doped semiconductor), $\Delta n(t) \propto e^{-2\alpha_{\mathrm{rec}} n_i (t-t_0)}$.

3.2.4 Characteristic relaxation time

The characteristic relaxation time critically depends on the presence of intrinsic carriers. Linearizing Eq. (3.17) for $\Delta n \ll n_i$ yields

$$\frac{\mathrm{d}(\Delta n)}{\mathrm{d}t} \simeq -2\alpha_{\mathrm{rec}} n_i \Delta n,$$

leading to an exponential relaxation characterized by the time constant

$$\boxed{t_{\mathrm{rel}} = \frac{1}{2\alpha_{\mathrm{rec}} n_i}.} \tag{3.19}$$

In the hydrogenic or insulating limit ($n_i = 0$), no intrinsic relaxation timescale exists and the decay of the excess carrier density becomes algebraic, with an effective relaxation time

$$t_{\mathrm{rel}} \sim \frac{1}{\alpha_{\mathrm{rec}} \Delta n_{\mathrm{eq}}}.$$

This qualitative difference reflects the absence of an intrinsic carrier reservoir capable of rapidly neutralizing the beam-induced charge population.

3.2.5 Characteristic time versus relaxation time

The characteristic time controlling the asymptotic approach to the steady state under continuous electron-beam irradiation is again

$$t_{\mathrm{ch}} = \frac{1}{\sigma_{\mathrm{ion}} \Phi + 2\alpha_{\mathrm{rec}}(n_i + \Delta n_{\mathrm{eq}})}. \tag{3.20}$$

This expression does not introduce a new timescale, but represents the direct generalization of the characteristic time t_{ch} previously derived for the hydrogenic case, extended to materials with a finite intrinsic carrier density. This timescale governs the decay of small deviations from the steady state. Accordingly, after a time $t \gtrsim 3\, t_{\mathrm{ch}}$ the carrier density is within a few percent of n_{eq}.

A fundamental dynamical asymmetry therefore emerges between the two processes:

- charging is externally driven by the incident electron flux and is typically fast;
- relaxation is internally controlled by recombination processes and is strongly material-dependent.

This asymmetry is illustrated in Fig. 3.4, which shows the temporal evolution of the carrier density during continuous irradiation and after beam switch-off.

While ionization drives a rapid increase of $n(t)$ toward a transient value, the subsequent relaxation proceeds more slowly once the external excitation is removed.

In systems with negligible intrinsic carrier density ($n_i \simeq 0$), one generally finds

$$t_{\mathrm{ch}} \ll t_{\mathrm{rel}},$$

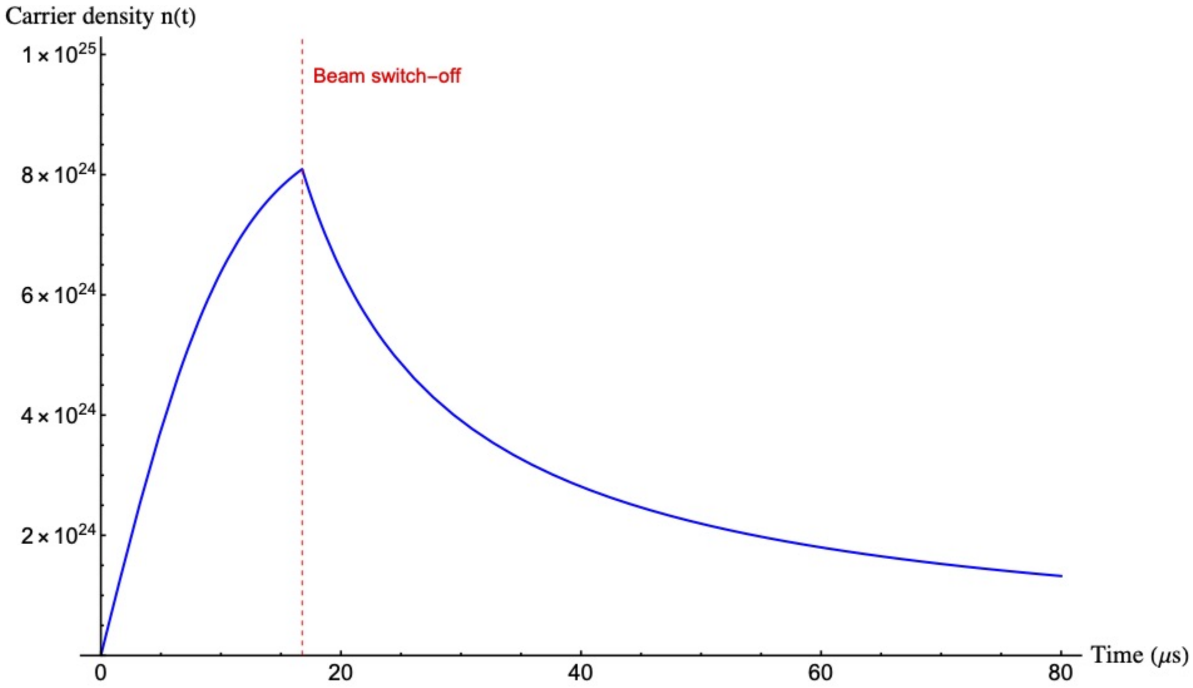

Figure 3.4: Time evolution of the carrier density $n(t)$ under continuous electron-beam irradiation and after beam switch-off. During the irradiation phase, ionization processes driven by the incident electron flux cause a rapid increase of the carrier density toward the steady-state value n_{eq}. The system is allowed to fully reach this equilibrium before the beam is switched off at time $t_0 = 3\,t_{\text{ch}}$ (vertical dashed line). For $t > t_0$, the external excitation is removed and ionization ceases, so that the subsequent dynamics are governed solely by recombination. The continuity of $n(t)$ at t_0 reflects particle conservation, while the change in slope marks the transition from externally driven charging dynamics to intrinsic plasma relaxation.

leading to pronounced memory effects and long-lived excess carrier populations. In contrast, materials with large n_i exhibit rapid neutralization after beam switch-off, resulting in a fast recovery of the equilibrium electrical state.

3.3 Extension to Real Materials

The hydrogenic model discussed so far provides a minimal and analytically tractable framework to describe beam-induced plasma formation and relaxation. Real materials, however, exhibit profoundly different electronic properties, which strongly affect both the magnitude of the induced carrier density and the associated temporal dynamics.

In this section, the formalism developed above is applied to three broad classes of materials relevant to transmission electron microscopy: insulators, semiconductors, and metals. For each class, characteristic carrier densities, recombination coefficients, and relaxation times are estimated and compared. These estimates demonstrate that the temporal response of a material to beam-induced ionization spans more than fifteen orders of magnitude, depending primarily on the intrinsic carrier density.

The intrinsic carrier densities and effective recombination coefficients used here are standard textbook values taken from semiconductor transport theory and solid-state physics literature [57, 58, 59].

3.3.1 Insulators: Silicon Oxide

Wide-bandgap insulators such as silicon oxide are characterized by an extremely low intrinsic carrier density. At room temperature, the intrinsic free-electron density is effectively negligible,

$$n_i \approx 0.$$

Beam-induced ionization generates electron–hole pairs that are not efficiently neutralized by intrinsic carriers. Typical effective recombination coefficients in amorphous SiO_2 are of order

$$\alpha_{\mathrm{rec}} \sim 10^{-22}\text{–}10^{-20}\,\mathrm{m}^3/\mathrm{s},$$

depending on defect density and local structure, as reported in experimental and modelling studies of beam-induced charging and carrier relaxation in amorphous oxides under electron irradiation [60].

For a representative excess carrier density

$$\Delta n_{\mathrm{eq}} \sim 10^{20}\text{–}10^{22}\,\mathrm{m}^{-3},$$

the characteristic relaxation time in the absence of intrinsic carriers follows

$$t_{\mathrm{rel}} \sim \frac{1}{\alpha_{\mathrm{rec}}\Delta n_{\mathrm{eq}}} \sim 10^{-3}\text{–}10^{2}\,\mathrm{s}.$$

This extremely broad range reflects the strong sensitivity of insulators to microscopic trapping and defect-assisted recombination. As a result, insulating samples may retain a substantial fraction of the beam-induced charge long after the illumination has ceased. This explains the well-known tendency of oxides to exhibit persistent charging, beam deflection, and imaging instabilities in TEM [60].

3.3.2 Semiconductors: Silicon and Carbon

In this subsection, carbon refers specifically to diamond, which behaves as a wide–bandgap semiconductor.

In semiconductors, there is a finite intrinsic carrier density, even in the absence of irradiation. At room temperature, typical values are

$$n_i^{\mathrm{Si}} \simeq 1.0 \times 10^{16}\,\mathrm{m}^{-3}, \qquad n_i^{\mathrm{C}} \sim 10^{8}\text{–}10^{10}\,\mathrm{m}^{-3},$$

depending on crystal structure and purity. Recombination proceeds via multiple channels, including band-to-band, Shockley–Read–Hall, and Auger processes. An effective recombination coefficient in moderately doped silicon is typically

$$\alpha_{\mathrm{rec}}^{\mathrm{eff}} \sim 10^{-19}\text{–}10^{-17}\,\mathrm{m}^3/\mathrm{s}.$$

These values are consistent with standard band-to-band, defect-assisted (Shockley–Read–Hall), and Auger recombination rates reported in semiconductor transport theory and beam-irradiation studies [11, 57, 58, 61].

In the presence of intrinsic carriers, relaxation after beam switch-off becomes exponential, with characteristic time

$$t_{\mathrm{rel}} = \frac{1}{2\alpha_{\mathrm{rec}} n_i}.$$

For silicon at room temperature, this yields

$$t_{\mathrm{rel}}^{\mathrm{Si}} \sim 10^{-3}\text{–}10^{-1}\,\mathrm{s},$$

while for carbon-based semiconductors the relaxation time may extend to seconds or longer. In contrast to insulators, semiconductors exhibit partial self-neutralization due to their intrinsic carrier population. However, relaxation remains slow compared to typical beam dwell times (STEM) or blanking times (TEM), implying that transient charging effects may still accumulate during scanning.

3.3.3 Metals: Aluminum

Metals represent the opposite extreme. In aluminum, the conduction electron density is of order

$$n_i^{\mathrm{Al}} \simeq 1.8 \times 10^{29}\,\mathrm{m}^{-3},$$

many orders of magnitude larger than any beam-induced excess density. Using the same effective recombination formalism, one finds

$$t_{\mathrm{rel}}^{\mathrm{Al}} \sim \frac{1}{2\alpha_{\mathrm{rec}} n_i} \lesssim 10^{-15}\text{–}10^{-12}\,\mathrm{s},$$

even for conservative estimates of α_{rec}. This timescale is far shorter than any experimental temporal resolution in TEM. As a result:

- beam-induced charging is immediately neutralized;
- no persistent electric fields can develop;
- the rate-equation approach predicts a negligible departure from equilibrium.

The analytical expressions derived above allow for order-of-magnitude estimates of the relaxation time in real materials. Representative values for different classes of materials relevant to TEM experiments are summarized in Table 3.1.

Table 3.1: Typical intrinsic carrier densities, effective recombination coefficients, and order-of-magnitude relaxation times for different classes of materials under TEM irradiation. The reported time ranges reflect representative estimates rather than material-specific predictions.

Material	n_i [m^{-3}]	α_{rec} [m^3/s]	t_{rel}
SiO_2 (insulator)	≈ 0	10^{-22}–10^{-20}	ms–hours
Si (semiconductor)	10^{16}	10^{-19}–10^{-17}	ms–s
Al (metal)	10^{29}	$\gtrsim 10^{-18}$	fs–ps

These estimates demonstrate that the temporal response of a material to beam-induced ionization spans more than fifteen orders of magnitude, depending primarily on the intrinsic carrier density. The hydrogenic model introduced in this chapter therefore constitutes the fundamental building block upon which increasingly realistic descriptions can be constructed by progressively reintroducing intrinsic carriers and transport effects. These results show that the microscopic recombination dynamics translate into macroscopically distinct electrical relaxation behaviors, depending primarily on the intrinsic carrier density of the material. This connection is made explicit in the following section, where the time-dependent conductivity is introduced.

3.4 Macroscopic Electrical Response and Conductivity

The microscopic description developed in the previous sections provides the full temporal evolution of the free-carrier density under electron-beam irradiation and after beam switch-off. However, experimentally observable consequences in transmission electron microscopy are governed by macroscopic electrical quantities rather than by the carrier density itself.

Among these quantities, electrical conductivity plays a central role, as it controls charge transport, dielectric screening, and the persistence of beam-induced electric fields. In this section, we establish a direct connection between the time-dependent carrier density and the macroscopic conductivity of the irradiated sample [62, 63].

3.4.1 Definition of beam-induced conductivity

Under the assumptions adopted throughout this chapter—namely homogeneous irradiation, local charge neutrality, and absence of spatial transport—the electrical conductivity can be expressed as

$$\sigma(t) = e\left[\mu_e n_e(t) + \mu_h n_h(t)\right], \tag{3.21}$$

where μ_e and μ_h denote the electron and hole mobilities, respectively.

In the hydrogenic model considered here, each ionization event produces one free electron and one proton, and charge neutrality implies

$$n_e(t) = n_h(t) \equiv n(t).$$

The conductivity therefore reduces to

$$\boxed{\sigma(t) = e\big(\mu_e + \mu_h\big)\, n(t).} \tag{3.22}$$

This expression shows that the macroscopic electrical response is directly proportional to the carrier density generated by the beam.

3.4.2 Intrinsic and excess conductivity

In real materials, a finite conductivity may exist even in the absence of irradiation. Using again $n(t) = n_i + \Delta n(t)$, the conductivity can be written as

$$\boxed{\sigma(t) = \sigma_i + \Delta\sigma(t), \qquad \sigma_i = e\big(\mu_e + \mu_h\big) n_i,} \tag{3.23}$$

where σ_i represents the intrinsic conductivity of the material and $\Delta\sigma(t)$ the excess conductivity induced by the electron beam.

The latter is given by

$$\Delta\sigma(t) = e\big(\mu_e + \mu_h\big)\Delta n(t), \tag{3.24}$$

establishing a one-to-one correspondence between the temporal evolution of the excess carrier density and the macroscopic electrical response.

3.4.3 Conductivity build-up under continuous irradiation

During continuous electron-beam irradiation, the carrier density evolves according to the Riccati equation derived in Section 3.8, approaching the steady-state value n_{eq} on the characteristic time scale

$$t_{\mathrm{ch}} = \frac{1}{\sigma_{\mathrm{ion}}\Phi + 2\alpha_{\mathrm{rec}} n_{\mathrm{eq}}}.$$

As a consequence, the conductivity increases from its intrinsic value σ_i toward the steady-state conductivity

$$\boxed{\sigma_{\mathrm{eq}} = e\big(\mu_e + \mu_h\big)\big(n_i + \Delta n_{\mathrm{eq}}\big).} \tag{3.25}$$

This beam-induced enhancement of the conductivity improves local charge screening and temporarily suppresses the build-up of strong electric fields inside the irradiated volume.

3.4.4 Conductivity relaxation after beam switch-off

As discussed in the previous section, the beam switch-off time is chosen as

$$t_0 = 3\,t_{\mathrm{ch}},$$

so that the system has fully reached the steady state before irradiation ceases. When the electron beam is switched off, ionization processes cease abruptly and the subsequent evolution of the system is governed solely by recombination. Since the electrical conductivity is directly proportional to the free-carrier density, its temporal relaxation follows immediately from the analytical solutions derived in Eq. (3.18).

For $t > t_0$, the excess conductivity evolves as

$$\boxed{\Delta\sigma(t) = e\big(\mu_e + \mu_h\big)\frac{2n_i\Delta n_{\mathrm{eq}}\, e^{-2\alpha_{\mathrm{rec}}n_i(t-t_0)}}{2n_i + \Delta n_{\mathrm{eq}}\left[1 - e^{-2\alpha_{\mathrm{rec}}n_i(t-t_0)}\right]}.} \tag{3.26}$$

Here $\Delta n_{\mathrm{eq}} = n(t_0) - n_i$ denotes the excess carrier density at the switch-off time, and the corresponding excess conductivity is

$$\Delta\sigma_{\mathrm{eq}} \equiv \Delta\sigma(t_0) = e\big(\mu_e + \mu_h\big)\,\Delta n_{\mathrm{eq}}.$$

Two qualitatively distinct relaxation regimes naturally emerge:

- in the insulating or hydrogenic limit ($n_i \to 0$), the intrinsic conductivity is negligible and $\sigma(t) \simeq \Delta\sigma(t)$. In this case, the conductivity decays algebraically,

  $$\Delta\sigma(t) = \frac{\Delta\sigma_{\mathrm{eq}}}{1 + \alpha_{\mathrm{rec}}\Delta n_{\mathrm{eq}}(t-t_0)},$$

  reflecting the absence of an intrinsic carrier reservoir and of a well-defined relaxation timescale;

- in materials with a finite intrinsic carrier density ($n_i \gg \Delta n$), the conductivity relaxes exponentially with the intrinsic relaxation time

  $$t_{\mathrm{rel}} = \frac{1}{2\alpha_{\mathrm{rec}}n_i},$$

  leading to a rapid recovery of the equilibrium electrical state.

The algebraic decay characteristic of insulating systems is illustrated in Fig. 3.5, which shows the normalized conductivity $\sigma(t)/\sigma(t_0)$ following beam switch-off. The absence of an exponential timescale implies long-lived excess conductivity and underlies the persistent charging and memory effects commonly observed in poorly conducting samples under TEM irradiation.

For semiconductors and metals, the corresponding relaxation dynamics are not shown graphically. In these materials, the presence of a finite (or extremely large) intrinsic carrier density leads to exponential relaxation on timescales that are either much longer (semiconductors) or many orders of magnitude shorter (metals) than the temporal window relevant for TEM observations. Their behavior is therefore more appropriately summarized through analytical estimates and characteristic timescales, as discussed in the following sections.

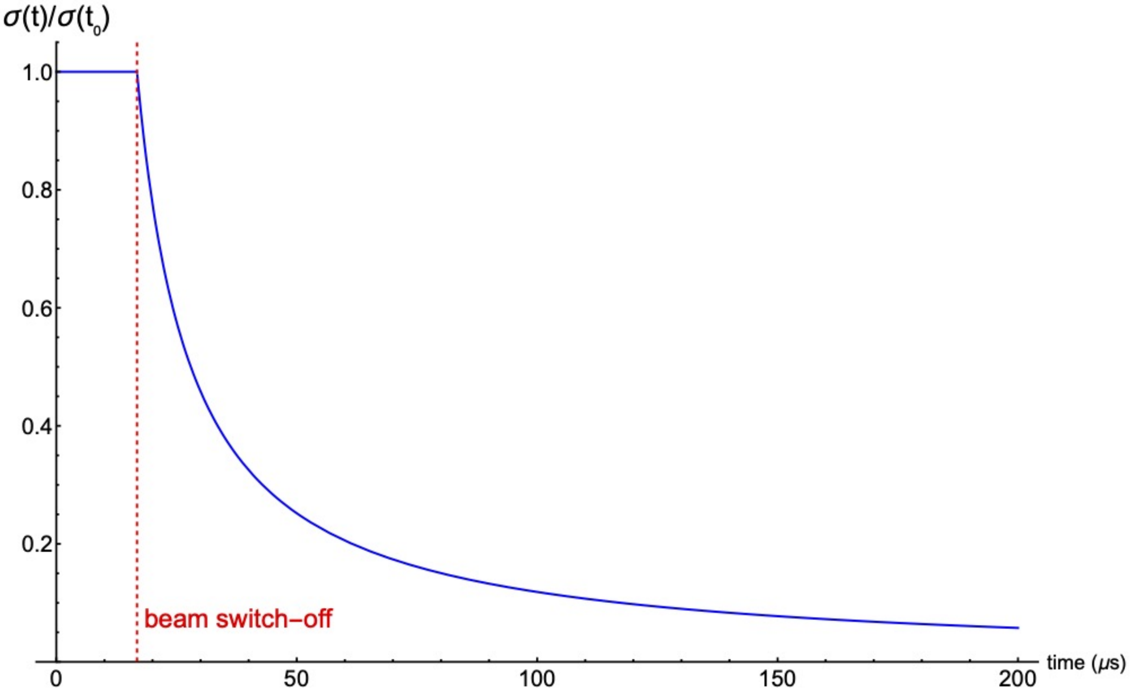

Figure 3.5: Normalized electrical conductivity $\sigma(t)/\sigma(t_0)$ after electron-beam switch-off in the insulating (hydrogenic) limit. The electron beam is switched off at time $t_0 = 3\,t_{\mathrm{ch}}$ (vertical red dashed line), after the system has reached the steady state under continuous irradiation. For $t > t_0$, ionization ceases and the carrier population relaxes solely via recombination, resulting in an algebraic decay of the conductivity. The absence of intrinsic carriers implies the lack of a well-defined intrinsic relaxation timescale, leading to long-lived excess conductivity and persistent charging effects. Time is expressed in microseconds to emphasize the experimentally relevant timescales under typical TEM conditions.

3.4.5 Dielectric relaxation and persistence of electric fields

The time-dependent conductivity directly controls the relaxation of internal electric fields. In a homogeneous medium, the dielectric relaxation time is defined as

$$\boxed{t_{\mathrm{d}}(t) = \frac{\varepsilon}{\sigma(t)},} \tag{3.27}$$

where ε is the permittivity of the material.

Immediately after beam switch-off, the enhanced conductivity due to excess carriers leads to efficient screening of electric fields. As recombination proceeds and $\Delta\sigma(t)$ decays, the dielectric relaxation time increases accordingly. In insulating materials, where $\sigma_i \simeq 0$, this mechanism can lead to electric fields persisting long after the free-carrier density has significantly decreased.

This delayed electrostatic relaxation provides a natural explanation for persistent beam deflection, image drift, and memory effects observed in TEM experiments on poorly conducting samples.

3.4.6 Implications for transmission electron microscopy

The analysis presented in this section highlights a key point: while the microscopic plasma dynamics are governed by ionization and recombination processes, the experimentally relevant timescales are set by the evolution of macroscopic electrical quantities.

In particular:

- beam-induced conductivity enhances charge screening during irradiation;
- slow conductivity relaxation leads to cumulative charging under repeated beam blanking or scanning;
- steady-state assumptions may fail even when the carrier density appears small.

In addition to charging-related imaging artifacts, a separate question is whether the beam-induced carrier population can feed back on the scattering process itself by modifying the screened interaction potential via the time-dependent Thomas–Fermi length $\lambda_{\mathrm{TF}}(t)$. This point is addressed quantitatively in the following.

3.4.7 Detectability of screening-induced changes in elastic scattering

A natural question is whether the ionization levels predicted by the present rate-equation model can have a non-negligible impact on the elastic scattering signal itself. The key link is the dependence of the Thomas–Fermi screening length on the instantaneous free-carrier density $n_e(t)$. Because $k_{\mathrm{TF}} \propto n_e^{1/6}$ in the degenerate Thomas–Fermi model,

$$\lambda_{\mathrm{TF}}(t) = k_{\mathrm{TF}}^{-1}(t) \propto n_e(t)^{-1/6},$$

even large changes in carrier density translate into comparatively modest variations of λ_{TF}.

For the representative TEM conditions considered in this chapter, the steady state corresponds to an ionization fraction $x = n_{\mathrm{eq}}/n_H^0 \sim 10^{-3}$–$2 \times 10^{-3}$, i.e. only

$\sim$ 1–2 ionized atoms per 10^3 hydrogen atoms. With $n_H^0 \simeq 10^{28}\,\mathrm{m}^{-3}$, this gives $n_e^{\mathrm{eq}} \simeq n_{\mathrm{eq}} \sim (1\text{–}2) \times 10^{25}\,\mathrm{m}^{-3}$, and therefore a screening length of order $\lambda_{\mathrm{TF}}^{\mathrm{eq}} \simeq 0.22$–$0.25\,\mathrm{nm}$.

The elastic Yukawa amplitude derived in the previous chapter reads

$$f(K) = \frac{2}{a_0}\frac{1}{K^2 + 1/\lambda_{\mathrm{TF}}^2}, \qquad \frac{\mathrm{d}\sigma}{\mathrm{d}\Omega} \propto \frac{1}{(K^2 + 1/\lambda_{\mathrm{TF}}^2)^2}.$$

A convenient measure of detectability is the ratio to the formally unscreened limit ($\lambda_{\mathrm{TF}} \to \infty$), for which $(\mathrm{d}\sigma/\mathrm{d}\Omega) \propto 1/K^4$:

$$\mathcal{R}(K,t) \equiv \frac{(\mathrm{d}\sigma/\mathrm{d}\Omega)_{\mathrm{screened}}}{(\mathrm{d}\sigma/\mathrm{d}\Omega)_{\mathrm{unscreened}}} = \left(\frac{K^2}{K^2 + 1/\lambda_{\mathrm{TF}}(t)^2}\right)^2.$$

For $\lambda_{\mathrm{TF}}^{\mathrm{eq}} \simeq 0.22$–$0.25\,\mathrm{nm}$ one has $1/\lambda_{\mathrm{TF}}^{\mathrm{eq}} \simeq 0.40$–$0.45\,\mathrm{\mathring{A}}^{-1}$, so that screening effects are confined primarily to very small momentum transfers, $K \lesssim 1/\lambda_{\mathrm{TF}}$ (forward scattering). For instance, taking $1/\lambda_{\mathrm{TF}} = 0.45\,\mathrm{\mathring{A}}^{-1}$ yields

$$K = 1\,\mathrm{\mathring{A}}^{-1}: \ \mathcal{R} \approx \left(\frac{1}{1 + 0.45^2}\right)^2 \simeq 0.69, \qquad K = 2\,\mathrm{\mathring{A}}^{-1}: \ \mathcal{R} \approx \left(\frac{4}{4 + 0.45^2}\right)^2 \simeq 0.91.$$

Therefore, at the stationary ionization level predicted here, the elastic cross section can be suppressed by tens of percent in the very-small-angle regime, while it is affected only weakly at medium and large K. In practice, detectability depends on the angular acceptance of the experiment: signals dominated by low-K scattering (e.g. bright-field or very small-angle measurements) are the most sensitive, whereas high-angle annular detection is expected to be largely insensitive to the screening variations induced by the transient plasma.

The time-dependent conductivity derived here thus constitutes the essential link between microscopic plasma formation and macroscopic electrical phenomena in transmission electron microscopy.

Chapter 4

Transport and Poisson Coupling in the Irradiated Sample

4.1 Electron Flow between Illuminated and Non-Illuminated Regions

Up to this point, the temporal evolution of ionization and recombination processes has been described under the simplifying assumption that all quantities depend solely on time, i.e. $n_e(t)$, $n_p(t)$, and $n_H(t)$ are spatially uniform within the irradiated region. In practice, however, the area directly exposed to the electron beam is surrounded by partially ionized or neutral zones, and charge transport between these regions plays a significant role [64, 65, 66, 67]. It is therefore necessary to extend the analysis to include both diffusion and drift phenomena.

We thus consider the more general case in which the charge densities and the electrostatic potential depend on both time and spatial coordinates, $n_{e,p} = n_{e,p}(\mathbf{r}, t)$ and $V = V(\mathbf{r}, t)$. Since protons are much heavier than electrons we have that $D_p <<$ D_e and $\mu_p << \mu_e$. Under these assumptions, the governing equations become

$$\frac{\partial n_e(\mathbf{r},t)}{\partial t} = D_e\nabla^2 n_e(\mathbf{r},t) + \nabla\cdot[\mu_e n_e(\mathbf{r},t)\mathbf{E}(\mathbf{r},t)] + G(\mathbf{r},t) - R(\mathbf{r},t), \tag{4.1}$$

$$\frac{\partial n_p(\mathbf{r},t)}{\partial t} = D_p\nabla^2 n_p(\mathbf{r},t) - \nabla\cdot[\mu_p n_p(\mathbf{r},t)\mathbf{E}(\mathbf{r},t)] + G(\mathbf{r},t) - R(\mathbf{r},t). \tag{4.2}$$

where

$$G = \sigma_{\text{ion}}\Phi(\mathbf{r},t)n_H(\mathbf{r},t), \tag{4.3}$$

$$R = \alpha_{\text{rec}}n_e(\mathbf{r},t)n_p(\mathbf{r},t). \tag{4.4}$$

Due to the axial symmetry of the problem, all quantities depend only on the radial coordinate r and time t. Under these conditions, the coupled equations governing

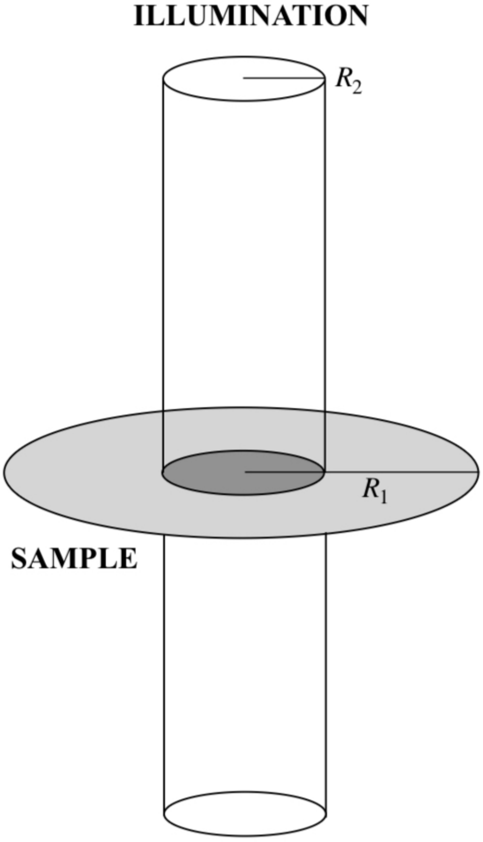

Figure 4.1: Primary beam of radius R_2 illuminating a circular sample of radius R_1 and negligible thickness.

electron transport and ion generation/recombination can be expressed as

$$\begin{aligned} \frac{\partial n_e(r,t)}{\partial t} &= \frac{1}{r}\frac{\partial}{\partial r}\left[r\left(D_e \frac{\partial n_e(r,t)}{\partial r} + \mu_e n_e(r,t) E_r(r,t) \right)\right] + G(r,t) - R(r,t), \\ \frac{\partial n_p(r,t)}{\partial t} &= \frac{1}{r}\frac{\partial}{\partial r}\left[r\left(D_p \frac{\partial n_p(r,t)}{\partial r} - \mu_p n_p(r,t) E_r(r,t) \right)\right] + G(r,t) - R(r,t), \qquad (4.5) \\ \frac{1}{r}\frac{\partial}{\partial r}\left(r\,\frac{\partial V(r,t)}{\partial r} \right) &= -\frac{q}{\varepsilon_0}\left[n_p(r,t) - n_e(r,t) \right]. \end{aligned}$$

The terms on the right-hand sides represent the local production and loss of charged particles due to ionization and recombination, respectively, as introduced in the previous chapter. The flux of primary electrons, $\Phi(r)$, is spatially dependent, following the beam profile (e.g. Gaussian or top-hat). The redistribution of charges gives rise to an electrostatic potential $V(r,t)$ satisfying Poisson's equation, where q is the elementary charge and ε_0 the vacuum permittivity.

4.1.1 Steady–state drift–diffusion and ionization balance

In the present model, we describe the beam-induced evolution of a pure hydrogen sample using coupled drift–diffusion equations for electrons and protons, together with a reaction balance for neutral atoms and a Poisson equation for the self-consistent electrostatic potential. Before writing down the full set of steady-state equations, we explicitly state the physical assumptions and sign conventions adopted throughout this section. All reaction terms are consistently written in the form $-G + R$, i.e. recombination minus ionization. Ionization acts as a loss channel for neutral atoms and a source for free carriers, whereas recombination acts as a gain channel for neutrals and a loss for free electrons and protons. Accordingly, the reaction term appearing on the right-hand side of the continuity equations takes the explicit form $-\sigma_{\text{ion}}\Phi(r)\, n_H + \alpha_{\text{rec}}\, n_e n_p$, where σ_{ion} is the (effective) ionization cross section, $\Phi(r)$ denotes the primary electron flux, and α_{rec} is the recombination coefficient.

In order to close the system, we make the following assumptions: (i) only one ionic species is present, namely protons H^+, so that each ionization event creates exactly one electron and one proton; (ii) no additional chemical pathways are considered (e.g. dissociation, molecular formation, attachment, or multi-step ionization are neglected), ensuring local conservation of hydrogen nuclei; and (iii) neutral hydrogen atoms are assumed immobile on the relevant time- and length-scales, so that no diffusive or drift transport term appears in the balance equation for n_H. Under these assumptions, the local densities satisfy $n_H(r,t) + n_p(r,t) = n_H^0 = \text{const.}$ at all times.

In steady state, beam-induced charge separation remains small but non-negligible, leading to the formation of internal electric fields that sustain drift currents and modify the local ionization balance.

For a pure hydrogen sample, the neutral density $n_H(r,t)$ evolves according to

$$\frac{\partial n_H}{\partial t} = -\sigma_{\text{ion}}\, \Phi(r)\, n_H + \alpha_{\text{rec}}\, n_e n_p, \tag{4.6}$$

with $n_H(r,t) = n_H^0 - n_p(r,t)$ expressing conservation of hydrogen nuclei.

The previous equation describes a purely local reaction balance for neutral hydrogen and does not represent a transport equation.

Neutral atoms are assumed immobile on the relevant time and length scales ($D_H =$

0), so that no drift or diffusion term appears in the balance equation for n_H.

In the illuminated core of the beam, ionization dominates ($G \gg R$), whereas at larger radii recombination prevails, leading to progressive neutralization of the charge carriers diffusing outward. In steady state, the coupled electron–proton drift–diffusion system (4.5) reduces to

$$\begin{aligned}
\frac{1}{r}\frac{\mathrm{d}}{\mathrm{d}r}\left[r\left(-D_e\frac{\mathrm{d}n_e}{\mathrm{d}r}-\mu_e n_e E_r\right)\right] &= -\big(n_H^0-n_p\big)\sigma_{\mathrm{ion}}\Phi(r)+\alpha_{\mathrm{rec}}\,n_e\,n_p,\\
\frac{1}{r}\frac{\mathrm{d}}{\mathrm{d}r}\left[r\left(-D_p\frac{\mathrm{d}n_p}{\mathrm{d}r}+\mu_p n_p E_r\right)\right] &= -\big(n_H^0-n_p\big)\sigma_{\mathrm{ion}}\Phi(r)+\alpha_{\mathrm{rec}}\,n_e\,n_p,\\
\frac{1}{r}\frac{\mathrm{d}}{\mathrm{d}r}\left(r\,\frac{\mathrm{d}V}{\mathrm{d}r}\right) &= -\frac{q}{\varepsilon_0}\,[n_p(r)-n_e(r)].
\end{aligned} \tag{4.7}$$

The first two equations in (4.7) express radial conservation of the electron and proton particle fluxes, respectively, each consisting of a diffusive component (proportional to $D_{e,p}\,dn_{e,p}/dr$) and a drift component (proportional to $\mu_{e,p}n_{e,p}E_r$, with $E_r = -\,dV/dr$). The identical reaction terms on the right-hand side reflect the one-to-one correspondence between electrons and protons created or annihilated in ionization and recombination events.

The third equation is the Poisson equation in cylindrical coordinates, relating the electrostatic potential $V(r)$ to the local space-charge density $q\,[n_p(r)-n_e(r)]$.

4.1.2 Steady–state reductions and conceptual limitations

Although the stationary drift–diffusion–Poisson system (4.7) can be written in compact form, its physical content and mathematical structure remain highly nontrivial. At first glance, the problem appears susceptible to further simplifications motivated by the experimental TEM/STEM geometry. In particular, it is natural to approximate the primary electron flux by a sharply localized top–hat profile,

$$\Phi(r)=\begin{cases}\Phi_0, & 0<r<R_2,\\[1em] 0, & R_2<r<R_1,\end{cases}$$

and to neglect proton transport altogether, exploiting the large mass ratio between ions and electrons. This corresponds to setting $D_p = 0$ and $\mu_p = 0$, thereby treating protons as effectively immobile on the relevant length and time scales.

Under these assumptions, the stationary proton balance equation reduces locally to

$$0 = -G(r) + R(r),$$

where the reaction term $-G + R$ is identical to that appearing in the electron equation, reflecting the one–to–one creation and annihilation of electron–proton pairs in ionization and recombination events. While this local condition may appear physically reasonable, its combination with transport and boundary conditions appropriate to a finite TEM sample leads to fundamental conceptual difficulties.

Imposing $0 = -G + R$ pointwise enforces the vanishing of the divergence of the electron particle flux. When combined with standard boundary conditions at the sample edge, this constraint forces the electron current to vanish identically, $J_e(r) = 0$. In the presence of a self–consistent electric field, the condition $J_e = 0$ yields solutions in which the electron density grows exponentially with the electrostatic potential, an outcome that is clearly unphysical. This pathology does not originate from an inappropriate choice of parameters but from the incompatibility between a strictly local reaction balance and global transport in a finite, partially illuminated system. It highlights the internal inconsistency of enforcing local stationarity while simultaneously suppressing ion transport.

A commonly adopted conceptual remedy consists in introducing an effective neutralization term for the ions, leading to a modified stationary proton balance equation of the form

$$0 = -G(r) + R(r) + \frac{n_p(r)}{\tau_p},$$

where τ_p is an effective ion lifetime. Physically, this term accounts for neutralization processes not explicitly resolved by the model, including surface recombination, interaction with secondary electrons, or charge relaxation mechanisms occurring outside the region explicitly described by the transport equations. The inclusion of n_p/τ_p restores conceptual consistency and prevents the pathological constraint $J_e = 0$. However, it does not lead to a substantial mathematical simplification. The resulting system remains fully nonlinear, strongly coupled through Poisson's equation, and characterized by widely separated spatial and temporal scales. As a consequence, it is highly stiff and numerically unstable, and quantitative steady–state solutions cannot be regarded as robust within this level of description [57, 61].

4.1.3 Validity limits and absence of quasi–neutrality

A further crucial aspect distinguishing the present TEM/STEM configuration from classical transport problems is the inapplicability of the quasi–neutrality approximation. In contrast to situations involving spatially uniform or infinite illumination, where transport can be neglected and quasi–neutrality imposed, the focused electron beam considered here induces strong spatial inhomogeneities. Charge transport between illuminated and non–illuminated regions is essential to the steady state, and local charge imbalances cannot be neglected. The electrostatic potential must therefore be determined self–consistently from Poisson's equation.

This situation differs fundamentally from the classical treatments discussed in the context of semiconductor physics or the Dember effect [68], where quasi–neutral approximations rely on spatially extended excitation and weak internal fields.

In the present geometry, the coexistence of generation, transport, and recombination over finite spatial scales precludes any local neutral approximation, even though global charge neutrality must still be preserved.

It is also important to stress that the present model neglects the possibility of secondary ionization events induced by the secondary electrons themselves [65, 67]. That is, electrons produced by primary ionization are assumed to lose energy predominantly through elastic scattering, transport, and recombination, without contributing to further ionization of nearby neutral atoms. This approximation is justified in the regime considered here, where secondary electrons are expected to have insufficient energy and range to sustain a significant ionization cascade. Including such processes would require a kinetic treatment of the secondary electron energy distribution and lies beyond the scope of the present drift–diffusion framework.

4.1.4 Boundary and matching conditions

The physical interpretation of the model relies critically on the choice of boundary and matching conditions, which reflect both the cylindrical symmetry and the finite extent of the sample. At the center of the system, regularity requires

$$\left.\frac{\mathrm{d}n_e}{\mathrm{d}r}\right|_{r=0} = \left.\frac{\mathrm{d}n_p}{\mathrm{d}r}\right|_{r=0} = 0, \qquad \left.\frac{\mathrm{d}V}{\mathrm{d}r}\right|_{r=0} = 0,$$

ensuring finite particle densities and a vanishing electric field at the origin.

At the outer radius $r = R_1$, the electron density is required to vanish,

$$n_e(R_1) = 0,$$

reflecting complete recombination or loss of electrons at the sample boundary. The electrostatic potential is defined up to an additive constant, while global charge neutrality of the sample is enforced through the coupled transport and Poisson equations.

At the interface $r = R_2$ separating the illuminated and non–illuminated regions, continuity conditions must be imposed. Specifically, the densities $n_e(r)$ and $n_p(r)$, the electrostatic potential $V(r)$, and the corresponding particle fluxes must be continuous across R_2. These matching conditions ensure a consistent coupling between regions with and without generation and prevent unphysical discontinuities in charge or current densities.

4.1.5 Qualitative physical picture and illustrative profiles

Within these constraints, the steady–state transport regime in a partially illuminated TEM/STEM sample admits primarily a qualitative and physically intuitive interpretation. The finite spatial extent of the primary electron beam introduces an intrinsic inhomogeneity, giving rise to distinct illuminated and non–illuminated regions whose coupling is governed by charge transport and electrostatic self–consistency.

In the illuminated core $0 < r < R_2$, the primary electron beam continuously ionizes neutral hydrogen atoms, producing electron–proton pairs. Protons, being effectively immobile on the relevant time and length scales, accumulate predominantly within this region and are neutralized on a characteristic timescale τ_p, which accounts for recombination and additional neutralization mechanisms not explicitly resolved by the transport equations. Electrons, by contrast, are highly mobile and respond rapidly to concentration gradients and internal electric fields. As a result, they diffuse and drift away from the illuminated region, progressively recombining as they migrate outward.

In the dark region $R_2 < r < R_1$, no further generation occurs. The electron density therefore decreases monotonically with radius until it vanishes at the sample boundary, where complete recombination or loss is imposed through the boundary condition $n_e(R_1) = 0$. The proton density, on the other hand, is strongly suppressed outside the illuminated region due to the absence of local generation and the effective neutralization mechanism. Consequently, the electron density extends throughout the sample to sustain transport and current continuity, whereas the proton density remains localized near the beam spot.

Although local quasi–neutrality is violated, the total charge of the sample remains strictly zero. This global neutrality is enforced by the boundary conditions and by the coupled drift–diffusion–Poisson dynamics. Local charge imbalances, while small in magnitude, play a crucial role in generating the internal electric field that couples transport and recombination processes.

To illustrate this physical picture, Fig. 4.2 shows schematic radial profiles of the proton and electron densities.

The illuminated region $0 < r < R_2$ is characterized by a pronounced accumulation of protons and a high electron density, while in the non–illuminated region the electron density extends beyond the generation zone due to diffusion and drift, eventually vanishing at the sample boundary. These profiles are not intended to represent a specific numerical solution, but rather to convey the qualitative features of transport and recombination in a finite, partially illuminated sample.

The corresponding net space–charge density $\rho(r) = q\,[n_p(r) - n_e(r)]$ is shown schematically in Fig. 4.3.

While the local charge density remains small compared to the individual carrier densities, it is non–zero and spatially structured. Its integral over the sample vanishes, ensuring global charge neutrality, yet these local deviations from neutrality act as the source of the self–consistent electrostatic field.

Figure 4.4 illustrates the qualitative profile of the internal radial electric field arising from beam–induced charge separation.

The field vanishes at the center of the sample by symmetry, increases within the illuminated region, and reaches a maximum near the interface $r = R_2$ separating

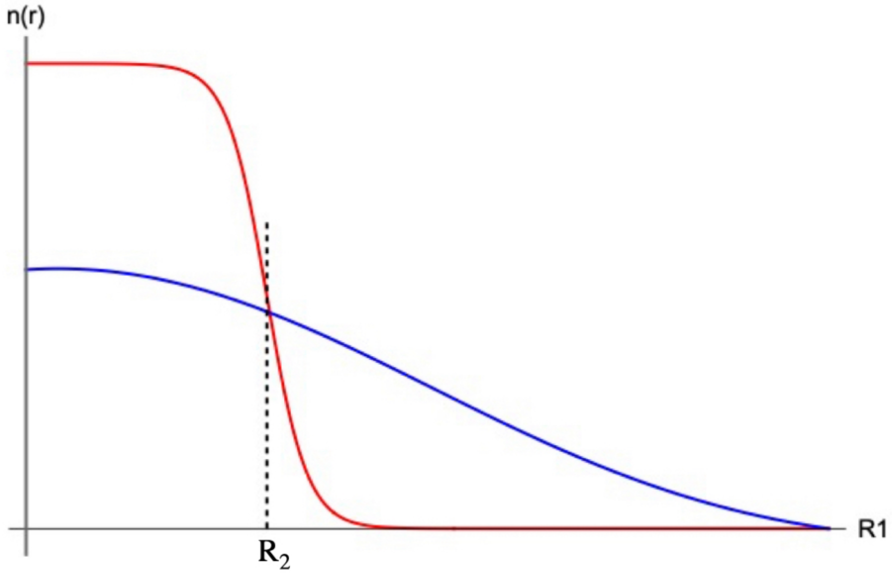

Figure 4.2: Schematic radial profiles of the proton density $n_p(r)$ (red curve) and electron density $n_e(r)$ (blue curve) in the steady–state TEM/STEM configuration. The dashed line indicates the electron-beam radius R_2, which marks the boundary of the illuminated region where primary carrier generation occurs. The region $0 < r < R_2$ corresponds to the area directly illuminated by the primary electron beam, while $R_2 < r < R_1$ denotes the non–illuminated (dark) region. Protons are assumed to be effectively immobile and therefore accumulate predominantly within the illuminated core, whereas electrons, being highly mobile, diffuse and drift beyond R_2 and progressively recombine as they approach the sample boundary at $r = R_1$, where $n_e(R_1) = 0$ is imposed. The profiles are purely illustrative and are intended to convey the qualitative features of transport and recombination in a finite, partially illuminated sample.

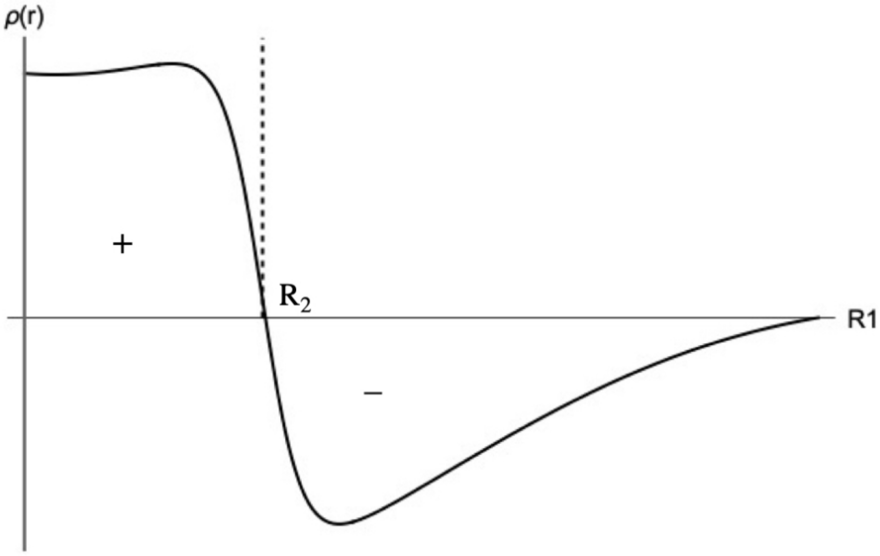

Figure 4.3: Schematic profile of the net space–charge density $\rho(r) = q\,[n_p(r) - n_e(r)]$ corresponding to the density distributions shown in Fig. 4.2. The dashed line indicates the electron-beam radius R_2, which marks the boundary of the illuminated region where primary carrier generation occurs. Although the local charge density remains small compared to the individual carrier densities, it is non–zero and spatially structured, reflecting the imbalance between ion generation and electron transport. The total integrated charge over the sample vanishes, ensuring global charge neutrality, while local deviations from neutrality act as the source of the self–consistent electrostatic field.

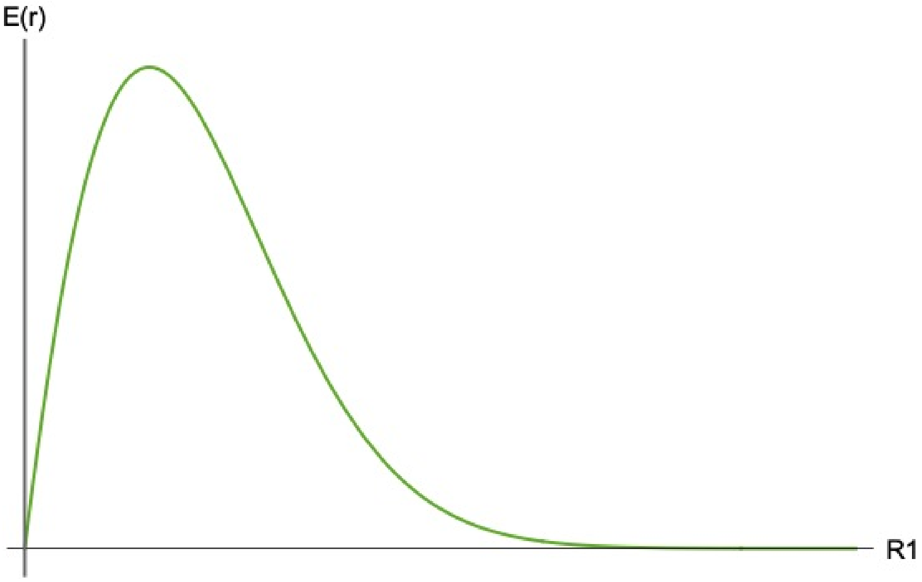

Figure 4.4: Qualitative profile of the self–consistent radial electric field $E(r)$ arising from beam–induced charge separation. The field vanishes at the center of the sample by symmetry, increases in the illuminated region, and reaches a maximum near the interface $r = R_2$ separating illuminated and non–illuminated zones. It then decays toward the sample boundary at $r = R_1$. This internally generated field sustains electron drift and ensures current continuity in steady state, playing a role analogous to the Dember field in classical photoexcitation problems.

illuminated and non–illuminated zones. It then decays toward the outer boundary. This internally generated field sustains electron drift and ensures current continuity in steady state, playing a role closely analogous to the Dember field in classical photoexcitation problems.

Finally, the associated electrostatic potential is shown schematically in Fig. 4.5.

The potential varies smoothly across the sample and is defined up to an additive constant, reflecting the absence of externally applied bias. Despite the smoothness of $V(r)$, its gradient gives rise to a non–negligible electric field that governs the drift component of electron transport and couples the illuminated and dark regions.

4.1.6 Order-of-magnitude estimate of the internal field and potential

Although Figs. 4.2–4.5 are schematic, it is useful to provide an order-of-magnitude estimate of the maximum self-consistent electric field and potential compatible with the carrier densities obtained in Fig. 3.1. The Poisson equation implies that a nonzero net space charge $\rho(r) = q\,[n_p(r) - n_e(r)]$ generates an internal field. For an order-of-

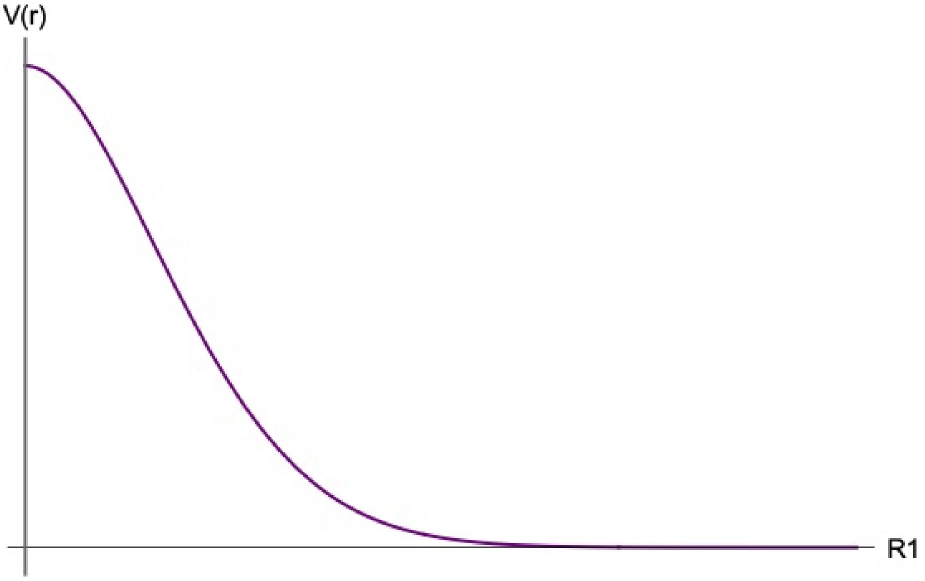

Figure 4.5: Schematic radial profile of the electrostatic potential $V(r)$ associated with the electric field shown in Fig. 4.4. The potential varies smoothly across the sample and remains finite everywhere, reflecting the absence of externally applied bias. Despite the smoothness of $V(r)$, its gradient gives rise to a non–negligible electric field that couples transport and recombination processes. The absolute value of the potential is defined up to an additive constant, while its spatial variation is fully determined by Poisson coupling and the imposed boundary conditions.

magnitude estimate, we approximate the characteristic scale of charge separation by the beam radius R_2 and assume that the local deviation from neutrality is a small fraction of the carrier density,

$$\Delta n_{\mathrm{ch}} \equiv n_p - n_e \simeq \eta\, n, \qquad 0 < \eta \ll 1, \tag{4.8}$$

where η quantifies the degree of local non-neutrality.

With this assumption, Poisson coupling yields the scaling

$$E_{\max} \sim \frac{q\,\Delta n_{\mathrm{ch}}\,R_2}{2\varepsilon_0} = \frac{q\,\eta\,n\,R_2}{2\varepsilon_0}, \qquad V_{\max} \sim E_{\max}\,R_2 \sim \frac{q\,\eta\,n\,R_2^2}{2\varepsilon_0}, \tag{4.9}$$

where the numerical factor is not essential at the present level of approximation (it depends on the precise radial profile).

Using the representative TEM parameter set of Fig. 3.1, the steady-state carrier density is $n \simeq n_{\mathrm{eq}} \sim 10^{25}\,\mathrm{m}^{-3}$. For a typical TEM illuminated diameter of $d \simeq 1\ \mu$m we have $R_2 \simeq 0.5\ \mu$m, which gives

$$E_{\max} \sim 4.5 \times 10^{10}\,\eta\ \mathrm{V/m}, \qquad V_{\max} \sim 2.3 \times 10^{4}\,\eta\ \mathrm{V}.$$

Therefore, even a very small charge-imbalance level $\eta \sim 10^{-5}$–10^{-4} corresponds to fields in the range $E_{\max} \sim 10^5$–$10^6\,\mathrm{V/m}$ and potentials of order $V_{\max} \sim 0.2$–$2\,\mathrm{V}$ across the illuminated region. These values are consistent with the qualitative picture of a weak but non-negligible internal field required to sustain drift currents and current continuity between illuminated and non-illuminated regions. Importantly, they also show that macroscopic electrostatic effects can be significant even when the ionization fraction remains at the level of $x \sim 10^{-3}$.

The profiles shown in Figs. 4.2–4.5 are schematic and are intended to provide an intuitive physical picture of the steady–state transport regime in a finite, partially illuminated TEM/STEM sample. In the spirit of classical representations of charge-separation effects (e.g. the Dember-effect picture, see Fig. V.3 in [68]), they do not correspond to a quantitative solution of the coupled drift–diffusion–Poisson equations, but rather illustrate the essential interplay between generation, diffusion, drift, recombination, and Poisson coupling.

Conclusions

This thesis has developed a unified theoretical framework to describe electron–matter interaction in transmission and scanning transmission electron microscopy across multiple physical scales, from microscopic scattering events to macroscopic electrical response under sustained irradiation.

The starting point of the analysis was a first–principles treatment of elastic and inelastic electron scattering within the first Born approximation. Both excitation and ionization processes were derived explicitly for hydrogen and carbon targets, emphasizing the role of screening, momentum transfer, and wavefunction structure. While simplified atomic models were intentionally adopted to preserve analytical tractability, their limitations were carefully identified and discussed, clarifying the distinction between idealized transitions and experimentally observed EELS edges. This microscopic description provided quantitative cross sections and transition amplitudes that serve as the fundamental input for all subsequent stages of the work.

A central theme of the thesis is the role of beam geometry. By extending the conventional plane–wave formulation to a spherical–wave description of the incident electron beam, the analysis demonstrated how finite source position and beam convergence modify the angular structure and magnitude of scattering amplitudes. In the plane–wave limit, the standard Born results are recovered, while at finite source distances the curvature of the wavefront leads to amplitude suppression, angular broadening, and symmetry breaking [24]. These effects are shown to be particularly relevant under modern STEM conditions, where tightly focused probes and off–axis illumination are routinely employed [6, 69]. The spherical–wave formalism therefore provides a more realistic foundation for interpreting elastic scattering, HAADF–STEM contrast, and wavefront–engineered imaging modalities.

Building upon the microscopic scattering description, the thesis then addressed the temporal evolution of beam–induced ionization in an irradiated sample. A minimal rate–equation model was formulated to describe the competition between ionization and recombination, leading to a Riccati equation governing the time–dependent free–carrier density. Its analytical solution revealed the emergence of a transient, beam–induced plasma whose build–up and steady–state density depend sensitively on the incident flux, ionization cross section, recombination coefficient, and initial neutral density. The stability analysis showed that the steady state is always dynamically stable, with a characteristic charging time that can be orders of magnitude shorter than experimental blanking times/dwell times in TEM/STEM.

A key physical insight of this work is the fundamental asymmetry between charging and relaxation processes. While carrier generation under irradiation is externally driven and typically fast, the relaxation following beam switch–off is internally controlled and strongly material–dependent. By explicitly solving the post–irradiation relaxation dynamics, the analysis demonstrated that insulating and hydrogenic systems exhibit algebraic decay and long–lived memory effects, whereas materials with finite intrinsic carrier density relax exponentially on timescales set by their recombination kinetics. This distinction provides a natural explanation for persistent charging, beam–induced drift, and history dependence commonly observed in electron microscopy experiments.

The connection between microscopic plasma dynamics and experimentally observable quantities was established through the introduction of a time–dependent conductivity. The beam–induced carrier density was shown to translate directly into an excess electrical conductivity, which in turn controls dielectric relaxation and the persistence of internal electric fields. This link explains why even modest carrier densities can produce pronounced electrostatic effects in poorly conducting samples, and why steady–state assumptions may fail under realistic scanning or pulsed illumination conditions.

Finally, the thesis extended the description to include spatial transport and self–consistent electrostatics through coupled drift–diffusion and Poisson equations. In a finite, partially illuminated TEM/STEM geometry, electron diffusion and drift between illuminated and non–illuminated regions were shown to be essential ingredients of the steady state. Local quasi–neutrality was demonstrated to be invalid, despite global charge neutrality being preserved. The resulting internal electric field, sustained by small but finite charge imbalances, plays a role analogous to the classical Dember field and ensures current continuity across the sample. Although the full stationary problem is intrinsically stiff and resists simple analytical or numerical solutions, the qualitative physical picture that emerges is robust and provides clear insight into the interplay between generation, transport, recombination, and electrostatic coupling.

Taken together, the results of this thesis show that electron–beam irradiation cannot, in general, be treated as a sequence of independent scattering events. Instead, it induces a dynamically evolving medium whose electrical properties depend on dose, geometry, and material parameters. The framework developed here bridges quantum scattering theory, plasma kinetics, and continuum electrodynamics, offering a coherent multiscale description of beam–sample interaction in modern electron microscopy.

Future work may extend this approach by incorporating secondary–electron cascades, energy–resolved transport, and fully time–dependent Poisson coupling, as well as by exploring the role of wavefront shaping in inelastic scattering. Such developments would further enhance the quantitative interpretation of TEM and STEM experiments and contribute to a predictive theory of irradiation–driven phenomena in nanoscale materials.

Acknowledgements

I would like to express my sincere and deepest gratitude to my supervisor, Prof. Marco Beleggia, for his continuous guidance, support, and scientific insight throughout the course of this work. His expertise, critical perspective, and clarity of thought have been essential in shaping both the direction and the rigor of this thesis, and in helping me develop a deeper and more coherent understanding of the physical problems addressed herein.

I am also profoundly grateful to Prof. Giulio Pozzi for the many invaluable scientific discussions and for his generous sharing of ideas and experience. His advice and intellectual openness have been a constant source of inspiration, and his contributions have significantly influenced the conceptual development of this work.

I would like to thank my colleagues and collaborators for the stimulating research environment and for many fruitful exchanges that enriched this project, both scientifically and personally. In particular, I wish to thank Payam Habibzadeh Kavkani, my PhD colleague, for the many discussions, collaborations, and moments of mutual support that made this journey more engaging and rewarding.

I am grateful to the members of the examination committee for their time, careful reading of the manuscript, and thoughtful evaluation of this work.

Finally, I wish to thank those who have supported me on a more personal level throughout these years. My deepest gratitude goes to my partner Sandro, for his unwavering support, patience, and understanding over many years. His constant presence, encouragement, and ability to stand by me through both the challenges and the uncertainties of this journey have been invaluable.

I am profoundly thankful to my family, my mother, my father, and my grandmother, for their unconditional love, trust, and encouragement. A special thought goes to my grandfather, who is no longer with us and cannot see me reach this milestone. I hope that, in some way, this achievement can still reach him.

Their presence, support, and belief in me have been essential throughout this path, and this work is also dedicated to them.

Appendix A

Explicit calculation of the total electron–hydrogen Ionization cross section

Replacing

$$\chi_s(\mathbf{r}_2) = \frac{e^{\mathrm{i}\mathbf{k}_s\cdot\mathbf{r}_2}}{L^{3/2}}\, e^{\pi/(2a_0k_s)}\,\Gamma\left(1+\frac{i}{a_0k_s}\right)\,{}_1F_1\left(-\frac{\mathrm{i}}{a_0k_s};1;-\mathrm{i}(k_sr_2+\mathbf{k}_s\cdot\mathbf{r}_2)\right). \tag{A.1}$$

in eq. (1.86) we obtain

$$\begin{aligned}\psi_n^{(+)}(\mathbf{r}_1) &= -\frac{2m}{4\pi\hbar^2}\frac{e^{\mathrm{i}k_fr_1}e^{\pi/(2a_0k_s)}}{r_1L^{3/2}}\Gamma\left(1-\frac{\mathrm{i}}{a_0k_s}\right)\frac{1}{a_0^{3/2}\sqrt{\pi}}\times\\ &\times\iint \mathrm{d}\mathbf{r}_1\,\mathrm{d}\mathbf{r}_2\,\left\{e^{\mathrm{i}(\mathbf{k}_i-\mathbf{k}_f)\cdot\mathbf{r}_1}\frac{e^2}{4\pi\epsilon_0|\mathbf{r}_1-\mathbf{r}_2|}e^{-\mathrm{i}\mathbf{k}_s\cdot\mathbf{r}_2}\,e^{-r_2/a_0}{}_1F_1\left(-\frac{\mathrm{i}}{a_0k_s};1;-\mathrm{i}(k_sr_2+\mathbf{k}_s\cdot\mathbf{r}_2)\right)\right\}\end{aligned} \tag{A.2}$$

. The $\mathbf{r}_1$ integral can be simply solved, and we gain

$$\begin{aligned}\psi_{ion}^{(+)}(\mathbf{r}_1) &= -\frac{2m}{4\pi\hbar^2}\frac{e^{\mathrm{i}k_fr_1}e^{\pi/(2a_0k_s)}}{r_1L^{3/2}}\Gamma\left(1-\frac{\mathrm{i}}{a_0k_s}\right)\frac{e^2}{\epsilon_0\,K^2\,a_0^{3/2}\sqrt{\pi}}\times\\ &\times\int \mathrm{d}\mathbf{r}_2\,\left\{e^{\mathrm{i}(\mathbf{k}_i-\mathbf{k}_f)\cdot\mathbf{r}_2}e^{-\mathrm{i}\mathbf{k}_s\cdot\mathbf{r}_2}\,e^{-r_2/a_0}{}_1F_1\left(-\frac{\mathrm{i}}{a_0k_s};1;-\mathrm{i}(k_sr_2+\mathbf{k}_s\cdot\mathbf{r}_2)\right)\right\} =\\ &= -\frac{2m}{4\pi\hbar^2}\frac{e^{\mathrm{i}k_fr_1}e^{\pi/(2a_0k_s)}}{r_1L^{3/2}}\Gamma\left(1-\frac{\mathrm{i}}{a_0k_s}\right)\frac{e^2}{\epsilon_0\,K^2\,a_0^{3/2}\sqrt{\pi}}\times\\ &\times\int \mathrm{d}\mathbf{r}_2\,\left\{e^{\mathrm{i}(\mathbf{K}-\mathbf{k}_s)\cdot\mathbf{r}_2}\,e^{-r_2/a_0}{}_1F_1\left(-\frac{\mathrm{i}}{a_0k_s};1;-\mathrm{i}(k_sr_2+\mathbf{k}_s\cdot\mathbf{r}_2)\right)\right\}.\end{aligned} \tag{A.3}$$

It is convenient to write the previous integral in the following way:

$$-\frac{\partial}{\partial\lambda}\left\{\int \mathrm{d}\mathbf{r}_2\,e^{(\mathrm{i}\mathbf{K}\cdot\mathbf{r}_2-\mathrm{i}\mathbf{k}_s\cdot\mathbf{r}_2-\lambda r_2)}{}_1F_1\left(-\frac{\mathrm{i}}{a_0k_s};1;-\mathrm{i}(k_sr_2+\mathbf{k}_s\cdot\mathbf{r}_2)\right)\right\}\Bigg|_{\lambda=1/a_0} \tag{A.4}$$

This can be evaluated most efficiently in parabolic coordinates (ξ,η,φ):

$$x=\sqrt{\xi\eta}\cos\varphi,\qquad y=\sqrt{\xi\eta}\sin\varphi,\qquad z=(\xi-\eta)/2.$$

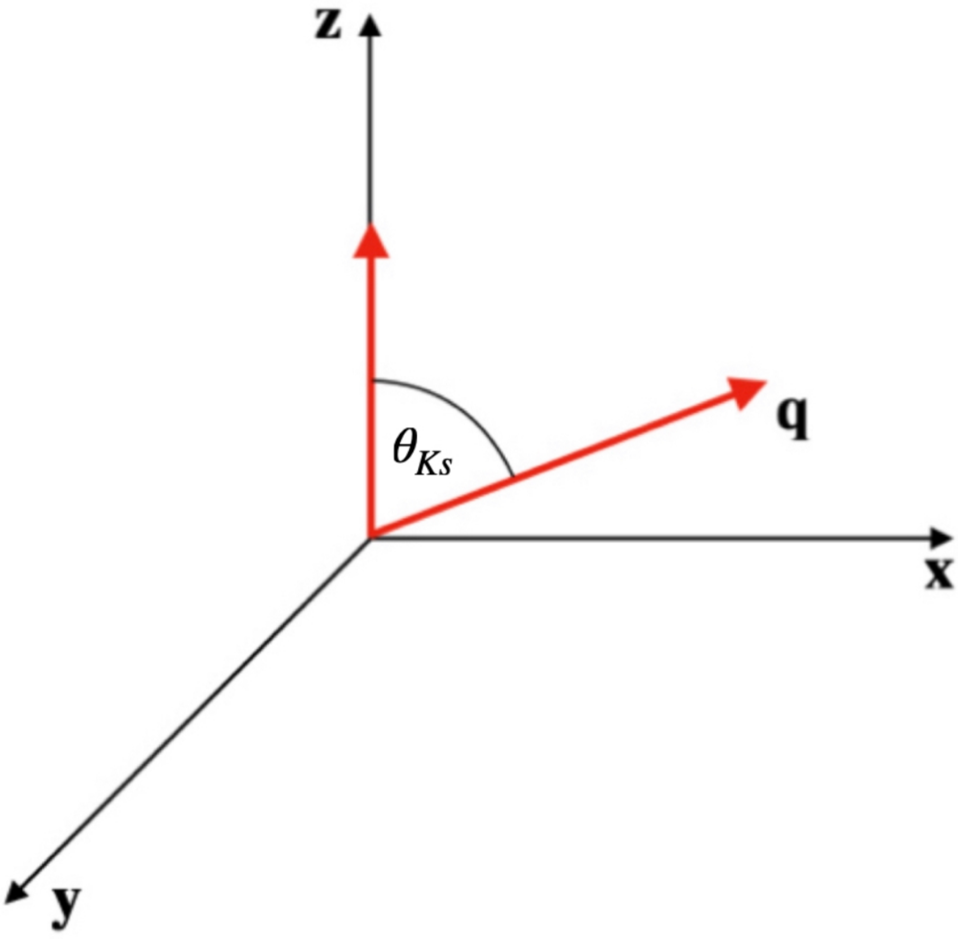

Figure A.1: Representation of the reference frame used to perform the integral in parabolic coordinates.

with $\xi \in [0, +\infty)$, $\eta \in [0, +\infty)$ and $\varphi \in [0, 2\pi)$, z-axis in $\mathbf{k}_s$ direction and φ angle calculated starting from the plane $(\mathbf{K}\,,\,\mathbf{k}_s)$. Let θ_{Ks} be the angle between $\mathbf{K}$ and $\mathbf{k}_s$ (as shown in fig. A.1). Since the Jacobian is given by $\mathrm{d}V = (\xi + \eta)/4 \;\, \mathrm{d}\xi\, \mathrm{d}\eta\, \mathrm{d}\varphi$, we have $r_2 = \sqrt{x^2 + y^2 + z^2} = (\xi + \eta)/2$. By symmetry, we may assume that $\mathbf{K}$ does not have components along the $\mathbf{y}$-axis; then

$$\mathbf{k}_s = (0, 0, k_s) \qquad \mathbf{K} = (K \sin\theta_{ks}, 0, K\cos\theta_{ks})$$

and (A.4) becomes

$$
-\frac{\partial}{\partial\lambda}\Bigg\{\int_0^\infty \mathrm{d}\xi \int_0^\infty \mathrm{d}\eta \int_0^{2\pi} \mathrm{d}\varphi\, \frac{e^{\mathrm{i}K\sqrt{\xi\eta}\cos\varphi\sin\theta_{ks}}}{\frac{1}{2}(\xi+\eta)} e^{\mathrm{i}K\cos\theta_{ks}(\xi-\eta)/2} e^{-\mathrm{i}k_s(\xi-\eta)/2} \times \\
\times\, e^{\lambda(\xi+\eta)/2}\frac{(\xi+\eta)}{4}\, {}_1F_1\left(\frac{\mathrm{i}}{k_s a_0}, 1, \mathrm{i}k_s\xi\right)\Bigg\}\Bigg|_{\lambda=1/a_0}. \quad (A.5)
$$

The $\int \mathrm{d}\varphi$ can be done immediately and gives $2\pi J_0(K\sqrt{\xi\eta}\,\sin\theta_{ks})$, while the Hypergeometric function does not depend on η, so

$$
-\pi\frac{\partial}{\partial\lambda}\int_0^\infty \mathrm{d}\xi e^{\mathrm{i}(K/2)\xi\cos\theta_{ks}} e^{-\mathrm{i}\xi k_s/2} e^{-\lambda\xi/2}\, {}_1F_1\left(\frac{\mathrm{i}}{k_s a_0}, 1, \mathrm{i}k_s\xi\right) \times \\
\times \int_0^\infty \mathrm{d}\eta J_0(K\sqrt{\xi\eta}\sin\theta_{ks}) e^{-\mathrm{i}K\eta/2\cos\theta_{ks}} e^{\mathrm{i}k_s\eta/2} e^{-\lambda\eta/2}. \quad (A.6)
$$

But since

$$
\int_0^\infty \mathrm{d}\eta J_0(A\sqrt{\eta}) e^{\eta B} = -\frac{e^{A^2/4B}}{B} \quad (A.7)
$$

we have

$$
\int_0^\infty \mathrm{d}\eta J_0(K\sqrt{\xi}\sqrt{\eta}\sin\theta_{ks}) e^{\eta(-\mathrm{i}K\cos\theta_{ks}+\mathrm{i}k_s-\lambda)/2} = \frac{-2e^{\frac{K^2\xi\sin^2\gamma}{2[\mathrm{i}(-K\cos\theta_{ks}+k_s)-\lambda]}}}{\mathrm{i}(-K\cos\theta_{ks}+k_s)-\lambda}. \quad (A.8)
$$

The integral (A.5) can be rearranged as

$$
-\pi\frac{\partial}{\partial\lambda}\Bigg\{\int_0^\infty \mathrm{d}\xi e^{\mathrm{i}(K/2)\xi\cos\theta_{ks}} e^{-\mathrm{i}\xi k_s/2} e^{-\lambda\xi/2}\, {}_1F_1\left(\frac{\mathrm{i}}{k_s a_0}, 1, \mathrm{i}k_s\xi\right) \frac{-2e^{\frac{K^2\xi\sin^2\gamma}{2[\mathrm{i}(-K\cos\theta_{ks}+k_s)-\lambda]}}}{i(-K\cos\theta_{ks}+k_s)-\lambda}\Bigg\}\Bigg|_{\lambda=1/a_0}. \quad (A.9)
$$

After a lengthy sequence of algebraic steps, we have

$$
2\pi\frac{\partial}{\partial\lambda}\Bigg\{\frac{1}{\mathrm{i}(-K\cos\theta_{ks}+k_s)-\lambda}\int_0^\infty d\xi\, e^{\frac{-\xi(-K^2-k_s^2-\lambda^2+2Kk_s\cos\theta_{ks})}{2\mathrm{i}(-K\cos\theta_{ks}+k_s)-2\lambda}}\, {}_1F_1\left(\frac{\mathrm{i}}{k_s a_0}, 1, \mathrm{i}k_s\xi\right)\Bigg\}\Bigg|_{\lambda=1/a_0}. \quad (A.10)
$$

The last integral, $\int \mathrm{d}\xi$, can be performed with the following formula, found in [70]:

$$
\int_0^\infty \mathrm{d}\xi e^{-A\xi}\, {}_1F_1(\alpha, 1, \beta\xi) = \Gamma(1) A^{\alpha-1}(A-B)^{-\alpha} \quad (A.11)
$$

which gives

$$2\pi\frac{\partial}{\partial\lambda}\left\{\frac{1}{\mathrm{i}(-K\cos\theta_{ks}+k_s)-\lambda}\left[\frac{1}{2}\frac{(-K^2-k_s^2-\lambda^2+2Kk_s\cos\theta_{ks})}{\mathrm{i}(-K\cos\theta_{ks}+k_s)-\lambda}\right]^{\frac{\mathrm{i}}{a_0k_s}-1}\times\right.$$
$$\left.\times\left[\frac{1}{2}\frac{(-K^2-k_s^2-\lambda^2+2Kk_s\cos\theta_{ks})}{\mathrm{i}(-K\cos\theta_{ks}+k_s)-\lambda}-\mathrm{i}k_s\right]^{-\frac{\mathrm{i}}{a_0k_s}}\right\}. \quad (A.12)$$

Using the properties of powers, one obtains, after some algebraic manipulation,

$$4\pi\frac{\partial}{\partial\lambda}\left\{(-K^2-k_s^2-\lambda^2+2Kk_s\cos\theta_{ks})^{\frac{\mathrm{i}}{a_0k_s}-1}(k_s^2-K^2-\lambda^2+2\mathrm{i}\lambda k_s)^{-\frac{\mathrm{i}}{a_0k_s}}\right\}\Bigg|_{\lambda=1/a_0}. \quad (A.13)$$

The derivative $\partial/\partial\lambda$ can be done and simplified with the help of a calculator (Mathematica). This gives us

$$-16\pi Ka_0^4\left[(\mathrm{i}+a_0k_s)^2-a_0^2K^2\right]^{-\frac{\mathrm{i}}{a_0k_s}-1}\left[-1-a_0^2k_s^2-a_0^2K^2+2a_0^2k_sK\cos\theta_{ks}\right]^{\frac{\mathrm{i}}{a_0k_s}-2}\times$$
$$\times\left[a_0K-(\mathrm{i}+a_0k_s)\cos\theta_{ks}\right]. \quad (A.14)$$

Finally we can write

$$\psi_{ion}^{(+)}(\mathbf{r}_1)=\frac{2me^2}{4\pi\hbar^2\epsilon_0}\frac{e^{\mathrm{i}k_fr_1}e^{\pi/(2a_0k_s)}}{r_1L^{3/2}}\Gamma\left(1-\frac{\mathrm{i}}{a_0k_s}\right)\frac{1}{K^2\,a_0^{3/2}\sqrt{\pi}}\Big\{-16\pi Ka_0^4\left[(\mathrm{i}+a_0k_s)^2+\right.$$
$$\left.-a_0^2K^2\right]^{-\frac{\mathrm{i}}{a_0k_s}-1}\left[-1-a_0^2k_s^2-a_0^2K^2+2a_0^2k_sK\cos\theta_{ks}\right]^{\frac{\mathrm{i}}{a_0k_s}-2}\left[a_0K-(\mathrm{i}+a_0k_s)\cos\theta_{ks}\right]\Big\}. \quad (A.15)$$

Since $me^2/4\pi\epsilon_0\hbar^2=1/a_0$, with some simplifications, we obtain exactly eq. (1.102) of the main text.

List of Figures

Bibliography

---

[1] M. Knoll and E. Ruska. “Das Elektronenmikroskop”. In: *Zeitschrift für Physik* 78 (1932), pp. 318–339. DOI: 10.1007/BF01342199.

[2] M. Haider et al. “Electron microscopy image enhanced by spherical aberration correction”. In: *Nature* 392 (1998), pp. 768–769.

[3] D. Van Dyck, S. Van Aert, and A. J. den Dekker. “Physical Limits on Atomic Resolution”. In: *Microscopy and Microanalysis* 10.1 (Feb. 2004), pp. 153–157. DOI: 10.1017/S143192760404036X.

[4] O. L. Krivanek et al. “Atom-by-atom structural and chemical analysis by annular dark-field electron microscopy”. In: *Nature* 514 (2014), pp. 209–212. DOI: 10.1038/nature13870.

[5] D.B. Williams and C.B. Carter. *Transmission Electron Microscopy: A Textbook for Materials Science*. Cambridge library collection v. 1. Springer, 2009. ISBN: 9780387765006. URL: https://books.google.it/books?id=dXdrG39VtUoC.

[6] Earl J. Kirkland. *Advanced Computing in Electron Microscopy*. 3rd. Springer, 2020. ISBN: 978-1-0716-0740-4. DOI: 10.1007/978-1-0716-0741-1.

[7] Ludwig Reimer and Helmut Kohl. *Transmission Electron Microscopy: Physics of Image Formation*. 5th. Springer, 2008. ISBN: 978-3-540-85226-1.

[8] John C. H. Spence. *High-Resolution Electron Microscopy*. 4th. Oxford University Press, 2013. ISBN: 9780199668618.

[9] R. F. Egerton. “Control of radiation damage in the TEM”. In: *Ultramicroscopy* 127 (Apr. 2013), pp. 100–108. DOI: 10.1016/j.ultramic.2012.07.006.

[10] R. F. Egerton. “Electron energy-loss spectroscopy in the TEM”. In: *Reports on Progress in Physics* 72.1, 016502 (Jan. 2009), p. 016502. DOI: 10.1088/0034-4885/72/1/016502.

[11] E. Bringuier. "The basis of the semiclassical description of electron transport in solids". In: *European Journal of Physics* 42.2, 025502 (Mar. 2021), p. 025502.

[12] R. F. Egerton. "Electron Energy-Loss Spectroscopy for Elemental Analysis". In: *Philosophical Transactions of the Royal Society of London Series A* 305.1491 (July 1982), pp. 521–531. DOI: 10.1098/rsta.1982.0049.

[13] C. J. Joachain. *Quantum Collision Theory*. 3rd. North-Holland, 1987.

[14] L. D. Landau and E. M. Lifshitz. *Quantum Mechanics: Non-Relativistic Theory*. Course of Theoretical Physics, Vol. 3. Pergamon Press, 1977.

[15] J. J. Sakurai and J. Napolitano. *Modern Quantum Mechanics*. 2nd. Pearson, 2017.

[16] D. Rapp. *Quantum Mechanics*. Holt, Rinehart and Winston, 1971. ISBN: 9780030812941. URL: https://books.google.it/books?id=dJzvAAAAMAAJ.

[17] R. G. Newton. *Scattering Theory of Waves and Particles*. Springer, 1982.

[18] H. M. Nussenzveig. *Introduction to Quantum Scattering Theory*. Academic Press, 1972.

[19] J. R. Taylor. *Scattering Theory: The Quantum Theory of Nonrelativistic Collisions*. Dover Publications, 1972.

[20] R. F. Egerton. *Electron Energy-Loss Spectroscopy in the Electron Microscope*. 3rd ed. Springer, 2012.

[21] J. M. Cowley and A. F. Moodie. "The scattering of electrons by atoms and crystals. I. A new theoretical approach". In: *Acta Crystallographica* 10 (1957), pp. 609–619.

[22] A. Howie and M. J. Whelan. "Diffraction Contrast of Electron Microscope Images of Crystal Lattice Defects. III. Results and Experimental Confirmation of the Dynamical Theory of Dislocation Image Contrast". In: *Proceedings of the Royal Society of London Series A* 267.1329 (May 1962), pp. 206–230. DOI: 10.1098/rspa.1962.0093.

[23] A. Howie and M. J. Whelan. "Diffraction Contrast of Electron Microscope Images of Crystal Lattice Defects. II. The Development of a Dynamical Theory". In: *Proceedings of the Royal Society of London Series A* 263.1313 (Sept. 1961), pp. 217–237. DOI: 10.1098/rspa.1961.0157.

[24] J. M. Cowley. *Diffraction Physics*. Elsevier, 1981.

[25] J. Verbeeck, H. Tian, and P. Schattschneider. "Production and application of electron vortex beams". In: *Nature* 467 (2010), pp. 301–304. DOI: 10.1038/nature09366.

[26] K. Gottfried and T.-M. Yan. *Quantum Mechanics: Fundamentals*. Springer, 2003.

[27] A. Messiah. *Quantum Mechanics, Vol. I–II*. North-Holland, 1961.

[28] Peter Schattschneider. *Fundamentals of Inelastic Electron Scattering*. Springer, 1986. ISBN: 9783211819371.

[29] H. Bethe. "Zur Theorie des Durchgangs schneller Korpuskularstrahlen durch Materie". In: *Annalen der Physik* 397 (1930), pp. 325–400.

[30] N. F. Mott. "The scattering of fast electrons". In: *Proceedings of the Royal Society A* 124 (1929), pp. 425–442.

[31] F. J. García de Abajo. "Relativistic effects in electron energy loss spectroscopy". In: *Physical Review B* 59 (1999), pp. 3095–3107.

[32] M. Inokuti. "Inelastic collisions of fast charged particles with atoms and molecules—The Bethe theory revisited". In: *Reviews of Modern Physics* 43 (1971), pp. 297–347.

[33] Robert G. Parr and Yang Weitao. *Density-Functional Theory of Atoms and Molecules*. Oxford University Press, USA, 1994. ISBN: 0195092767. URL: http://www.amazon.com/Density-Functional-Molecules-International-Monographs-Chemistry/dp/0195092767/ref=sr_1_1?ie=UTF8&s=books&qid=1279096906&sr=1-1.

[34] Enrico Clementi and D. L. Raimondi. “Atomic Screening Constants from SCF Functions”. In: *The Journal of Chemical Physics* 38.11 (1963), pp. 2686–2689. DOI: `10.1063/1.1733573`.

[35] Enrico Clementi, D. L. Raimondi, and W. P. Reinhardt. “Atomic Screening Constants from SCF Functions. II. Atoms with 37 to 86 Electrons”. In: *The Journal of Chemical Physics* 47.4 (1967), pp. 1300–1307. DOI: `10.1063/1.1712084`.

[36] Ann-Lenaig Hamon et al. “ELNES study of carbon K-edge spectra of plasma deposited carbon films”. In: *Journal of Materials Chemistry* 14 (2004), pp. 2030–2035. DOI: `10.1039/B406468M`.

[37] Xavier Llovet et al. “Cross Sections for Inner-Shell Ionization by Electron Impact”. In: *Journal of Physical and Chemical Reference Data* 43.1 (2014), p. 013102. DOI: `10.1063/1.4832851`.

[38] F. J. García de Abajo. “Optical excitations in electron microscopy”. In: *Reviews of Modern Physics* 82 (2010), pp. 209–275.

[39] Ján Rusz, Juan-Carlos Idrobo, and Somnath Bhowmick. “Achieving Atomic Resolution Magnetic Dichroism by Controlling the Phase Symmetry of an Electron Probe”. In: *Physical Review Letters* 113.14 (2014), p. 145501. DOI: `10.1103/PhysRevLett.113.145501`. arXiv: `1408.3150 [cond-mat.mtrl-sci]`.

[40] Ján Rusz et al. “Sum rules for electron energy-loss near-edge spectra”. In: *Physical Review B* 76 (2007), p. 060408. DOI: `10.1103/PhysRevB.76.060408`.

[41] H. Ibach et al. “Electron energy loss spectroscopy for studies of surface vibrations”. In: *Nuovo Cimento B Serie* 39.2 (June 1977), pp. 759–767. DOI: `10.1007/BF02725821`.

[42] R. H. Ritchie. “Plasma Losses by Fast Electrons in Thin Films”. In: *Physical Review* 106.5 (June 1957), pp. 874–881. DOI: `10.1103/PhysRev.106.874`.

[43] J Lindhard. “ON THE PROPERTIES OF A GAS OF CHARGED PARTICLES”. In: *Kgl. Danske Videnskab. Selskab Mat.-fys. Medd.* Vol: 28, No. 8 (Jan. 1954). URL: `https://www.osti.gov/biblio/4405425`.

[44] J. C. Ashley. "Interaction of low-energy electrons and positrons with condensed matter: Stopping powers and inelastic mean free paths from optical data". In: (Jan. 1989), pp. 4–7.

[45] Max Born and Emil Wolf. *Principles of Optics: Electromagnetic Theory of Propagation, Interference and Diffraction of Light (7th Edition)*. 7th. Cambridge University Press, 1999. ISBN: 0521642221.

[46] O. Scherzer. "The Theoretical Resolution Limit of the Electron Microscope". In: *Journal of Applied Physics* 20.1 (Jan. 1949), pp. 20–29. DOI: 10.1063/1.1698233.

[47] Helmut Kohl and Harald Rose. "Theory of Image Formation by Inelastically Scattered Electrons in the Electron Microscope". In: *Advances in Electronics and Electron Physics* 65 (1985), pp. 173–227. DOI: 10.1016/S0065-2539(08)60878-1.

[48] Peter Schattschneider et al. "The physical significance of the mixed dynamic form factor". In: *Micron* 31.4 (2000), pp. 333–345. DOI: 10.1016/S0968-4328(99)00112-2.

[49] A. Rothwarf. "Plasmon theory of electron-hole pair production: efficiency of cathode ray phosphors". In: *Journal of Applied Physics* 44.2 (1973), pp. 752–756. DOI: 10.1063/1.1662257.

[50] Wolfgang S. M. Werner et al. "Role of surface and bulk plasmon decay in secondary electron emission". In: *Physical Review B* 78.23 (2008), p. 233403. DOI: 10.1103/PhysRevB.78.233403.

[51] D L Book. *Nrl (Naval Research Laboratory) plasma formulary*. Tech. rep. Naval Research Lab., Washington, DC (USA), Jan. 1980. URL: https://www.osti.gov/biblio/5843656.

[52] J. D. Huba. *NRL Plasma Formulary*. Tech. rep. Washington, DC: Naval Research Laboratory, 2023. URL: https://www.nrl.navy.mil/Portals/38/PDF%20Files/NRL_Plasma_Formulary_2023.pdf?ver=Ffbv5HssiwiNJk2ZA2Zi9g%3D%3D%C3%97tamp=1698852579254.

[53] Gaber Omar and Yukap Hahn. “Dielectronic recombination in plasmas: The final state distribution”. In: *Physical Review E* 62.3 (Sept. 2000), pp. 4096–4103. DOI: 10.1103/PhysRevE.62.4096.

[54] Gaber Omar and Yukap Hahn. “Dielectronic recombination in plasmas. II. Initial excited states”. In: *Physical Review E* 63.4 (Apr. 2001), p. 046407. DOI: 10.1103/PhysRevE.63.046407.

[55] Y. Hahn. “Plasma density effects on the three-body recombination rate coefficients”. In: *Physics Letters A* 231.1 (Feb. 1997), pp. 82–88. DOI: 10.1016/S0375-9601(97)00287-9.

[56] D. R. Bates and A. Dalgarno. “Electronic Recombination”. In: *Pure and Applied Physics* 13 (Jan. 1962), pp. 245–271. DOI: 10.1016/B978-0-12-081450-3.50011-4.

[57] P. A. Markowich, C. A. Ringhofer, and C. Schmeiser. *Semiconductor Equations*. Springer, 1990.

[58] N. W. Ashcroft and N. D. Mermin. *Solid State Physics*. Holt, Rinehart and Winston, 1976.

[59] Charles Kittel. *Introduction to Solid State Physics*. 8th ed. Wiley, 2005.

[60] J. Cazaux. “Correlations between ionization radiation damage and charging effects in transmission electron microscopy”. In: *Ultramicroscopy* 60.3 (1995), pp. 411–425. ISSN: 0304-3991. DOI: https://doi.org/10.1016/0304-3991(95)00077-1. URL: https://www.sciencedirect.com/science/article/pii/0304399195000771.

[61] S. Selberherr. *Analysis and Simulation of Semiconductor Devices*. Springer, 1984.

[62] Robert M. Glaeser and Kenneth A. Taylor. “Radiation damage relative to transmission electron microscopy of biological specimens at low temperature: a review”. In: *Journal of Microscopy* 112.1 (1978), pp. 127–138. DOI: https://doi.org/10.1111/j.1365-2818.1978.tb01160.x. eprint: https://onlinelibrary.wiley.com/doi/pdf/10.1111/j.1365-2818.1978.tb01160.

x. URL: https://onlinelibrary.wiley.com/doi/abs/10.1111/j.1365-2818.1978.tb01160.x.

[63] C. Kisielowski et al. “Detection of Single Atoms and Buried Defects in Three Dimensions by Aberration-Corrected Electron Microscope with 0.5-Å Information Limit”. In: *Microscopy and Microanalysis* 14.5 (Oct. 2008), pp. 469–477. DOI: 10.1017/S1431927608080902.

[64] H.-J. Fitting and M. Touzin. “Secondary electron emission and self-consistent charge transport in semi-insulating samples”. In: *Journal of Applied Physics* 110.4, 044111-044111-10 (Aug. 2011), pp. 044111-044111–10. DOI: 10.1063/1.3608151.

[65] David Joy. *Monte Carlo Modeling for Electron Microscopy and Microanalysis*. Oct. 2023. ISBN: 9780195088748. DOI: 10.1093/oso/9780195088748.001.0001.

[66] J. M. Fernandez-Varea, J. D. Martinez, and F. Salvat. “A simplified method for the detailed Monte Carlo simulation of electron transport”. In: *Journal of Physics D Applied Physics* 24.6 (June 1991), pp. 814–826. DOI: 10.1088/0022-3727/24/6/004.

[67] M. Dapor. *Transport of energetic electrons in solids*. Vol. 58. Springer, 2017.

[68] Jean-Noël Chazalviel. *Coulomb Screening by Mobile Charges: Applications to Materials Science, Chemistry, and Biology*. Boston, Basel, Berlin: Birkhäuser, 1999. ISBN: 0-8176-3950-0.

[69] S. J. Pennycook and P. D. Nellist. *Scanning Transmission Electron Microscopy: Imaging and Analysis*. Springer, 2011.

[70] I. S. Gradshteyn and I. M. Ryzhik. *Table of Integrals, Series, and Products*. Ed. by Alan Jeffrey. 5th ed. San Diego: Academic Press, 1994. ISBN: 0-12-294760-6.